

Aalto University
School of Engineering
Department of Applied Mechanics

Aino Saari

Hydrodynamic study on a ducted propeller in a large vessel by time-accurate self-propulsion simulation with Reynolds-Averaged Navier-Stokes -equations

Master's Thesis submitted in partial fulfillment of the requirements for the degree of Master of Science in Technology

Helsinki, September 8, 2014

Supervisor:	Professor Jerzy Matusiak
Advisors:	Juho Ilkko .Sc. (Tech.)
	Miklos Lakatos M.Sc. (Tech.)

Aalto University
School of Engineering

ABSTRACT OF
MASTER'S THESIS

Author:	Aino Saari		
Title:	Hydrodynamic study on a ducted propeller in a large vessel by time-accurate self-propulsion simulation with Reynolds-Averaged Navier-Stokes -equations		
Date:	September 8, 2014	Pages:	74 + 19
Department:	Department of Applied Mechanics		
Professorship:	Marine Engineering	Code:	Kul-24
Supervisor:	Professor Jerzy Matusiak		
Advisors:	Juho Ilkko .Sc. (Tech.) Miklos Lakatos M.Sc. (Tech.)		
<p>In this master's thesis the suitability of a ducted propeller on a large vessel is studied. The study is done from the hydrodynamic point of view and aims at evaluating the effect of a ducted propulsion on the ship power demand when compared to a conventional propulsion system. Based on the results obtained, it is decided whether the further investigations on the topic are advisable.</p> <p>The study is done with a case vessel with the propeller Ka4-55 in duct 19A. The hull form is modified from an existing hull form. There are both model test and RANS-simulation results for the original vessel and they are used as a reference line. The ducted propeller performance behind the vessel is studied by a time-accurate self-propulsion simulation with RANS-solver FINFLO. The duct and propeller are modeled with the Chimera grid method.</p> <p>Approximative results are obtained at the self-propulsion point of the modified vessel. The rotation rate of the ducted propeller is significantly lower than that of the conventional propeller used in comparison and the power demand is higher. FINFLO has tendency to overestimate the propeller torque if the computational grid is not dense enough. When this is taken into account and a correction is made to the obtained torque value, the power demand of the ducted propeller is decreased. Thus it is probable that with a duct and propeller optimized for the vessel in the case, an improvement in the power demand would be achieved. However, the self-propulsion simulation with FINFLO has uncertainties and in order to obtain more reliable results, the self-propulsion tests should be done by other RANS-solvers or in model tests.</p>			
Keywords:	ducted propulsion, power demand, self-propulsion simulation, CFD, RANS, time-accurate simulation, Chimera grid		
Language:	English		

Tekijä:	Aino Saari		
Työn nimi:	Tutkimus suulakepotkurista isossa aluksessa hydrodynamiikan näkökulmasta käyttäen ajan suhteen tarkkaa itsepropulsiosimulointia Reynolds-keskiarvotetuilla Navier-Stokes -yhtälöillä		
Päiväys:	8. syyskuuta 2014	Sivumäärä:	74 + 19
Laitos:	Sovelletun mekaniikan laitos		
Professuuri:	Meritekniikka	Koodi:	Kul-24
Valvoja:	Professori Jerzy Matusiak		
Ohjaajat:	Diplomi-insinööri Juho Ilkko Diplomi-insinööri Miklos Lakatos		
<p>Tässä diplomityössä tarkastellaan suulakepotkurin sopivuutta suuren aluksen propulsiolaitteeksi. Tutkimus tehdään hydrodynamiikan näkökulmasta ja sen tarkoituksena on selvittää suulakepotkurin vaikutus laivan tehontarpeeseen verrattuna tavanomaiseen avopotkuriin. Saatujen tulosten perusteella päätetään, kannattaako jatkossa panostaa suulakepotkurien käyttöön suurissa aluksissa.</p> <p>Tarkastelussa käytettiin potkuria Ka4-55 ja suulaketta 19A ja laivan runkomuoto saatiin muokkaamalla olemassa oleva runkomuoto suulakepotkurille sopivaksi. Alkuperäisellä runkomuodolla tehtyjä RANS simulointeja ja mallikokeita pidettiin vertailukohtana. Suulakepotkurin toimivuutta aluksen perässä testattiin itsepropulsiosimuloinnilla. Simuloinnit tehtiin ajan suhteen tarkkana RANS-ratkaisija FINFLOlla. Suulake ja potkuri mallinnettiin Chimera-hilalla.</p> <p>Itsepropulsiosimuloinnista saatiin suuntaa-antavia tuloksia. Potkurin pyörimisnopeus laski huomattavasti avopotkurin pyörimisnopeudesta ja potkurin tehontarve nousi. FINFLOlla on taipumusta yliarvioida potkurimomentti, kun laskentahilan tiheys ei ole riittävä. Kun tämä otetaan huomioon ja potkurimomenttia korjataan, potkurin tehontarve on pienempi kuin avopotkurin tehontarve. Siten on todennäköistä, että suulake-potkuri yhdistelmällä, joka on optimoitu kyseiselle alukselle, tehontarve tulee laskemaan. On kuitenkin huomattava, että laskentatuloksiin liittyy epävarmuustekijöitä ja siten on tehtävä itsepropulsiosimulointeja muilla RANS-ratkaisijoilla tai itsepropulsiomallikoe ennen kuin voidaan tehdä varmoja johtopäätöksiä.</p>			
Avainsanat:	suulakepotkuri, tehontarve, itsepropulsiosimulointi, CFD, RANS, ajansuhteen tarkka laskenta, Chimera hila		
Kieli:	Englanti		

Acknowledgements

This thesis was written for Deltamarin Ltd. in cooperation with Finflo Ltd. during the first half of the year 2014. I wish to thank Deltamarin for the opportunity for writing this thesis and Finflo for making the topic possible. I really enjoyed doing this thesis and it is almost a pity that now it is finished.

I would like to thank my supervisor Professor Jerzy Matusiak for valuable guidance and support during the process.

I wish to thank my instructors Juho Ilkko and Miklos Lakatos for sharing their knowledge. I also appreciate the advice and comments of Timo Siikonen, Tommi Mikkola, Antonio Sánchez-Caja, Esa Salminen, Matias Niemeläinen and Matti Tammero. It is wonderful that there are so many people whom you can ask for advice when you need it.

Special thanks to my family and friends who supported me during this process and at least pretended to be interested in my topic.

Helsinki, September 8, 2014

Aino Saari

Contents

Contents	v
List of Tables	vii
Abbreviations and Acronyms	x
1 Introduction	1
2 Ducted propulsion	3
2.1 Development of ducted propellers	4
2.2 Physical background	7
2.2.1 Ducted propeller by momentum theory	7
2.2.2 Forces created by the duct	11
2.2.3 Accelerating and decelerating ducts	13
3 State of the art of ship flow simulation	15
3.1 Propeller simulation with conventional and ducted propellers	15
3.1.1 Actuator disk model	15
3.1.2 Lifting line and lifting surface models	16
3.1.3 Boundary element methods	17
3.1.4 RANS simulation	17
3.2 Self-propulsion simulation	19
3.2.1 Hybrid methods	20
3.2.2 Full RANS simulation	20
4 Test case	22
4.1 Hull form	22
4.2 Duct	23
4.3 Propeller	24
4.3.1 Propeller rotation rate and pitch optimization	24
4.3.2 Propeller excitations	25
5 Methods	27
5.1 Governing equations for ship flows	27
5.1.1 Potential flow theory	28
5.1.2 RANS equations	29
5.2 Ship flow simulation tools	33
5.2.1 Potential flow solver ν -SHALLO	33

5.2.2	RANS solver FINFLO	34
5.2.3	Grid generation	36
5.3	Simulation schemes and parameters in FINFLO	40
5.3.1	Resistance simulation scheme	40
5.3.2	Self-propulsion simulation scheme	41
5.3.3	Simulation parameters	42
6	Results and discussion	44
6.1	Resistance simulation	45
6.2	Propeller open water simulation	52
6.2.1	Ducted propeller Ka4-55 in 19A	52
6.2.2	Open propeller	54
6.3	Self-propulsion simulation	56
7	Conclusions	66
7.1	Resistance	66
7.2	Simulation of the propeller in the open water condition	67
7.3	Self-propulsion	67
7.4	Recommendations for further work	68
A	Duct geometry	i
B	Propeller geometry	ii
C	Ka-series polynomials	v
D	FINFLO input and boundary conditions	viii
D.1	Resistance simulation	viii
D.2	Self-propulsion simulation	x

List of Tables

4.1	Ship reference values	23
5.1	Grid dimensions	39
5.2	FINFLOboundary conditions for the ship simulation	40
5.3	Free stream values (model scale)	42
5.4	Simulation parameters used in FINFLOsimulations	43
6.1	Dynamic position of the ship calculated with ν -SHALLOas a percentage of the dynamic position of the vessel A.	45
6.2	Resistance test results as percentage values (model scale)	51
6.3	The propeller open water simulation results on grid level L2 as a percentage of the model test results (Oosterveld, 1970) of the propeller Ka4-55 in duct 19A	53
6.4	The propeller open water simulation results on L1 as a percentage of the model test results (Oosterveld, 1970) of the propeller Ka4-55 in duct 19A	54
6.5	Propeller open water simulation results as a percentage of the model test results of the open propeller of vessel A	55
6.6	Self-propulsion results as a percentage of the self-propulsion model test data of the vessel A(model scale)	64
A.1	Propeller Ka4-55 geometry. Taken from (Kuiper, 1992).	i
B.1	Ordinates of nozzle 19A. Taken from (Kuiper, 1992).	iii
B.2	Ordinates of propeller of Ka-series. Taken from (Kuiper, 1992). . . .	iv
C.1	Coefficients for polynomials, Ka3-65 and Ka4-55. Taken from (Oosterveld, 1970)	vi
C.2	Coefficients for polynomials, Ka4-70 and Ka5-75. Taken from (Oosterveld, 1970)	vii

List of Figures

2.1	Possible location of 1) a fixed duct with rudder, 2) a rotating duct with a movable flap. Taken from (Becker Marine Systems, a)	3
2.2	Supporting types of a rotating duct	4
2.3	Supporting types of a fixed duct.	4
2.4	Nozzle shapes 19 and 19A. Taken from (Carlton, 1994)	5
2.5	Propeller Ka4-70. Taken from (Carlton, 1994)	5
2.6	Simplified model of ducted propeller.	8
2.7	Pressure jump at the propeller plane	8
2.8	Forces on the foil	11
2.9	Force components of a duct. Modified from (Matusiak, 2007a).	11
2.10	Duct forces according to 2D wing theory	12
2.11	Force components of a duct with small angle of attack. Modified from (Matusiak, 2007a).	12
2.12	Accelerating and decelerating duct forms. Modified from (Carlton, 1994).	13
3.1	Lifting and lifting surface presentations for foil sections	16
3.2	Sliding mesh. Taken from (Dhinesh et al., 2010).	18
3.3	Overlapping mesh. Taken from (Zheng and Liou, 2003).	18
4.1	Sketch of the aft ship modifications	23
4.2	Profile of the Wageningen nozzle 19A	23
4.3	Scheme for finding the optimal propeller rotation rate and P/D , when the propeller thrust and diameter are known	24
4.4	Propeller open water curves and $KT(J)$	25
4.5	Modified stern with the chosen ducted propeller Ka4-55	26
5.1	Components of turbulent velocity. Taken from (Mikkola, 2013)	31
5.2	Surface capturing methods. Taken from (Mikkola, 2013)	33
5.3	Hull surface panels before and after several iterations. Taken from (Marzi and Hafermann, 2008).	34
5.4	Cells used for right and left value interpolation with MUSCL approach. Cells used for left and right values are marked with L and R respectively.	35
5.5	Hull surface panelization in Catia	37
5.6	Volume mesh for resistance simulation	38

5.7	Overlapping meshes of propeller and duct used in self-propulsion simulation. The duct surface and mesh outer edge are red and the propeller surface and mesh outer edge are blue	39
5.8	Meshes of propeller and duct used in self-propulsion simulation	39
5.9	Self-propulsion scheme	41
6.1	Convergence of the total resistance coefficient of the vessel B	46
6.2	Convergence of the turbulent kinetic energy of the vessel B	47
6.3	Convergence of the minimum and maximum wave heights of the vessel B	48
6.4	Wave patterns of modified (above) and original (below) hull forms . .	49
6.5	Wave pattern at the aft region of modified (above) and original (below) hull forms	49
6.6	Nominal wake at the propeller plane of the original vessel (left) and modified vessel (right)	50
6.7	Nominal wake at the propeller disk of original (left) and modified (right) hull forms	50
6.8	Propeller open water curves and simulation results for Ka4-55 in duct 19A with $P/D = 1.2$. The simulation results on grid level L2 are marked with dots and the results on grid level L1 with crosses. The design point of the propeller is marked with the dashed line.	53
6.9	Propeller open water curves and simulation results for the open propeller used in the vessel A. The simulation results (grid level L2) are marked with dots and the design point is marked with a dashed line.	55
6.10	Convergence of the total resistance coefficient in quasi-static (QS) and time-accurate (TA) simulations on the coarse and medium grids (L3 and L2)	56
6.11	Convergence of the turbulent kinetic energy	57
6.12	Convergence of the minimum and maximum wave heights	57
6.13	Convergence of the total thrust of the propeller and the duct	58
6.14	Convergence of the propeller thrust	58
6.15	Convergence of the duct thrust	59
6.16	Convergence of the propeller moment	59
6.17	Wave pattern of the self-propulsion simulation obtained on grid level L3	60
6.18	Wake field at $D/3$ after the propeller plane	61
6.19	Thrust forces of the propeller blades during one propeller revolution .	62
6.20	Moments around the propeller axis of the propeller blades during one propeller revolution	62
B.1	Geometry of propeller Ka4-55	iii

Abbreviations and Acronyms

Nomenclature

Upper case

A	cross-sectional area
A_0	propeller disk area
A_e	effective propeller disk area
A_e/A_0	propeller area ratio
$A_{x,y}, B_{x,y}, C_{x,y}$	polynomial coefficients
C	constant value
C_A	correlation allowance coefficient
C_F	friction resistance coefficient
C_f	skin friction coefficient
CFL	Courant number
C_T	thrust loading coefficient, total resistance coefficient
$C_{T,p}$	propeller thrust loading coefficient
D	propeller diameter, drag force
E	total internal energy
EAR	propeller area ratio
F	inviscid flux vector in x -direction
\hat{F}	flux through a face
F_D	towing force in self-propulsion simulation
F_i	body force
F_k	kinetic energy flux
Fn	Froude number
F_{tot}	total force
$F_{tot}, G_{tot}, H_{tot}$	total flux in x, y, z direction respectively
F_v	viscous flux term in x -direction
I, J, K	coordinate directions
J	propeller advance coefficient
K_T	thrust loading coefficient
K_{TN}	nozzle thrust loading coefficient
K_Q	torque loading coefficient
K_{QT}	torque loading coefficient by thrust identity
L	nozzle length, lift force, characteristic length

L_{PP}	length between perpendiculars
L_{OS}	overall submerged length of a ship
P/D	propeller pitch-diameter ratio
P_E	effective power
P_D	power delivered at propeller
P_T	thrust power
Q	source term, propeller torque
R	propeller radius
R_i	relation of the change of the conservative quantities in the sequential nodes
R_{ij}	Reynolds stress
Rn	Reynolds number
R_R	residual resistance
R_T	total resistance
R_V	viscous resistance
S	ship wetted surface, boundary of control volume
S_{ij}	rate of strain tensor
T	thrust
T_p	propeller thrust
T_{tot}	total thrust
T_∞	free stream temperature
U	vector of conservative terms
U_0	inflow velocity, free stream velocity
U_A	propeller induced velocity at propeller plane
$U_{A,0}$	propeller induced velocity far down stream
U^l, U^r	left and right values of conservative quantities
V	control volume, velocity
V_s	ship velocity
\vec{V}	velocity vector
V_A	advance velocity
V_∞	free stream velocity
Z	number of propeller blades

Lower case

c	chord length, void fraction
d	cell height
f	frequency
g	acceleration due to gravitation
h	free surface height
k	turbulent kinetic energy
m	potential flow source strength, model scale
\dot{m}	mass flow
n	propeller rotation rate
n_x, n_y, n_z	surface unit normals in x, y, z direction
p	pressure
Δp	change in pressure

\bar{p}	average pressure
p'	fluctuating pressure
p_a	atmospheric pressure
p_∞	pressure far field
p^-	pressure before propeller plane
p^+	pressure after propeller plane
r	distance between two points, radius
t	thrust deduction factor
u	velocity
\bar{u}	average velocity
u'	fluctuating velocity
u_τ	friction velocity
w	velocity in z direction, wake fraction
w_n	nominal wake fraction
w_T	effective wake fraction (Taylor wake fraction)
x, y, z	coordinates
y^+	non-dimensional distance

Greek letters

α	angle of attack
α_p	under relaxation coefficient of pressure correction
α_u	under relaxation coefficient of velocity correction
δ_{ij}	Kronecker delta
ϵ	dissipation of turbulent kinetic energy
η_0	open water efficiency
η_D	propulsive efficiency
η_I	ideal efficiency of a propeller
η_R	relative rotative efficiency of a propeller
κ	parameter defining discretization scheme
μ	molecular viscosity
μ_T	eddy viscosity
ν	kinematic viscosity
ρ	density
σ_{ji}	viscous stress
τ	duct loading factor
τ_{wall}	wall shear stress
ϕ	velocity potential, scalar function
ω	specific rate of dissipation of turbulent kinetic energy
∇	displacement, nabla operator

Subscripts

∞	free stream
i	cell index
i, j	component
m	model scale

p	propeller
s	ship scale
tot	total
x, y, z	coordinate direction

Abbreviations

BEM	Boundary Element Method
CFD	Computational Fluid Dynamics
CPU	Central Processing Unit
CRS	Cooperative Research Ships
DES	Detached Eddy Simulation
DNS	Direct Navies-Stokes
FMG	Full Multi-Grid
FVM	Finite Volume Method
HSVA	Hamburgische Schiffbau Versuchsanstalt
ITTC	International Towing Tank Conference
LE	Leading Edge
LES	Large Eddy Simulation
MUSCL	Monotonic Upstream-Centered Scheme for Conservation Law
MRF	Multi Reference Frame
NS	Navier-Stokes
NSMB	Netherlands Ship Model Basin
POW	Propeller Open Water curves
RANS	Reynolds-averaged Navies-Stokes
RPM	Revolutions Per Minute
RPS	Revolutions Per Second
RSM	Reynolds Stress Model
SST	Shear Stress Transport
TA	Time Accurate
TE	Trailing Edge
VOF	Volume of Fluid
QS	Quasi Static

Chapter 1

Introduction

The energy efficiency of ships is becoming increasingly important and the ship propulsion systems are one field where improvements for the energy efficiency are searched. The propulsion with a better efficiency means less required power from a main engine and hence it is more profitable for a ship owner. A more important advantage is, that the propulsion system with the better efficiency is more environmentally friendly since the exhaust emissions are smaller.

At present the efficiency of the ships is mainly attempted to improve by optimizing the hull and propeller forms separately with the CFD (Computational Fluid Dynamics) tools and/or model tests. The hull flow simulation by RANS (Reynolds-averaged Navier-Stokes) and propeller simulation by the potential flow theory can give quite well optimized shapes, but since the hull-propeller interaction is not usually studied in these processes, surprises in the propulsion efficiency might occur when the self-propulsion model test is done. Thus it would be a great advantage to be able to include the self-propulsion testing for the optimization process done with the CFD. The self-propulsion simulation tools are currently being developed and they are already able to give results with moderate accuracy but they are not yet used in the daily design. However, even at its current state, the self-propulsion simulation can give more freedom for developing new propeller-hull combinations as it is not necessary to conduct expensive model tests to get an idea of the functionality of the combination. At the first stages of a development of a new concept it can be enough to get approximate results in order to decide whether the concept is worth of a deeper study.

By tradition, in large merchant vessels conventional open propellers either with a fixed or a controllable pitch are used and the maximum efficiency of the propeller is reached by using the largest possible diameter and optimizing the propeller shape when the nominal wake field of the ship is known. The efficiency of the open propeller behind the hull can be in some situations further improved by different flow stabilizing devices, such as pre-swirl stators and ducts positioned upstream of the propeller. These devices are intended for creating a more uniform inflow to the propeller and in this way improving the propeller efficiency. In addition to conventional open propeller solutions, alternative propulsion systems are searched for decreasing the required power even more. For example ducted propeller arrangements, which are by tradition used in small vessels requiring a lot of thrust while moving slowly, have raised interest. The traditional vessels for the ducted propulsion are for example trawlers, tugboats and dredgers but it is, however, possible that implementing a

ducted propeller in a large vessel having a relatively highly loaded propeller, would result in a decrease in power demand. In this thesis a such implementation is done in order to find out whether it is a profitable solution from the hydrodynamic point of view. The profitability of the implementation is studied by the resistance and self-propulsion simulations with RANS by FINFLO-solver and obtained results are compared to the model test and RANS simulation results of the same vessel with the open propeller.

In this thesis, the introduction is given in Chapter 1. In Chapter 2 the ducted propellers are introduced, the history and the state of the art of the ducted propellers are discussed and the description of the physical background is given. In Chapter 3 the state of the art of the propeller and self-propulsion simulation is reviewed and in Chapter 4 the test case vessel and selection of the ducted propeller is presented. A description of the ship flow simulation both with the potential flow and RANS equations is introduced in Chapter 5 as well as the simulation programs *v-SHALLO* and *FINFLO*. In Chapter 6 the simulation results of the resistance, propeller open water and self-propulsion tests are presented and discussed. Finally in Chapter 7 conclusions are made and recommendations for further work are given.

Chapter 2

Ducted propulsion

A ducted propulsion unit consist of a propeller with a fixed or controllable pitch and duct which can be fixed or rotate around a vertical axis. With the fixed duct the propeller is located at the approximately same location as the open propeller while the rotating propeller without the rudder can be placed more astern. Examples of duct locations for fixed and rotating ducts are shown in Figure 2.1. In addition to the propeller location, the duct type affects also the duct support type, since the steerable duct must be free to rotate while there are no such requirements for fixed duct supports.

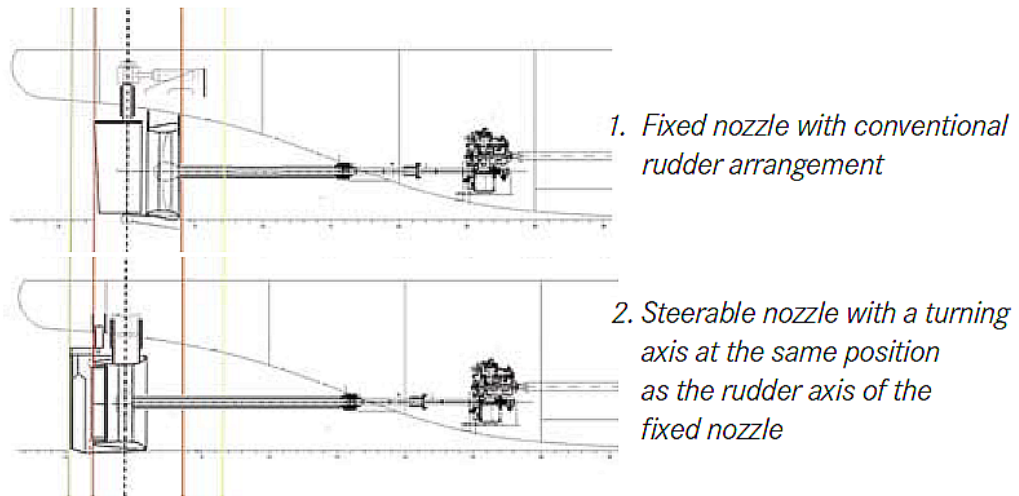


Figure 2.1: Possible location of 1) a fixed duct with rudder, 2) a rotating duct with a movable flap. Taken from (Becker Marine Systems, a)

A rotating duct is supported with one or two support points which are located above and below the duct at its rotation axis. If the supporting is done with one point, the point above the duct is used and the support type is called hanged, while for the two point support an additional heel support is build below the duct and the support type is called heel supported. These support types are shown in Figure 2.2. (Becker Marine Systems, b) For fixed ducts the support types are called the strut support and head-box support. When the strut supports are used, two or three aerofoil-shaped struts support the duct whereas in the head-box support the duct is fixed to the hull with a box shaped support. (Minchev et al., 2009) Examples of

the fixed duct supports are shown in Figure 2.3.

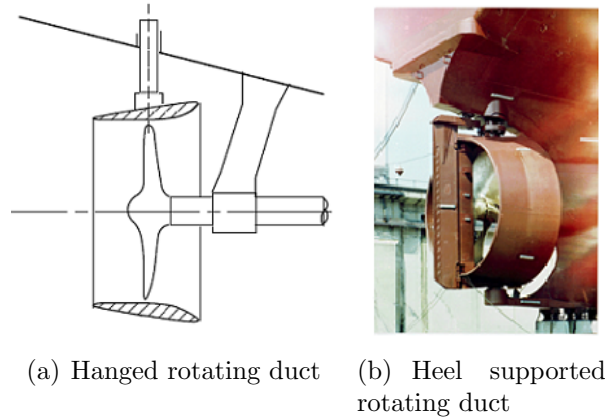


Figure 2.2: Supporting types of a rotating duct

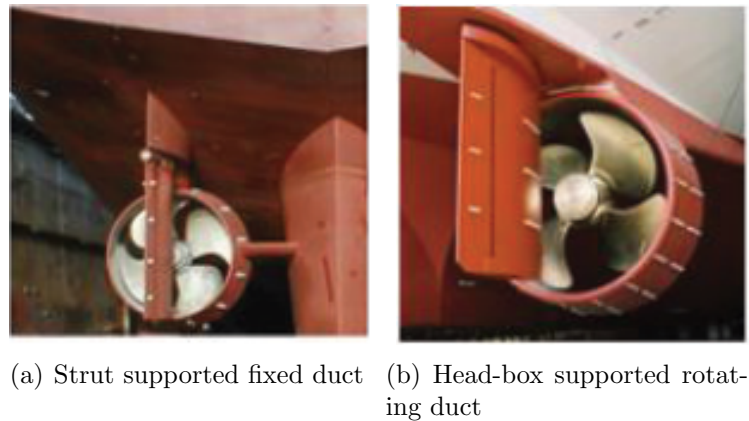


Figure 2.3: Supporting types of a fixed duct.

The above-mentioned matters affect the suitability of the ducted propulsion in different cases. For example, a steerable duct is not necessarily fitting for a vessel needing a good maneuvering performance but can be a good choice for a vessel having a lot of straight course sailing, whereas a fixed duct with a rudder gives better maneuvering capability but also requires more room in the aft. Next the development of ducted propellers starting from 1930s is reviewed and the current state of the art of the ducted propulsion is described.

2.1 Development of ducted propellers

The first articles considering the ducted propulsion were published by Stipa in 1931 and Kort in 1934. In these articles model tests of ducted propellers were reported and since the results with accelerating nozzles were considered to be encouraging, the research on the ducted propulsion was continued. (Sacks and Burnell, 1959) One

of the following studies was the extensive model test experiments by van Manen in 1950s at NSMB (Netherlands Ship Model Basin). In these model tests the duct and propeller shapes were optimized and the resulting shapes were published together with the propeller open water curves. The most popular duct shapes developed were the nozzles 19A and 37, where the nozzle 37 is designed to have a good bollard pull performance also in the astern direction. The nozzle shapes are shown in Figure 2.4. Additionally a propeller series was developed for the accelerating ducts, since the conventional propellers had a bad cavitation behavior. The new Ka-propeller series had wide blade tips (so called Kaplan-type), which reduced the danger of cavitation. In Figure 2.5 is shown an example of the propeller blade design in Ka-series. (Oosterveld, 1970)

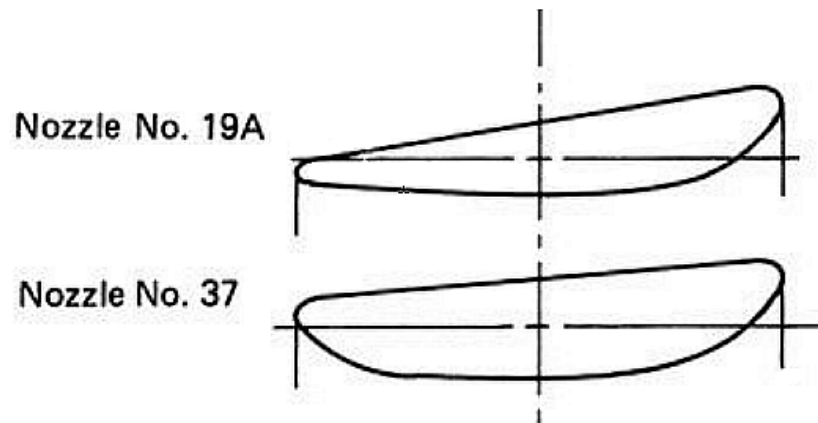


Figure 2.4: Nozzle shapes 19 and 19A. Taken from (Carlton, 1994)

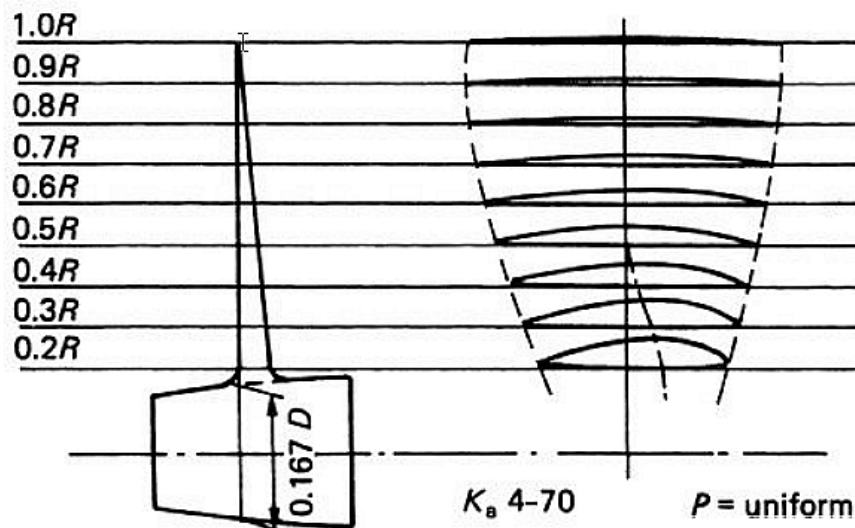


Figure 2.5: Propeller Ka4-70. Taken from (Carlton, 1994)

The work done on the ducted propulsion development at NSMB has created the basis for the further development of the ducted propulsion. The NSMB duct series (known also as Wageningen duct series) together with the Ka-propeller series are still used as a comparison and starting point for new designs because the model tests results and geometry information of the series are freely available and can be found for example in (Oosterveld, 1970).

The traditional use of the ducted propulsion is in small vessels which operate close to the bollard pull condition, i.e. close to the condition where the ship does not advance but still needs a lot of thrust from the propeller. A great deal of the research is considering this kind of traditional combinations but also different applications have been considered. Based on the model tests done at NSMB it was suggested that the ducted propulsion would be feasible, if the thrust loading coefficient of the vessel was high enough, i.e. $C_T > 2 - 3$, which means that the ducted propulsion is an alternative for example for towing vessels, trawlers, tankers, coasters and some of the single screw cargo ships (Oosterveld, 1970). The assumption was studied with model tests of tankers having a ducted propulsion by Oosterveld (1970) and a 2 – 6 % decrease in the power demand was obtained when compared to the conventional propellers. However, even though power savings were obtained with the ducts of NSMB series and they are still offered by manufacturers, it is known that they are not optimal designs for all cases as it is possible to create duct shapes having smaller duct resistance and greater duct thrust, especially for higher speeds (Dang and Laheji, 2004).

Researches on the duct shape and propeller optimization have been done for example by Pylkkänen (1991), Taketani et al. (2009), Tamura et al. (2010) and Minchev et al. (2009). Pylkkänen (1991) studied the effect of the propeller advance number on the ducted propeller efficiency with different duct shapes which were modified from the nozzle 19A. Taketani et al. (2009) and Tamura et al. (2010) developed a new duct and propeller for ‘Z-peller’ propulsion system of Niigata Power Systems Co., Ltd by using the nozzle 19A as an initial nozzle shape for the new design, while Minchev et al. (2009) compared the nozzle 19A with the MAN Diesel AHT nozzle. Both ‘Z-peller’ and AHT nozzle produced more thrust in the bollard pull condition when compared to the nozzle 19A, which reveals that with the modern design and CFD tools the ducted propellers can be further optimized. Better results in the optimization can be achieved by instead of optimizing only the ducted propeller, including also the hull modifications and the duct support optimization in the process (Minchev et al., 2009). An example of a such optimization process can be found in (Minchev et al., 2009). By tradition the ducted propellers are optimized for the bollard pull condition but it is also possible to optimize the ducts for the free sailing condition and for example HR-nozzle (Wärtsilä) and Rice Speed nozzle (Rice Speed) are designed for higher velocities. In (Çelik et al., 2011) the performance of these nozzles in a high speed passenger ferry has been studied and compared to the performance of the nozzle 19A. It was found out that the newer nozzle designs HR-nozzle and Rice Speed nozzle were more suitable for the high speed ship than the nozzle 19A having about 10 % smaller power demand.

Regardless of the evidence of the ducted propulsion feasibility in tankers and new duct shapes designed for free sailing, the ducts are still most commonly used in small vessels, even though also large ducts with diameters up to eight meters have been

manufactured. With larger ducts, however, the manufacture becomes complicated since it is difficult to reach the required tolerances in the duct circularity. The manufacture has also been limiting the complexity of the duct shapes, which in practice have been axisymmetric although also non-axisymmetric duct shapes with varying duct foil shapes and radii have been designed in order to smooth the wake field at the propeller plane. (Carlton, 1994) For example Oosterveld (1970) tested non-axisymmetric ducts behind a tanker and found out that non-axisymmetry of the nozzle decreased the required power by 3 % more than the axisymmetric duct. With this kind of non-conventional duct shape designs a better propeller efficiency would be achieved, but the high cost and manufacture difficulties have prevented their use in practice (Carlton, 1994). Other ideas for improving the ducted propulsion efficiency are for instance the duct with suction and/or injection at the trailing edge, ring propeller which has the propeller blades fixed to the duct (Oosterveld, 1970) and the duct with the movable flaps (Becker Marine Systems, b). The ducts have also been used before the propeller for stabilizing the flow field (Becker Marine Systems, b).

Above the topic of the ducted propulsion has been discussed in a general level. Next a deeper review of the physical background and characteristics of a ducted propeller is given.

2.2 Physical background

When being a part of a propulsion system, the duct changes the inflow velocity to the propeller and creates negative or positive thrust force. These phenomena have effect on the propeller behavior and efficiency of the propulsion system. (Matusiak, 2007a) Next the physical background of the ducted propellers is considered and the classification to the accelerating and decelerating ducts is introduced.

2.2.1 Ducted propeller by momentum theory

The basic idea of the ducted propulsion can be explained with the momentum theory. The simplified model used is shown in Figure 2.6, where the propeller plane is located at $x = 0$, A_0 is the propeller disk area, V_A is the inflow velocity, U_A is the induced velocity at the propeller plane, $U_{A,0}$ is the induced velocity far downstream, p^∞ is the pressure far field and p^- and p^+ are the pressures up- and downstream of the propeller plane respectively. When the pressures and velocities defined in Figure 2.6 are used, the thrust forces can be derived separately for the duct-propeller combination and propeller alone.

The total thrust developed by the propulsion system can be presented as a change in the momentum of the fluid. Thus the total thrust T_{tot} of the ducted propeller is

$$T_{tot} = \dot{m}(V_A + U_{A,0}) - \dot{m}V_A = \dot{m}U_{A,0}, \quad (2.1)$$

where the mass flow \dot{m} through the propeller plane can be written as

$$\dot{m} = \rho A_0 (V_A + U_A) \quad (2.2)$$

and the total thrust developed is obtained to be

$$T_{tot} = \rho A_0 (V_A + U_A) U_{A,0}. \quad (2.3)$$

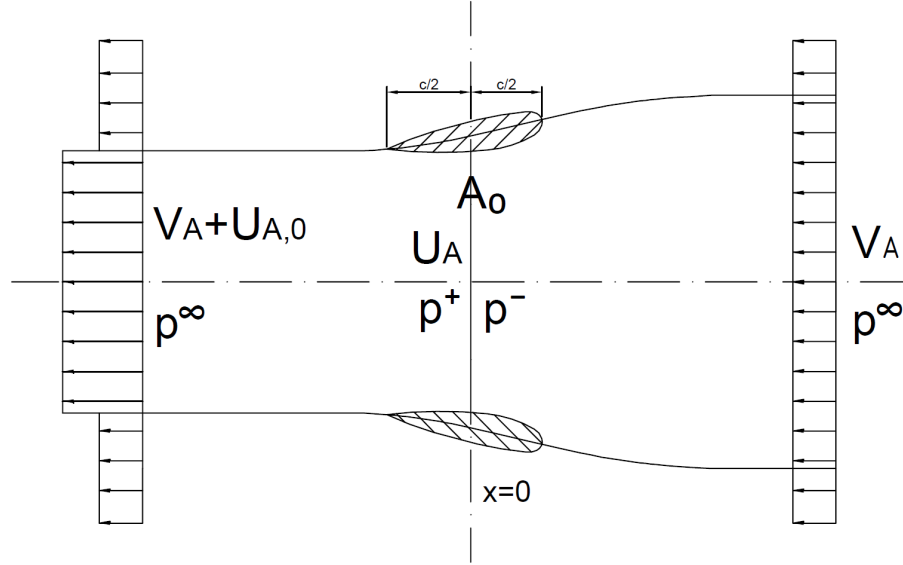


Figure 2.6: Simplified model of ducted propeller.

As the momentums in Equation (2.1) are defined far up- and downstream from the propeller plane, the thrust obtained includes both propeller and duct thrusts. (Kerwin, 2010; van Manen and Oosterveld, 1972)

The propeller thrust alone can be obtained with the pressure jump created by the propeller at the propeller plane, shown in Figure 2.7. The propeller thrust T_p

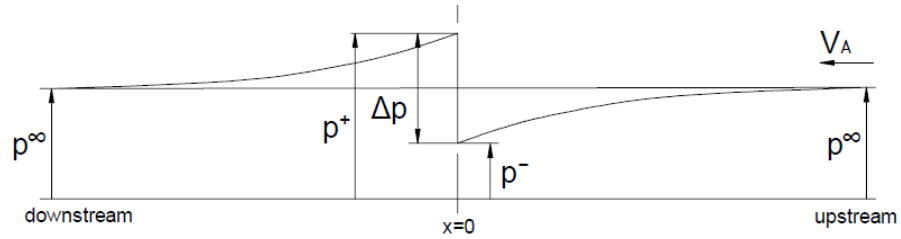


Figure 2.7: Pressure jump at the propeller plane

expressed with the pressure jump Δp is

$$T_p = \Delta p A_0, \quad (2.4)$$

where the pressure jump can be calculated from the Bernoulli equation

$$p + \frac{1}{2}\rho V^2 + \rho g z = C, \quad (2.5)$$

where C is constant. The pressure before the propeller plane p^- is obtained by writing the Bernoulli equation far upstream and right before the propeller plane and setting them equal

$$p_\infty + \frac{1}{2}\rho V_A^2 = p^- + \frac{1}{2}\rho(V_A + U_A)^2 \quad (2.6)$$

$$p^- = p_\infty + \frac{1}{2}\rho V_A^2 - \frac{1}{2}\rho(V_A + U_A)^2. \quad (2.7)$$

Respectively the pressure right after the propeller plane p^+ is obtained by the Bernoulli equations just after the propeller plane and far downstream

$$p^+ + \frac{1}{2}\rho(V_A + U_A)^2 = p_\infty + \frac{1}{2}\rho(V_A + U_{A,0})^2 \quad (2.8)$$

$$p^+ = p_\infty + \frac{1}{2}\rho(V_A + U_{A,0})^2 - \frac{1}{2}\rho(V_A + U_A)^2. \quad (2.9)$$

Hence the pressure jump at the propeller plane can be calculated to be

$$\Delta p = p^+ - p^- = \frac{1}{2}\rho(2V_A + U_{A,0})U_{A,0} \quad (2.10)$$

and the thrust developed by the propeller is obtained by substituting the pressure jump from Equation (2.10) to Equation (2.4)

$$T_p = \frac{1}{2}\rho A_0(2V_A + U_{A,0})U_{A,0}. \quad (2.11)$$

As the pressures jump is defined inside the duct and pressure values are defined very close to each other, the effect of the duct is not included in the thrust definition. (Matusiak, 2007a; Kerwin, 2010; van Manen and Oosterveld, 1972)

A general coefficient used for presenting the propeller loading rate is the non-dimensional thrust loading coefficient C_T which is defined as

$$C_T = \frac{T}{\frac{1}{2}\rho A_0 V_A^2}. \quad (2.12)$$

For the ducted propeller the thrust loading coefficient is usually calculated with the total thrust of the system, which gives

$$C_T = \frac{T_{tot}}{\frac{1}{2}\rho A_0 V_A^2}. \quad (2.13)$$

The propeller loading coefficient is obtained from the total thrust loading coefficient with the duct loading factor τ so that

$$C_{T,p} = \tau C_T \quad (2.14)$$

where τ is defined as

$$\tau = \frac{T_p}{T_{tot}}. \quad (2.15)$$

The smaller τ is, the larger part of the total thrust is created by the duct. If $\tau = 1$, no thrust is created by the duct and when $\tau > 1$, the duct creates negative thrust and the propeller loading increases since the propeller has to create the thrust also for canceling the negative thrust created by the duct. Thus, the situation where $\tau > 1$, is not desirable and the smaller τ is, the less power is demanded from the propeller and the more effective the propulsion system is. A measure used for estimating the efficiency of a propulsion system is the ideal efficiency η_I which is obtained with

$$\eta_I = \frac{P_T}{P_D}, \quad (2.16)$$

where P_T is a thrust power and P_D is a power delivered at the propeller. The thrust power can be simply calculated from

$$P_T = T_{tot}V_A = \rho A_0(V_A + U_A)U_{A,0}V_A \quad (2.17)$$

and the power delivered at the propeller P_D can be calculated as a kinetic energy flux through the propeller plane, which is

$$F_k = \frac{1}{2}\dot{m}_2V_2^2 - \frac{1}{2}\dot{m}_1V_1^2, \quad (2.18)$$

where subscripts 1 and 2 correspond to chosen cross sections in the flow field. To obtain the power delivered at the propeller P_D , these cross sections are set just before and after the propeller plane and thus the power delivered at the propeller is obtained to be

$$P_D = \frac{1}{2}\dot{m}(V_A + U_{A,0})^2 - \frac{1}{2}\dot{m}V_A^2 \quad (2.19)$$

$$= \frac{1}{2}\rho A_0(V_A + U_A)[(V_A + U_{A,0})^2 - V_A^2]. \quad (2.20)$$

When Equations (2.17) and (2.20) are substituted to Equation (2.16), the ideal efficiency η_I is after simplifying obtained to form

$$\eta_I = \frac{1}{1 + \frac{1}{2}\frac{U_{A,0}}{V_A}}. \quad (2.21)$$

Since it is more practical to express the ideal efficiency with a parameter linked with the thrust instead of the rate of induced and incoming velocities $U_{A,0}/V_A$, the velocity rate is expressed in terms of the thrust loading coefficient. The relation between the velocity rate and the thrust loading coefficient is obtained by first calculating the thrust loading coefficient in Equation (2.12) with the propeller thrust from Equation (2.11)

$$C_{T,p} = 2\left(1 + \frac{1}{2}\frac{U_{A,0}}{V_A}\right)\frac{U_{A,0}}{V_A} \quad (2.22)$$

and next solving the rate of velocities $\frac{U_{A,0}}{V_A}$ from Equation (2.22). The rate of velocities is obtained to be

$$\frac{U_{A,0}}{V_A} = -1 + \sqrt{1 + C_{T,p}} \quad (2.23)$$

and when this is substituted to Equation (2.21), the ideal efficiency is obtained to be

$$\eta_I = \frac{2}{1 + \sqrt{1 + C_{T,p}}}. \quad (2.24)$$

The ideal efficiency can be further modified to a form where the duct effect can be easily seen when the relationship from Equation (2.14) is substituted to ideal efficiency expression in Equation (2.24)

$$\eta_I = \frac{2}{1 + \sqrt{1 + \tau C_T}}. \quad (2.25)$$

From Equation (2.25) it can be seen that the duct creating thrust ($\tau < 1$) increases the ideal efficiency and respectively a duct creating negative thrust ($\tau > 1$) decreases the ideal efficiency. (Matusiak, 2007a; Kerwin, 2010; van Manen and Oosterveld, 1972)

From the efficiency point of view, a ducted propeller is the better the larger part of the thrust is created by the duct. However, the actuator disk theory does not explain, how a duct creates thrust and thus it is discussed in the next section.

2.2.2 Forces created by the duct

A duct section is a lifting foil section, which creates forces when the flow passes it. The forces result from the pressure differences on the foil surface and they can be divided to lift and drag forces, from which the lift L is perpendicular and drag D is parallel to the inflow. The total force F_{tot} resulting from the pressure differences and the force division to the lift and drag forces are shown in Figure 2.8. (Molland and Turnock, 2007) In the duct the interesting component instead of the lift or drag is the thrust component in horizontal direction, which is shown in Figure 2.9. In

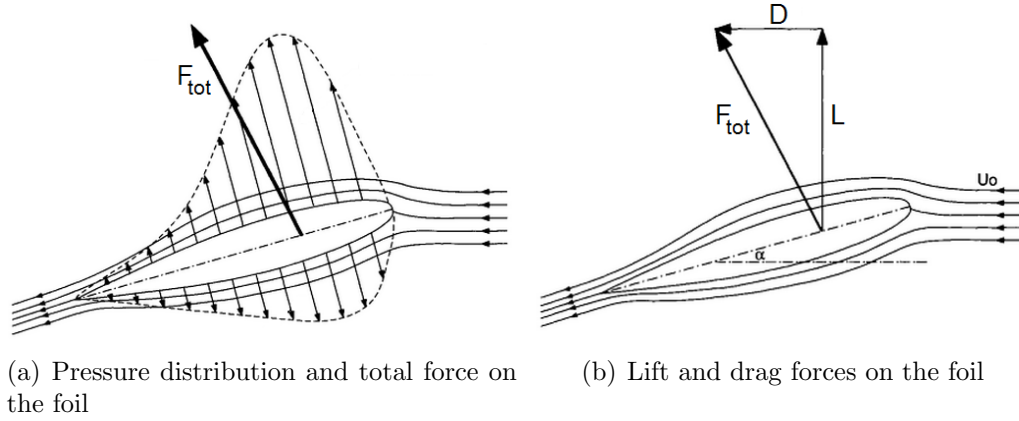


Figure 2.8: Forces on the foil

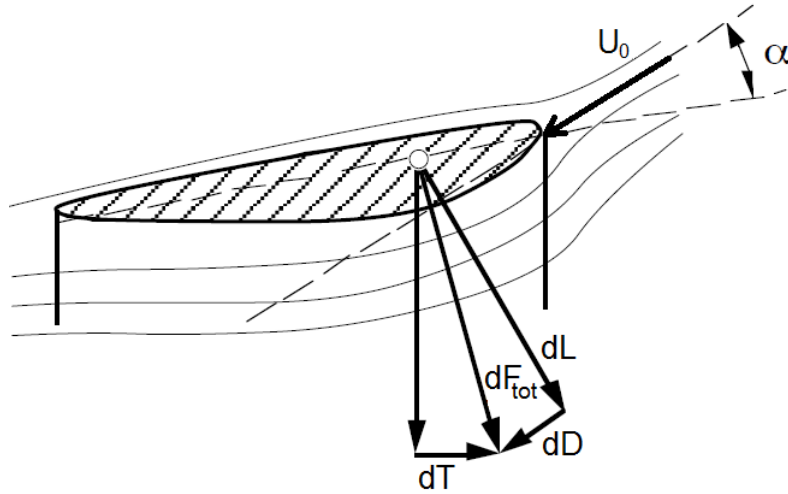


Figure 2.9: Force components of a duct. Modified from (Matusiak, 2007a).

Figure dT is the thrust component, dF_{tot} the total induced force, dL the lift force, dD the drag force, U_0 the inflow velocity and α the angle of attack. (Matusiak, 2007a)

When considering the duct forces, it must be taken into account that the duct is an axisymmetric object and each force component of a duct section has a responding reversed component. Thus, according to the 2D wing theory, the duct alone in the uniform inflow creates no total force, since the force created by the duct section is perpendicular to inflow and canceled by reversed component, as shown

in Figure 2.10(a). Adding a rotating propeller inside the duct modifies the inflow angle and a thrust force is created, as shown in Figure 2.10(b). When the viscous forces and the induced drag by free vortices are taken into account, the propeller is still a requirement for the duct to create positive thrust, since the viscous effects and vortices create drag. However, if the inflow angle to the duct is too small or negative, the duct creates negative thrust force, as shown in Figure 2.11. (Matusiak, 2007a)

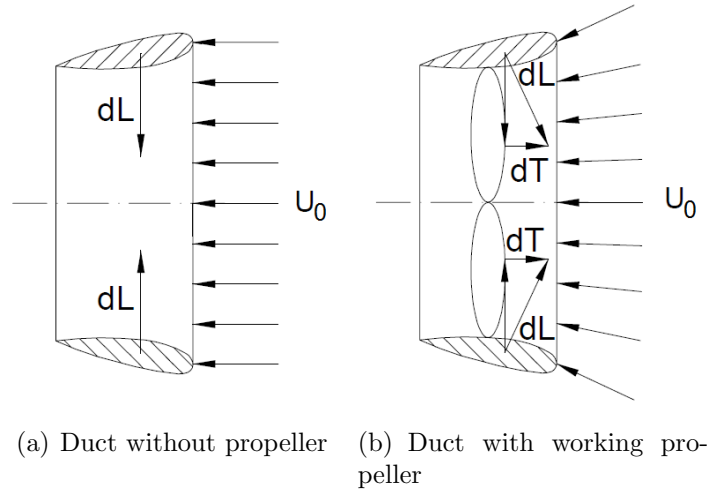


Figure 2.10: Duct forces according to 2D wing theory

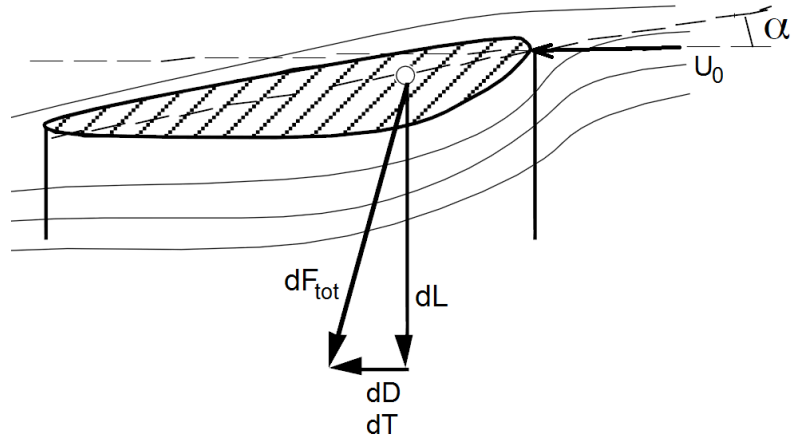


Figure 2.11: Force components of a duct with small angle of attack. Modified from (Matusiak, 2007a).

It was mentioned previously, that the duct creates negative thrust only if the inflow angle to the duct is too small but in reality, also the duct section shape affects the thrust generation. There are duct shapes which are not able to generate positive thrust while others can produce a remarkable amount of it. By using the conventional classification of the duct profiles to accelerating and decelerating ducts,

it can be said that decelerating ducts do not create thrust while accelerating ducts do. Next the classification to accelerating and decelerating ducts is declared.

2.2.3 Accelerating and decelerating ducts

The duct shape classification is done based on the duct effect on the flow velocity. As the names accelerating and decelerating ducts suggest, the accelerating ducts accelerate and decelerating ducts decelerate the flow from the duct inlet to the propeller plane. The duct effect on a flow velocity can be seen from the continuity equation, which for a flow in a steady state is a requirement for a constant mass flow

$$\dot{m}_1 = \dot{m}_2 \quad (2.26)$$

$$\rho V_1 A_1 = \rho V_2 A_2, \quad (2.27)$$

where A_1 , V_1 , A_2 and V_2 are the cross sectional areas and flow velocities at locations 1 and 2 respectively. If it is assumed that location 1 is at the inlet of the duct, location 2 is at the propeller plane and the density is constant, the velocity at the propeller plane is obtained to be

$$V_2 = \frac{A_1}{A_2} V_1. \quad (2.28)$$

From Equation (2.28) it can be seen, that the flow is accelerated to the propeller plane, if the cross-sectional area of the duct is decreased from the inlet to the propeller plane. Thus an accelerating duct is such that it has a smaller cross sectional area at the propeller plane than at the inlet and respectively a decelerating duct has a larger diameter at the propeller plane than at the inlet. In Figure 2.12 are shown examples of accelerating and decelerating duct profiles.

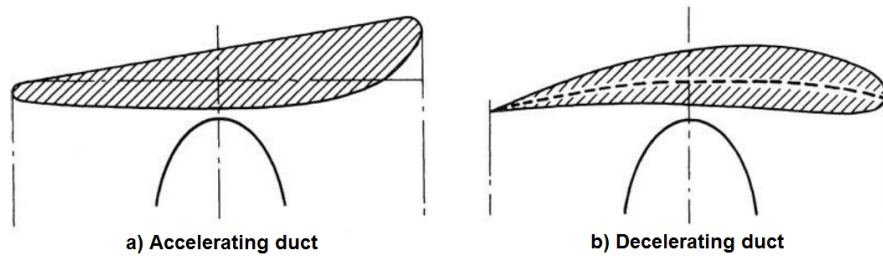


Figure 2.12: Accelerating and decelerating duct forms. Modified from (Carlton, 1994).

The accelerating ducts can increase the propeller efficiency, while the decelerating ducts always decrease it. This can be seen by comparing the ideal efficiencies of ducted propellers to the ideal efficiency of an open propeller. In the consideration it is assumed that the propeller is in an uniform inflow V_A and the propeller thrust T_p is the same for all propellers. For an open propeller the inflow velocity is also the propeller advance velocity and if the propeller is put inside an accelerating duct, the propeller advance velocity is increased from V_A . This decreases the propeller loading coefficient in Equation (2.12) and increases the ideal efficiency in Equation (2.24). If

the propeller is instead put inside a decelerating duct, the propeller advance velocity is decreased from V_A , the propeller loading coefficient is increased and the propeller ideal efficiency is decreased.

Traditionally the accelerating ducts are used because they are able to create theoretically up to 50 % more thrust in the bollard pull condition than the conventional open propellers (Carlton, 1994). The accelerating ducts can also have a better ideal efficiency but on the other hand the increased inflow velocity can cause cavitation problems on the propeller blades and the advantage of the duct can be canceled by the viscous resistance of the duct. As the decelerating ducts have a negative effect on the efficiency, they are in practice used only in the naval ships for reducing the cavitation risk and noise level of the vessel. Because the accelerating ducts can have a positive effect on the propulsion power demand, they are a potential propulsion system when new, more efficient solutions for the ship propulsion are searched. Development projects both for the duct and propeller geometries and ducted propeller simulation tools exist. For example at CRS (Cooperative Research Ships) a simulation tool for ducted propulsion is being developed, as it is expected that ducted propellers will in future raise interest also among other kind of ship types than those which traditionally use the ducted propulsion.

In this chapter the development of the ducted propellers was discussed, the physical background was considered with the momentum theory and the thrust creation mechanism of the duct was presented. Also the classification to accelerating and decelerating ducts was clarified and the possibilities of the accelerating ducts were reviewed. In the next chapter the state of the art of the simulation methods for conventional propellers and their extensions for the ducted propulsion is presented and the state of the art and basics of the self-propulsion simulation methods are discussed.

Chapter 3

State of the art of ship flow simulation

The flow simulation is an useful tool in the hydrodynamic design of the ships since it can produce detailed information about the flow around the hull and propeller already before model tests. Different simulation tools have been and are being developed for ship resistance, propeller and self-propulsion testing. The resistance simulation tools using RANS-equations give already results with good accuracy and they are being used as daily design tools and as well the potential flow methods are commonly used in the propeller design and analysis. The self-propulsion simulation is such a new field that the methods are not yet commonly used in design purposes but are being further developed. In this chapter short reviews of the propeller simulation and self-propulsion simulation methods are given.

3.1 Propeller simulation with conventional and ducted propellers

The CFD tools for the propeller design are on a good level. The CFD simulation is used for the design and analysis of the propellers and tools used are mostly potential flow based methods, such as lifting line and lifting surface methods and panel methods. The most simplified propeller model is the actuator disk model whereas the RANS solvers have the most detailed description of the propeller and flow. The propeller simulation methods have first been developed for open propellers but they can be applied also for the ducted propellers. The nozzle around the propeller creates though additional challenges to the simulation, the main challenge being the simulation of the tip vortex flow in a gap between the propeller blade tip and the duct (Yu et al., 2013). In next sections the different propeller simulation methods are shortly described.

3.1.1 Actuator disk model

The easiest way for the propeller flow modeling is the actuator disk model, which theoretical background was explained in Section 2.2.1 by the momentum theory. The general actuator disk model for open propellers is based on the assumption

that the propeller is a thin, permeable disk in the flow, which introduces a pressure jump to the flow. The flow at the propeller disk is accelerated and either only axial or both axial and tangential velocities are taken into account. This basic model can be extended for the ducted propellers, in which case the propeller thrust is given by the similar actuator disk which is used for the open propellers and the duct thrust is given by a zero thickness ring around the propeller disk. (Kerwin, 2010)

The thrust created by the actuator disk can be calculated either if the pressure jump at the propeller disk is known or if both the incoming and induced flow velocities are known. In practice the actuator disk is used for introducing the propeller effect on the RANS equations by defining a force or pressure distribution for the disk and scaling it to give the required thrust and torque. The force distribution can be uniform, have radial force distribution or have a changing force distribution both in radial and circumferential directions. Since the actuator disk only introduces a force distribution, its accuracy depends on the method used for the force distribution calculation and how detailed force distribution is given to the actuator disk. (Sánchez-Caja and Pylkkänen, 2007)

The force distribution can be obtained for example by propeller simulations with lifting line method (Sánchez-Caja and Pylkkänen, 2007) or boundary element method (BEM) (Bosschers et al., 2008; Ripjkema et al., 2013), which are discussed in next sections. It is also possible to define the force distribution without any propeller simulation, for example with the circulation distribution defined by Hough and Ordway (1964), and then only a basic information about propeller is needed (Zhang, 2010).

3.1.2 Lifting line and lifting surface models

The lifting surface and lifting line are potential flow methods which in the ship hydrodynamics are used for the propeller design and analysis. In the lifting surface method the propeller blades are presented by lifting surfaces having propeller specific vortex sheet distributions while the lifting line model is a simplification of the lifting surface model and the propeller blades are presented with the lifting lines having line vortex distributions. In both methods the propeller induced velocities and propeller forces can be solved based on the vorticity distribution. The methods have continuous vortex distributions, which are often discretized for computational purposes with panels. Then instead of continuous vortex distributions, approximated constant vortex values are given on each panel. These discretized calculation models are called vortex lattice solutions. (Kerwin, 2010)

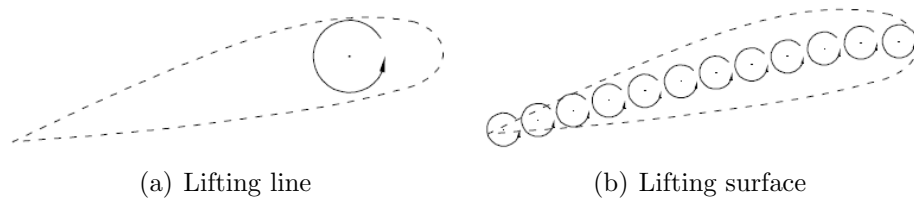


Figure 3.1: Lifting and lifting surface presentations for foil sections

The duct can be implemented to the lifting line presentation with an image vortex system, which creates such a boundary at the duct surface, that no flow penetrates through it. The boundary is created by modeling the duct mean line with a system of ring vortices and additionally the duct thickness can be taken into account with a system of ring sources. (Stubblefield, 2008) With the lifting line and surface models the tip gap can be modeled or the gap can be ignored. For example Van Houten (1986) developed a model for tip gap flow calculation but in an open source propeller design and analysis code OPENPROP v 2.4 no duct gap is taken into account (Epps, 2010).

3.1.3 Boundary element methods

The boundary element methods, or panel methods, are potential flow methods which can be used in the propeller modeling and preliminary ship resistance simulations. In a propeller simulation by BEM the propeller is discretized with panels and depending on the method a distribution of either sources and vortices, sources and dipoles or only vortices is defined on the panels. The propeller forces are calculated by solving either the velocities or velocity potentials and further solving the pressures and forces from the velocities. (Kerwin, 2010) A duct can be included to a panel method by creating panels for the duct geometry and the tip gap flow can be modeled with panels generated for the tip vortex.

A panel method for the ducted propellers was developed by Kerwin et al. (1987) and has been further inspected for example by Baltazar and Falcão de Campos (2009) and Baltazar et al. (2012). Baltazar and Falcão de Campos (2009) concentrated on the effect of the gap modeling when Baltazar et al. (2012) tested different wake calculation methods.

3.1.4 RANS simulation

The most detailed and physically correct description of the propeller flow is obtained with the RANS simulation. The previously reviewed methods were potential flow based, i.e. the flow was assumed to be irrotational and inviscid while in RANS simulations no such simplifications are done. Additionally, while in lifting line and BEM methods the solution is calculated only on the propeller surface and in the propeller wake, in the RANS methods also the fluid is modeled.

The propeller simulation with RANS can be done time accurately or as a quasi-static computation (Siikonen, 2013). The quasi-static simulation is used in the propeller open water condition, where the inflow to a propeller is uniform, and it is enough to model a section with only one propeller blade with periodical boundary conditions at the section sides because the situation is symmetric. (Watanabe et al., 2003) However, when a propeller is located in a non-uniform wake field, the whole propeller must be modeled and a time accurate simulation is required.

In both cases, the computational domain consists of two domains, which are the domain rotating with the propeller and the static outer domain. The domains can be overlapping, as in the Chimera method, or alternatively the blocks have no overlaps or gaps between them, as in the sliding mesh method. In both sliding mesh and Chimera grid methods the propeller rotation is implemented to the flow by rotating

the propeller block in each time step so that the taken rotation angle corresponds to the actual propeller rotation rate. (Siikonen, 2013)

In the sliding mesh method the flow variables are interpolated at the interface between the static and sliding meshes. (Siikonen, 2013) In the Chimera grid, or dynamic overset grid, the propeller is modeled as a separate sub-block which is then set on the major grid and in the domain each grid point is marked either as active, interpolated or hole point. The hole points are the points where the calculation results are discarded or the calculation is not done at all, i.e. the points inside a geometry or outside the computational domain. At the edge of the hole boundary and at the outer edge of the sub-domain, the interpolation points are defined in the major grid and in the sub-domain respectively and the information between grids is communicated via the interpolated boundary points. At the overlap region the grid points are active and the flow problem is solved as usual in both grids. (Zheng and Liou, 2003; Carrica et al., 2010) In Figure 3.2 is shown the principle of the sliding mesh and in Figure 3.3 are shown the different regions of the overlapping grids.

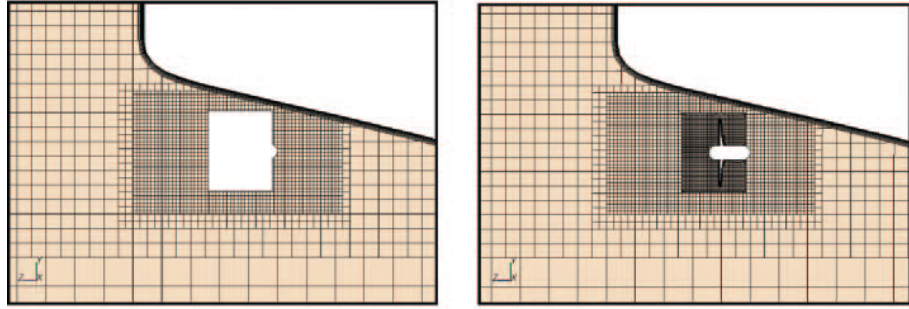


Figure 3.2: Sliding mesh. Taken from (Dhinesh et al., 2010).

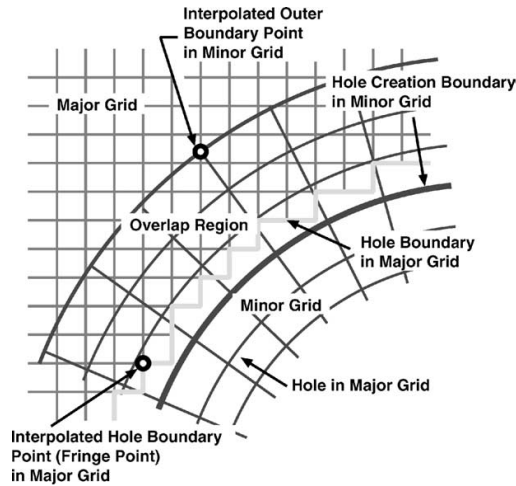


Figure 3.3: Overlapping mesh. Taken from (Zheng and Liou, 2003).

In addition to the time-accurate simulation, the sliding mesh and Chimera grid methods can be used for the quasi-static simulation. In the propeller simulation the quasi-static simulation is used either in the open water condition for final results or

in a non-symmetric situation for computing the initial state for the time-accurate simulation. In the quasi-static simulation the needed CPU (Central Processing Unit) time is reduced by using approximative boundary conditions at the boundary between the static and rotating blocks instead of actual physical boundary conditions used in the time-accurate simulation. There are two alternatives for the boundary condition approximations called multi reference frame (MRF) and mixing plane or steady-averaged method. In MRF it is assumed that only a weak interaction between the moving and fixed domains exist and the rotating block adopts the boundary conditions of one position and uses them for the whole simulation. In the mixing plane model the flow quantities are averaged circumferentially at the mesh block interfaces and the averaged values are used as boundary values. (Siikonen, 2013)

The propeller simulations with RANS have been done for example by Sánchez-Caja et al. (2008), Yu et al. (2013) and Watanabe et al. (2003), of whom Sánchez-Caja et al. (2008) and Yu et al. (2013) have used the MRF-method for the ducted propeller simulation and Watanabe et al. (2003) used both the time-accurate simulation and the steady state simulation with the open propeller. Yu et al. (2013) obtained accurate simulation results when compared to model tests results and Sánchez-Caja et al. (2008) obtained a quite accurate prediction of the total thrust whereas the torque was underestimated. Watanabe et al. (2003) obtained results with a fairly good accuracy for the thrust with both methods while the torque was overestimated.

As described in previews sections, there are many different methods for the propeller simulation and depending on the method, different amount of physical properties are taken into account in the simulation. At present the potential flow based methods are most commonly used in propeller design and analysis because of their lighter computational load while in the hull resistance simulation it is self-evident to use RANS solvers, which can predict the hull resistance accurately in the most of cases. Thus the self-propulsion schemes are based on the RANS simulation of the hull flow and the propeller calculation is included to the calculation model either by coupling RANS with a potential flow solver or by time-accurate RANS simulation. These different methods are discussed in the next section.

3.2 Self-propulsion simulation

The aim of the self-propulsion simulation is to give reliable results of the propulsion parameters and thus a reliable powering prediction. The self-propulsion models consist basically of the hull resistance simulation and propeller simulation models which are combined together.

In the simplest self-propulsion methods the propeller is modeled with an actuator disk model, which introduces a constant body force distribution to RANS equations. The body force distribution is defined separately from the RANS solver and thus the methods with the actuator disk are called coupled or hybrid methods. In full RANS self-propulsion methods the actual propeller geometry is implemented to the simulation by the sliding mesh method or Chimera grid model.

3.2.1 Hybrid methods

The hybrid methods couple RANS equations with potential flow solvers and use the actuator disk model for introducing the propeller forces calculated by the potential flow solver to the RANS equations. They are relatively simple and fast when compared to the time-accurate RANS simulation and can thus be effective design tools.

In the simplest hybrid self-propulsion models the propeller force distribution is given to the actuator disk at the beginning of the simulation and is not updated during the computation. Thus the force distribution is defined based either on the open water condition or nominal wake obtained from the resistance test. Hence the self-propulsion point is not reached as the hull-propeller interaction both changes the wake field where the propeller operates and influences the hull resistance. To obtain more realistic results, the correct force distribution of the propeller is searched with an iterative process where the general idea is to update the wake field used in the propeller simulation program and calculate a new force distribution which is then updated to the actuator disk in the RANS model. The iteration procedure is repeated until the wake field does not change anymore, i.e. until the wake field obtained is the effective wake field. In addition to updating the force distribution, also the required thrust and torque values are updated if the ship resistance has changed. (Sánchez-Caja and Pylkkänen, 2007)

The self-propulsion simulations with hybrid methods have been done for example by Bosschers et al. (2008) and Ripjkema et al. (2013) by using BEM for the propeller simulation and Sánchez-Caja and Pylkkänen (2007) by using a lifting line method. Also Tahara et al. (2006), Kawamura et al. (1997) and Phillips et al. (2009) have used a potential flow based solvers for propeller performance calculation and coupled it with a RANS solver.

3.2.2 Full RANS simulation

The self-propulsion simulation with a hybrid method is effective, since only a constant source term is added to a RANS hull flow solution. The propeller simulation with a potential flow solver is fast and thus updating the actuator disk force distribution does not lengthen the computation time significantly. Even though the use of the potential flow solver makes the computation quick, it has also its disadvantages. For example the viscous effects on the propeller are taken into account only with approximative viscous force coefficients and moreover the accuracy of the hybrid method depends on the accuracy of the propeller calculation program and whether the actuator disk model can adopt both radially and circumferentially non-uniform thrust and torque distributions. In the full RANS simulation these aspects are not critical since the propeller geometry and viscous effects are directly included in the simulation. Instead the different time scales in the propeller and hull flows and heavy computation can cause difficulties.

In the full RANS self-propulsion simulation the propeller is added to the computation either by sliding mesh model or Chimera grid model discussed in Chapter 3.1.4 and the simulation is done as a time-accurate simulation. In the coupled methods the self-propulsion point is reached by updating the wake field for the propeller simulation tool while in the full RANS simulation the self-propulsion point is by

tradition searched in the same way as in the model tests, i.e. several simulations are run with different propeller rotation rates and the self-propulsion point is estimated by interpolating from the points closest to the real self-propulsion point (Carrica et al., 2010). However, the time-accurate simulation requires a lot of CPU time and thus more effective methods for finding the self-propulsion point have been developed. These methods, called speed controllers, basically monitor the total resistance and propeller thrust and based on these update the propeller rotation rate.

The simulations with speed-controllers has been done by Carrica et al. (2010), Carrica et al. (2011) and Dhinesh et al. (2010), where Carrica et al. (2010) and Carrica et al. (2011) used the Chimera grid method for the propeller implementation and Dhinesh et al. (2010) used the sliding mesh method. A simple way for checking the self-propulsion model is to do a self-propulsion simulation with a predefined propeller rotation rate for a vessel which self-propulsion point is already known from the model tests. This kind of simulation has been done by Gao et al. (2012) and Zhang (2010) with the sliding mesh method. The accuracy of the self-propulsion results with the different full RANS computation models vary when compared to model test results. The maximum difference to the model test results in the referenced articles is in the propeller rotation rate not more than 4 % and in the propeller thrust not more than 3 %.

In this chapter the different propeller simulation models have been described, including both the potential flow and RANS models. The self-propulsion schemes coupling the RANS solvers and potential flow solvers for the propeller have been shortly introduced as well as the time-accurate self-propulsion models. In the next chapter the test case used is presented and the procedure for the propeller pitch-diameter ratio and propeller rotation rate optimization used in the propeller choice is described.

Chapter 4

Test case

The purpose of this master's thesis is to test the full RANS self-propulsion simulation of FINFLO and to examine the ducted propeller performance in a large vessel. The study is done with a case vessel which is modified from an existing hull form which has a conventional open propeller. The obtained simulation results are compared to the results of the original hull and propeller arrangement. As the model test and simulation results of the original vessel are obtained in the model scale, the simulations with the modified vessel are also conducted in the model scale. In this chapter the test case is introduced and the choice of the duct-propeller combination is justified.

4.1 Hull form

A large vessel with an existing model test data and RANS simulation results is chosen as a comparison case. The comparison vessel A has a conventional open propeller and a rudder and the test case vessel B is obtained by modifying the original vessel A. The conventional propeller and rudder are replaced with the propeller and steerable duct and the propeller diameter is kept the same. In order to fit the ducted propeller to the ship, modifications are needed for the aft hull shape. First, the propeller shaft is lifted so that the duct bottom is located above the hull base line. Second, the propeller is moved aft-wards so that there is a gap between the duct top and the hull. Once the location of the ducted propeller is determined, the skeg is reshaped to suit the new propeller position. In the modifications the ship length between perpendiculars L_{PP} is kept constant and the ship wetted surface area S and displacement ∇ are slightly increased, as shown in Table 4.1. A sketch of the modifications made is shown in Figure 4.1.

Table 4.1: Ship reference values

		Vessel A	Vessel B	Difference
L_{PP}	[m]	176.65	176.65	0.0 %
S	[m ²]	3 870	3 945	1.94 %
∇	[m ³]	42 890	42 970	0.18 %
D	[m]	6.0	6.0	0.0 %
V_s	[kn]	14.0	14.0	0.0 %
Fn	[-]	0.1714	0.1714	0.0 %

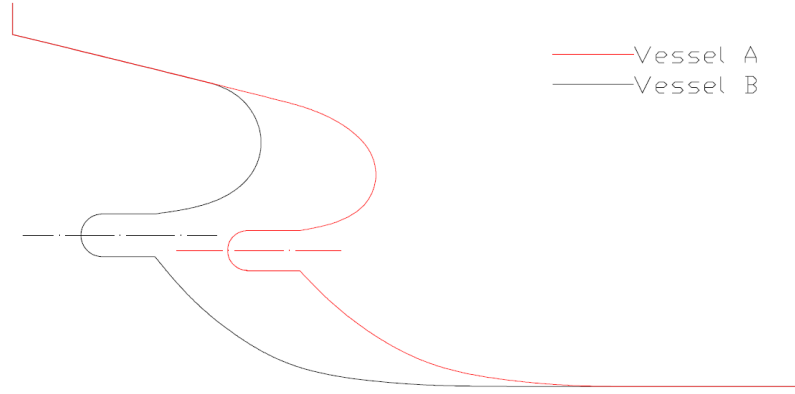


Figure 4.1: Sketch of the aft ship modifications

4.2 Duct

The duct and propeller are chosen from the Wageningen Ka-series. The duct shape is chosen to be 19A, which is the most common duct shape from Wageningen series designed for having a good forward performance. The duct profile 19A is shown in Figure 4.2 and the detailed description of the duct geometry is given in Appendix A. The propeller is located at the mid-plane of the duct and the tip gap between the propeller blade tip and duct inner surface is approximately 0.4 % of the propeller diameter, which is similar to the tip gap used in the model tests at NSMB (Oosterveld, 1970).

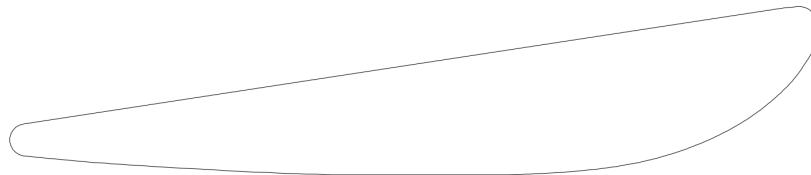


Figure 4.2: Profile of the Wageningen nozzle 19A

4.3 Propeller

The propeller is chosen from the propellers tested in the nozzle 19A, which means that there are four possible propellers, Ka3-65, Ka4-55, Ka4-70 and Ka5-75, which have the model test data and geometry specifications available. In order to choose the most suitable propeller for the vessel B, the propeller efficiencies and the danger of harmful propeller excitations at the optimal propeller rotation rates are studied. The study is done by first searching the optimal propeller rotation rates and pitch-diameter ratios for each propeller and next calculating the propeller pressure forces based on the optimal propeller rotation rates. Finally the propeller with the low danger of vibration problems with the best efficiency is chosen.

4.3.1 Propeller rotation rate and pitch optimization

The optimal values for the propeller rotation rate n and pitch-diameter ratio P/D are searched from the propeller open water curves. The wake fraction and thrust deduction factor are estimated and the propeller diameter and the required thrust are known. Thus the propeller rotation rate is solved with the propeller thrust loading coefficient K_T , which is defined as

$$K_T = \frac{T}{\rho n^2 D^4}, \quad (4.1)$$

where n is propeller revolutions per second. The optimization procedure is simple and it is shown in Figure 4.3. First the thrust loading coefficient is calculated as a

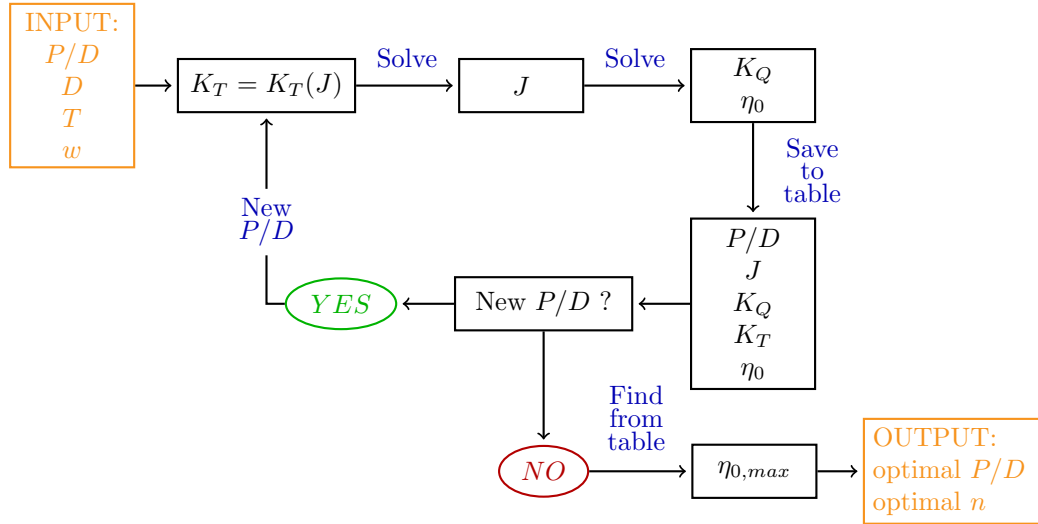


Figure 4.3: Scheme for finding the optimal propeller rotation rate and P/D , when the propeller thrust and diameter are known

function of the advance coefficient J

$$K_T(J) = \frac{T}{\rho D^2 V_A^2} J^2, \quad (4.2)$$

where

$$J = \frac{V_A}{nD}. \quad (4.3)$$

Next the cross section points of the $K_T(J)$ and the K_T given by propeller open water results are searched. The cross section points define the advance coefficients for each propeller pitch-diameter ratio and the corresponding torque loading coefficients K_Q and open water efficiencies η_0 are searched from the propeller open water curves, as shown in Figure 4.4. From the values obtained for each pitch-diameter ratio, the optimal propeller rotation rate is found by searching for the best propeller efficiency and solving the optimal propeller rotation rate from Equation (4.3). (Matusiak, 2007a)

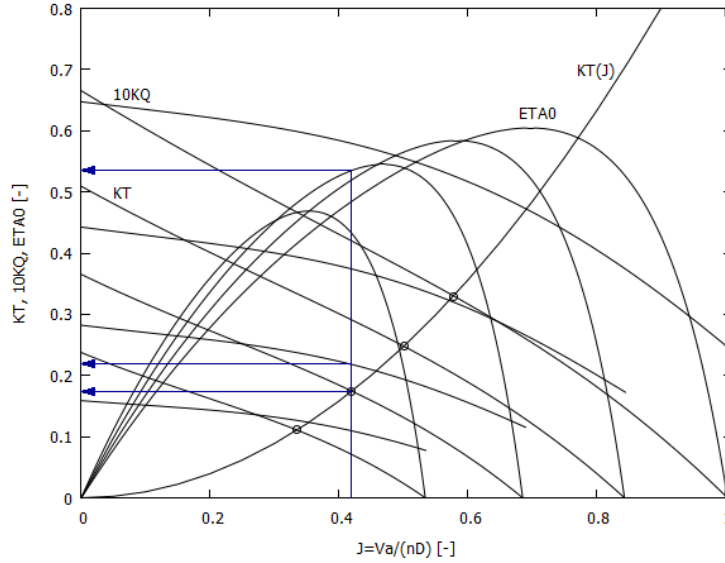


Figure 4.4: Propeller open water curves and $K_T(J)$

In the propeller optimization the required power, the ship wake field and the propeller open water curves must be known. As in this thesis the choice of the propeller is done before any simulation is done with the new hull form, the required power and the wake fraction are estimated based on the model test results of the original hull. It is approximated that the rudder creates 3 % of the hull resistance and thus the required power of the new hull is estimated to decrease by 3 % from the power demand of the original hull form and the Taylor wake fraction is kept the same as in the original hull.

The best efficiency is achieved with the propeller Ka3-65 and the lowest efficiency with the propeller Ka5-75. The differences are however small and the largest difference is less than 1.5 %. The difference between the four bladed propellers Ka4-55 and Ka4-70 is less than 0.5 %.

4.3.2 Propeller excitations

Other aspect to be considered when selecting the propeller is the pressure forces on the hull created by the blades of the rotating propeller passing the hull. The frequency of these pressure forces is calculated with

$$f = nZ, \quad (4.4)$$

where Z is the number of the propeller blades. The frequency should not be close to the hull girder natural frequencies since then the propeller might excite significant hull vibrations. According to American Bureau of Shipping (2006) the first natural frequencies of ships are 1 - 2 Hz and the highest significant natural frequencies are about 6 Hz. Usually the propeller revolutions are such that these frequencies are not close. However, with a three bladed propeller it is more probable than with propeller with more blades.

The conclusion of the propeller study is, that the propeller Ka3-65 would be the most efficient choice, but with the three bladed propeller the propeller excitation frequency can get quite close to the significant hull natural frequencies. In order to avoid possible vibration problems, the propeller is chosen to be the four bladed propeller Ka4-55 instead of Ka3-65 since the difference in the efficiencies is not large and the four bladed propeller is a more realistic choice. The chosen propeller Ka4-55 has the area ratio of $A_e/A_0 = 0.55$ and the best efficiency is obtained with the pitch-diameter ratio $P/D = 1.2$. A detailed description of the geometry of the chosen propeller Ka4-55 is shown in Appendix B.

In this chapter the differences of the original vessel and the test case vessel have been presented and the duct and propeller have been chosen. In Figure 4.5 the final stern arrangement with the modified aft shape and chosen ducted propeller is shown. In order to keep the ship simulation as simple as possible, the duct support is not modeled. In the next chapter the methods used in the simulation and the computational grids are described.

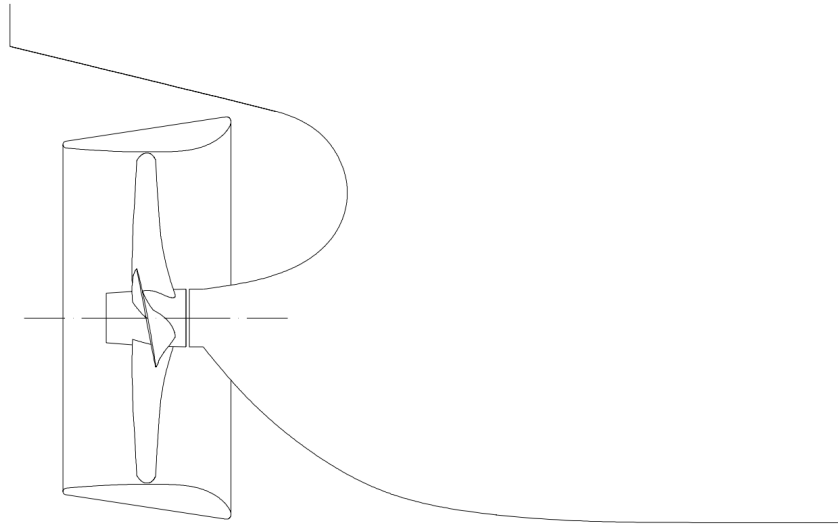


Figure 4.5: Modified stern with the chosen ducted propeller Ka4-55

Chapter 5

Methods

The ship hull and self-propulsion characteristics are tested with RANS simulations which are done with FINFLO-solver (Finflo Ltd.). The initial position of the ship is calculated with the potential flow solver v-SHALLO (HSVA). Next the basis of the ship flow simulation is described and computational models used are introduced.

5.1 Governing equations for ship flows

The description of the viscous fluid flow is given with the Navier-Stokes -equations (NS-equations) and continuity equation, which are respectively written with the tensor notation as

$$\frac{\partial u_i}{\partial t} + u_j \frac{\partial u_i}{\partial x_j} = -\frac{1}{\rho} \frac{\partial p}{\partial x_i} + \frac{1}{\rho} \frac{\partial \sigma_{ij}}{\partial x_j} + F_i \quad (5.1)$$

$$\frac{\partial u_i}{\partial x_i} = 0, \quad (5.2)$$

where σ_{ij} is the viscous stress term, u_i is the velocity component, x_i is the coordinate direction and F_i is the body force component (source component). The viscous stress term is defined as

$$\sigma_{ij} = \mu S_{ij} = \mu \left(\frac{\partial u_i}{\partial x_j} + \frac{\partial u_j}{\partial x_i} \right), \quad (5.3)$$

where μ is the dynamic viscosity and S_{ij} is the rate of strain tensor. The NS-equations and continuity equation create the basis for the ship flow simulation, the NS-equations describing the momentum of the viscous flow and the continuity equation taking care of the mass balance. In Equations (5.1) and (5.2) the density ρ is assumed to be constant, which is a good approximation for the ship flows. In addition to the NS- and continuity equations there is an equation for the energy conservation, but it is usually not included in the ship flow simulation and is thus not discussed here. (Larsson and Raven, 2010)

The flow simulations are done in different situations with varying requirements for the accuracy and CPU time and hence the NS-equations have been simplified and/or modified in different ways. For example, the simplified equations are used in the potential flow theory whereas the RANS-equations are obtained by modifying the presentation of the flow velocities. However, though the momentum equations may change, the continuity equation remains the same. (Larsson and Raven, 2010)

The momentum equations and continuity equation are generic equations and hence boundary conditions are needed to specify the case in line. In the ship flow simulation these specifying boundary conditions are defined at the free surface and on the solid surfaces, i.e. on the hull surface and on the possible appendages. The hull surface boundary conditions define that there is no flow through the hull surface (no penetration condition) and the tangential velocity on the hull surface is equal to the surface velocity (no-slip condition). On the free surface the boundary conditions needed are the kinetic, or dynamic, and kinematic boundary conditions. The dynamic boundary condition says that the pressure on the free surface is equal to atmospheric pressure while the kinematic boundary condition says that the particles on the free surface remain there. The dynamic and kinematic boundary conditions can be respectively written as

$$p|_{z=h} = p_a \quad (5.4)$$

and

$$w = \frac{Dh}{Dt}, \quad (5.5)$$

where h is the free surface height, p_a is the atmospheric pressure and w is the vertical velocity component. (Matusiak, 2005; Larsson and Raven, 2010)

Above the generic equations for the ship flow simulation together with the boundary conditions have been presented. In this thesis the NS-equations as such are not used, but two different set of equations derived from NS-equations are applied. The potential flow model is obtained with simplifications made on the NS-equations and the RANS-equations are obtained by re-formulating the velocity components of the NS-equations. Next these two flow descriptions are presented.

5.1.1 Potential flow theory

In the potential flow theory the flow is assumed to be incompressible, inviscid and irrotational, which means that the density of the fluid is constant (incompressibility), the kinematic viscosity is neglected (inviscid fluid) and the fluid particles do not have angular velocities, i.e. spin (irrotational fluid). The assumptions can be respectively written as

$$\rho = C \quad (5.6)$$

$$\nu = 0 \quad (5.7)$$

$$\nabla \times \vec{V} = 0. \quad (5.8)$$

In reality the flow described in the potential flow theory does not exist but nonetheless the theory is widely used because it enables quite simple and fast computational models. In practice the potential flow theory is considered to be suitable in situations, where the viscous effects are limited to a very thin layer close to the solid surfaces and the flow in the global scale is of interest. (Sánchez-Caja, 2013)

In the potential flow theory the momentum of the fluid is described with the Euler equations, which are obtained by neglecting the viscosity from the NS-equations and are written as

$$\frac{\partial u_i}{\partial t} + u_j \frac{\partial u_i}{\partial x_j} = -\frac{1}{\rho} \frac{\partial p}{\partial x_i} + F_i. \quad (5.9)$$

The Euler equations can be further modified to the Bernoulli equation, which for the irrotational, steady state flow is

$$\frac{1}{2}\rho V^2 + \rho gz + p = C. \quad (5.10)$$

The Bernoulli equation is constant along a streamline in the inviscid region and it is usually written at the point of interest and at a point far field, where the pressure and velocity are known. (Larsson and Raven, 2010)

In potential flow applications the Bernoulli equation and the continuity equation are written using velocity potentials ϕ instead of velocities. The velocity potentials are used for describing the velocity field and they are defined as

$$\vec{V} = \frac{\partial \phi}{\partial x} \vec{i} + \frac{\partial \phi}{\partial y} \vec{j} + \frac{\partial \phi}{\partial z} \vec{k} = \nabla \phi \quad (5.11)$$

and the resulting continuity and Bernoulli equations are respectively

$$\frac{\partial^2 \phi}{\partial x^2} + \frac{\partial^2 \phi}{\partial y^2} + \frac{\partial^2 \phi}{\partial z^2} = \nabla^2 \phi = 0 \quad (5.12)$$

and

$$\frac{1}{2} \nabla \phi \cdot \nabla \phi + \frac{\rho}{p} + gz = C. \quad (5.13)$$

The advantage of the use of velocity potentials can be seen from the newly obtained continuity equation (5.12), which is the Laplace equation. There are already existing fundamental solutions for the Laplace equation and additionally the equation is homogeneous and linear, which means that the superposition principle can be used for the velocity potentials. Thus also a complex flow field can be described by a composition of simple velocity potentials. The common velocity potential types are named as sources, dipoles and vortices, of which the sources and dipoles are mainly used in panel methods while the vortices are important in lifting line and lifting surface methods. The velocities can be solved from the continuity equation and further the pressures from the Bernoulli equation. (Larsson and Raven, 2010)

In the ship hydrodynamics, the potential flow solvers are used for the propeller simulation, as described in Section 3.1, and for the hull flow simulation. In the hull flow simulation panel methods, where the hull surface and free-surface are discretized with panels, are used. The resistance of the ship cannot be estimated reliable with the potential flow theory since the viscous effects and the turbulence are neglected. Instead the potential flow simulations are a useful tool for optimizing the wave pattern, even though the stern waves are usually overestimated. It is also possible to evaluate the dynamic position of the hull, i.e. the dynamic sinkage and trim, with a panel method.

5.1.2 RANS equations

In the potential flow theory significant simplifications are made with the assumptions of inviscid, incompressible and irrotational fluid. In reality the fluid is always viscous

and the flow characteristics change depending on the viscosity and flow velocity. The dependence is expressed with the non-dimensional Reynold number Rn , which is

$$Rn = \frac{uL}{\nu}, \quad (5.14)$$

where L is the characteristic dimension. With low Reynold numbers the flow is laminar and when the Reynold number gets high enough, the flow transforms to a turbulent flow. In a laminar flow individual tracks of flow particles can be followed and streamlines follow smoothly surface curvatures whereas in turbulent flows the particle tracks are random and the flow velocities and pressures fluctuate. The ship hull flow is always turbulent and hence the turbulence simulation has an important role in the ship simulation. (Matusiak, 2007b)

The turbulent flow problems can be solved either with the time accurate simulation of the turbulence or by treating the turbulence as a steady state phenomenon and calculating the effect of turbulence with a turbulence model. The method for the time accurate simulation of the turbulence is called DNS (Direct Navier-Stokes) where the actual velocities are solved from the NS-equations. In order to get correct results from DNS, all the turbulent time scales must be modeled, i.e. also the smallest turbulent fluctuations must be caught. Thus a fine mesh and small time steps are required and a lot of CPU time is needed for the solution. In practice DNS simulation is possible only for flows with low global Reynolds numbers. Other turbulence simulation models which use the NS-equations are for instance LES (Large Eddy Simulation) and its lighter version DES (Detached Eddy Simulation). In LES and DES only a part of the turbulence is solved time accurately, in the same way as in DNS, and the turbulence scales smaller than the grid resolution are modeled by place-averaged equations. (Siikonen, 2013)

A common practice is to use instead of DNS, LES or DES some turbulence model which is based on the time-averaging of the turbulent flow. The usage of these turbulence models requires a modification of the NS-equations to a such form, that the effect of the turbulence stands out from the equations. The modified form is the RANS-equations, where the turbulent flow velocities are divided to average and fluctuating velocity components, \bar{u} and u' respectively

$$u = \bar{u} + u'. \quad (5.15)$$

The velocity components are also shown in Figure 5.1. Similarly the pressure is divided to average and fluctuating components, \bar{p} and p' respectively

$$p = \bar{p} + p'. \quad (5.16)$$

The velocity and pressure components from Equations (5.15) and (5.16) are substituted to NS-equations (5.1) and after substitution a time average is taken from the equations. As a result the RANS equations are obtained

$$\frac{\partial \bar{u}_i}{\partial t} + \frac{\partial \bar{u}_j \bar{u}_i}{\partial x_j} = -\frac{1}{\rho} \frac{\partial \bar{p}}{\partial x_i} + \frac{1}{\rho} \frac{\partial}{\partial x_j} (\sigma_{ij} + R_{ij}) + F_i, \quad (5.17)$$

where R_{ij} is the Reynolds stress and overline marks the time average. The Reynolds stress is a correlation between fluctuating velocity components and is defined as

$$R_{ij} = R_{ji} = -\rho \overline{u'_j u'_i}. \quad (5.18)$$

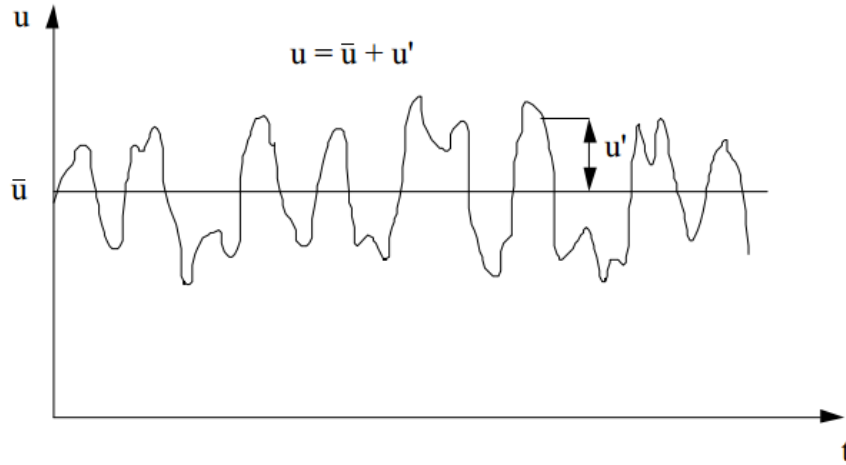


Figure 5.1: Components of turbulent velocity. Taken from (Mikkola, 2013)

(Larsson and Raven, 2010) The Reynolds stress tensor in Equation (5.18) introduces six new unknowns to the equations. In the laminar flow the fluctuating velocities vanish and the RANS-equations return to the NS-equations. The new unknowns are solved with turbulence models and hence the goal of turbulence modeling is to create sensible models for the Reynolds stress calculation. (Matusiak, 2007b)

Plenty of different turbulence models have been developed and the most used models are two-equation models, which have two transport equations for turbulent quantities. For example the widely used $k - \epsilon$ -models and $k - \omega$ -models have one equation for solving the turbulent kinetic energy k and one equation for solving either the rate of dissipation of turbulent kinetic energy ϵ or the specific rate of dissipation of turbulent kinetic energy $\omega = \epsilon/k$. In the ship simulation the complex aft shape and as a consequence flow phenomena at the aft region are challenging for the turbulence modeling. The $k - \epsilon$ -model has tendency for smoothing the irregularities of the ship wake out while the $k - \omega$ -model gives better results, but it is sensitive to changes of k and ω and thus it is difficult to find stable boundary conditions at the outer edge. To avoid these problems the turbulence models combining $k - \epsilon$ - and $k - \omega$ -models ($k - \epsilon/k - \omega$ -models) in a suitable way, are often used in the ship hydrodynamics. (Larsson and Raven, 2010) In these models the $k - \omega$ -model is used in the boundary layer, the $k - \epsilon$ -model outside the boundary layer and the change from one model to another is done with a blending function (Siikonen et al., 2010). In addition to the mentioned turbulence models, there are also for example models with only zero or one transport equation, algebraic turbulence models and Reynold stress models (RSM). More information about turbulence models can be found for example from (Wilcox, 2006). (Larsson and Raven, 2010)

The turbulence is a complex phenomenon and thus the turbulence models include different assumptions and empirical coefficients. The fundamental assumption, which is made in almost all turbulence models, is the Boussinesq assumption. It assumes that the Reynolds stresses can be calculated with

$$R_{ij} = \mu_T S_{ij} - \frac{2}{3} \rho k \delta_{ij}, \quad (5.19)$$

where μ_T is the turbulent viscosity or eddy viscosity and δ_{ij} is the Kronecker delta.

The turbulent kinetic energy is defined as

$$k = \frac{1}{2} \overline{u'_i u'_i} \quad (5.20)$$

and the Kronecker delta is

$$\delta_{ij} = \begin{cases} 1 & \text{if } i = j \\ 0 & \text{if } i \neq j \end{cases} \quad (5.21)$$

The Boussinesq assumption in Equation (5.19) is obtained by first assuming that the Reynolds stresses can be calculated in the same way as viscous stresses σ_{ij} , when the molecular viscosity μ is replaced with the eddy viscosity μ_T

$$R_{ij} = \mu_T S_{ij}, \quad (5.22)$$

where the eddy viscosity μ_T is not constant but depends on the location and flow characteristics. With this assumption the sum of the diagonal Reynolds stress terms R_{ii} is zero according to the continuity equation while according to Equation (5.18) it is not. In order to include them to the Reynolds stress calculation, next the sum of the diagonal terms is expressed with the turbulent kinetic energy k as

$$R_{ii} = -2\rho k \quad (5.23)$$

and added to Equation (5.22) with the Kronecker delta, so that they are non-zero only at the diagonal of the R_{ij} tensor. Additionally R_{ii} is divided by three since R_{ii} is the sum of three terms. The turbulence models aim at modeling the turbulent quantities, such as k , ϵ and ω , which are further needed in the modeling of the eddy viscosity. (Larsson and Raven, 2010)

Together with the turbulence simulation, the free surface computation is important in the ship flow simulation. At present there are two kind methods for the free surface modeling, which are the interface tracking methods (surface tracking methods) and the interface capturing methods. In the surface tracking methods a time stepping approach is used, in which the free surface is updated after each time step. During one time step, first the free surface is kept constant while the flow below the free surface is computed and at the end of each iteration round the new free surface height is solved and the volume mesh is updated to correspond the newly obtained free surface. When the flow below the fixed free surface is computed, the dynamic boundary condition ($p|_{z=h} = p_a$) is applied to the free surface whereas the kinematic boundary condition ($w = Dh/Dt$) is used for solving the new free surface. (Larsson and Raven, 2010)

The interface capturing methods differ from the interface tracking methods significantly. In the interface capturing methods also the air above the free surface is modeled. The two most used interface capturing methods are the Volume of Fluid (VOF) method and the Level Set method. In VOF method a void fraction c is defined to tell how much of the volume of a cell is water, so that if $c = 1$, the cell is full of water and if $c = 0$, the cell contains only air. During the simulation the void fraction is solved from a transport equation and the free surface location is defined based on the value of c , usually at $c = 0.5$. In Level Set method a scalar function ϕ is defined for representing the distances of the fluid particles to the free surface. Usually value $\phi = 0$ is given on the free surface, negative values in the

air and positive in the water. The scalar function values are fixed to fluid particles and transported with them. The transportation is solved from a transport equation defined for ϕ and since the scalar values are fixed to particles, the free surface should always be found at $\phi = 0$. (Larsson and Raven, 2010) In Figure 5.2 are shown the principles of the VOF and Level Set methods.

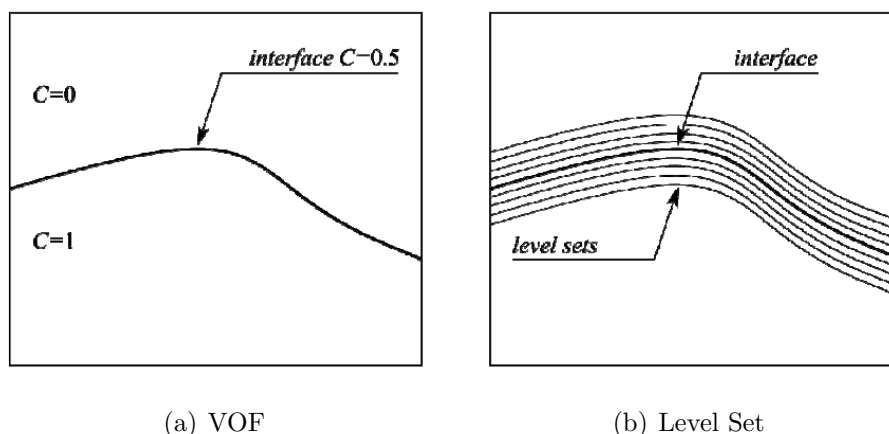


Figure 5.2: Surface capturing methods. Taken from (Mikkola, 2013)

5.2 Ship flow simulation tools

In the previous section the equations used in the potential flow and RANS simulations were described. The solvers used in this study are the potential flow solver ν -SHALLO and the RANS solver FINFLO. Next the solvers are shortly introduced and the computation grids used are described together with the boundary conditions applied.

5.2.1 Potential flow solver ν -Shallo

ν -SHALLO is a potential flow solver which can be used for the wave resistance simulation. It applies fully non-linear boundary conditions for the free surface elevation and can be used for calculating the dynamic sinkage and trim. The fully non-linear boundary conditions of the free surface mean that effect of curved flow along the hull surface is taken into account.

For the calculation, the hull surface and free surface are discretized with panels. The initial mesh of the hull is imported to ν -SHALLO and the free surface mesh is created automatically by ν -SHALLO. The hull surface mesh is cut to wetted and dry parts based on the free-surface level as is shown in Figure 5.3(b) and only the wetted part of the mesh is used in calculation and it is updated during the simulation. (Marzi and Hafermann, 2008)

The flow field is described with velocity potentials using sources and parallel free stream velocity. Each panel has a source and the total velocity potential of each panel is a composition of the free stream velocity potential and all panel sources.

For example the velocity potential at the panel j is written as

$$\phi_j = -Ux + \sum_i m_i \frac{-4\pi}{r_i}, \quad (5.24)$$

where m_i is the point source strength, r_i is the distance between the point source and point j where the potential is calculated.

The dynamic position of the ship is obtained by calculating vertical components of the body forces from the pressures and by updating the wetted part of the hull grid so that the equilibrium equation is satisfied. The wave elevation is calculated with the Bernoulli equation and the free-surface mesh is updated to correspond the new free-surface. In Figure 5.3 are shown examples of the mesh before simulation and the updated wetted surface mesh after several iterations. (Marzi and Hafermann, 2008)

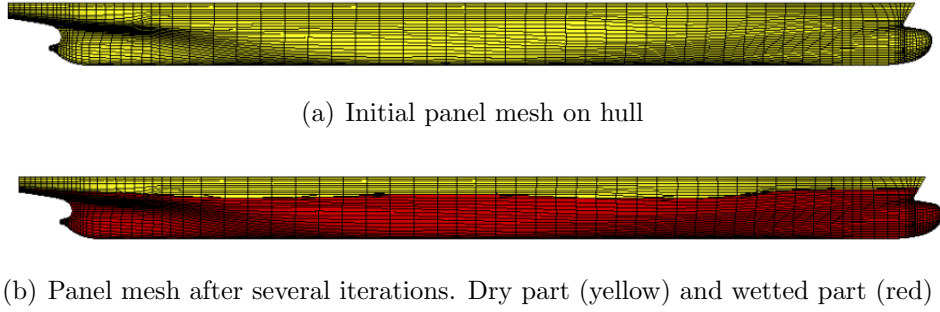


Figure 5.3: Hull surface panels before and after several iterations. Taken from (Marzi and Hafermann, 2008).

5.2.2 RANS solver FINFLO

There is a large variety of different RANS solvers suitable for the ship flow simulation, for example STAR-CCM+ (CD-adapco), FINETTM/Marine (NUMECA), CFDSHIP-IOWA (IIHR), FINFLO (Finflo Ltd.) and FLUENT (ANSYS, Inc.). In this thesis FINFLO solver is used for the resistance and self-propulsion simulations. FINFLO is capable of computing the ship which is free to trim and sink, i.e. which has two degrees of freedom. Often though the trim and sinkage are predefined and the computation is done with the fixed ship. The propeller can be implemented to the calculation by the actuator disk model, as done in (Lakatos, 2013), or by the Chimera grid or sliding mesh method. The free surface calculation is done by a surface tracking method or kept constant. (Finflo Ltd., 2012)

In FINFLO the RANS equations together with the equations for the turbulent quantities and scalar transport equation are presented as

$$\frac{\partial U}{\partial t} + \frac{\partial F_{tot}}{\partial x} + \frac{\partial G_{tot}}{\partial y} + \frac{\partial H_{tot}}{\partial z} = Q, \quad (5.25)$$

where F_{tot} , G_{tot} and H_{tot} are the flux vectors in x , y and z directions respectively, Q is the source term and U includes the conservative quantities to be solved and is given as

$$U = (\rho, \rho u, \rho v, \rho w, E, \rho k, \rho \epsilon, \rho \phi)^T, \quad (5.26)$$

where E is the total internal energy and ϕ is the scalar function. In FINFLO the flux terms are further divided to inviscid and viscous parts, for example in x -direction the total flux is divided to $F_{tot} = F + F_v$, where F is the inviscid and F_v is the viscous flux term. (Finflo Ltd., 2012)

FINFLO uses the finite volume method (FVM) for spatial discretization, which means that the flow equations are solved in the integral form, which is

$$\frac{d}{dt} \int_V U dV + \int_S \vec{F}(U) \cdot d\vec{S} = \int_V Q dV \quad (5.27)$$

where V is an arbitrary control volume and S its boundary. When the integrals are solved for a computational cell i , the equation for the cell is obtained to be

$$V_i \frac{dU_i}{dt} = \sum_{Faces} (-S\hat{F} + V_i Q_i), \quad (5.28)$$

where the flux for a face, \hat{F} , is calculated with

$$\hat{F} = n_x F_{tot} + n_y G_{tot} + n_z H_{tot} \quad (5.29)$$

where n_x , n_y and n_z are the surface unit normals. The inviscid and viscous fluxes are solved separately. The inviscid fluxes are obtained by Roe's flux difference splitting method, which is an approximative Riemann solver. In Roe's method the right and left values, U^r and U^l respectively, are needed at the cell faces. These values are interpolated with the MUSCL approach and the van Albada limiter is used for avoiding peaks in the solution. The MUSCL schemes for left and right values are

$$U_{i+1/2}^l = U_i + \frac{\phi(R_i)}{4} [(1 - \kappa)(U_i - U_{i-1}) + (1 + \kappa)(U_{i+1} - U_i)] \quad (5.30)$$

$$U_{i+1/2}^r = U_{i+1} + \frac{\phi(R_{i+1})}{4} [(1 + \kappa)(U_{i+1} - U_i) + (1 - \kappa)(U_{i+2} - U_{i+1})], \quad (5.31)$$

where κ is the parameter used for controlling the discretization type, subscripts mark the calculation points, $\phi(R)$ is the limiter and R is the relation of the change in the conservative quantity in the sequential nodes. (Finflo Ltd., 2012) For the



Figure 5.4: Cells used for right and left value interpolation with MUSCL approach. Cells used for left and right values are marked with L and R respectively.

propeller flow the convective terms are obtained with an upwind-biased method and the pressures are computed as central differences with a Rhie-Chow -type dissipation term. In Figure 5.4 are shown the nodes used for right and left values.

The viscous fluxes are calculated by using the thin-layer approximation, where the derivatives in a direction perpendicular to a solid surface are calculated by using only the perpendicular components. The thin layer approximation can be written as

$$\left(\frac{\partial u}{\partial x}\right)_i \approx \frac{(n_x u)_{i+1/2} - (n_x u)_{i-1/2}}{d_i}, \quad (5.32)$$

where d_i is the cell thickness and the velocities at the cell faces are calculated as average values from the cell values. (Finflo Ltd., 2012)

In FINFLO a turbulent flow is computed with a turbulence model. There are available for example Algebraic models, two equation models and RSM models and the description of these can be found in (Finflo Ltd., 2012). In this thesis the two equation model SST $k - \omega$ (Shear Stress Transport) is applied. The SST $k - \omega$ -model is a $k - \epsilon/k - \omega$ -model where an additional limitation is applied to the eddy viscosity μ_T in order to avoid non-physical values close to the wall. (Siikonen et al., 2010)

The RANS simulation takes a lot of CPU time, and thus different computation acceleration schemes are included in FINFLO. The methods used are the coarse-grain parallelization and full multi-grid (FMG) method. In coarse-grain parallelization the simulation problem is divided for multiple computer cores. Each core solves its own flow problem independently of other processes and after each iteration round, the cores change information needed in boundary conditions and convergence monitoring with each other. In FMG the calculation is done on several grid levels starting from the coarsest grid and proceeding to the finest. On each grid level a converged solution is calculated and then used as an initial guess for the finer grid level. (Siikonen, 2014)

5.2.3 Grid generation

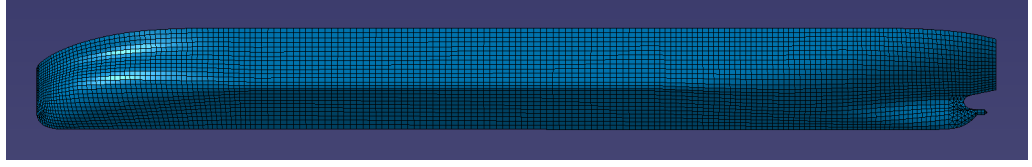
The flow simulations in ν -SHALLO and FINFLO require different computational grids. In ν -SHALLO only the hull surface and free surface are discretized while in FINFLO also the fluid domain is modeled.

The hull panelization for ν -SHALLO simulation is done with Catia V5-software. For the panelization the hull surface is divided into patches so that the panel quality can be easier controlled and the panel sizes adjusted to be suitable for calculation in different areas. The panelization is more dense at the bow and skeg areas, whereas larger panels are used in the areas with simpler geometry. The created panel mesh has both rectangular and triangular panels so that there are no panels with a bad aspect ratio. The total amount of the panels on the half hull is 4691. In Figure 5.5 are shown the hull division to patches and the hull panelization.

In the panelization for the potential flow solver only the reasonable aspect ratio and panel sizes were required. The grid generation for the RANS simulation is a more complex process, since also the fluid is discretized. The volume grid must have a good quality, i.e. no negative volumes or negative skewness, and the boundary layer close to the solid walls must be taken into account so that there are enough control volumes inside the boundary layer and the heights of the first volumes are suitable. In practice about 30 computation volumes are used inside the boundary layer and outside the boundary layer the grid is coarser. The requirement for the



(a) Hull division for meshing



(b) Panel mesh

Figure 5.5: Hull surface panelization in Catia

first cell height is given with the non-dimensional distance to the wall y^+ , which is in turbulent boundary layers given as

$$y^+ = \frac{\rho u_\tau y}{\mu} \quad (5.33)$$

where u_τ is the friction velocity, which is

$$u_\tau = \sqrt{\frac{\tau_w}{\rho}}, \quad (5.34)$$

where τ_w is the wall shear stress. The non-dimensional distance y^+ at the first calculation node should be $y^+ \approx 1$ in order to obtain results with the acceptable accuracy. (Siikonen, 2013) As the wall friction velocity and consequently the y^+ values are not known before the simulation, approximative equations are used in the grid generation phase for estimating the first cell heights. There are plenty of approximative equations for the skin friction coefficient C_f , which can be found for example in (White, 2006). Once the skin friction coefficient is known, the wall shear stress can be solved from the equation

$$C_f = \frac{\tau_w}{\frac{1}{2}\rho U_\infty^2}. \quad (5.35)$$

Further, when the wall shear stress is known, the height of the first cell can be solved from Equation (5.33). (White, 2006) In this thesis the first cell height for the hull mesh is approximated according to the equation

$$y^+ \leq \frac{0.01 L_{OS}}{\sqrt{Rn_{LOS}}}, \quad (5.36)$$

where L_{OS} is the overall submerged length of the ship and Rn_{LOS} is the Reynolds number with the reference length L_{OS} .

The structured grid used in FINFLO simulations is created with Gridgen software (Pointwise, Inc.). The volume meshes are separately generated for the hull, propeller and duct and each of them consist of blocks having six faces. In the hull

volume block the hull surface is surrounded by a quarter ball shaped volume mesh with the radius of about $15 \times L_{PP}$, as shown in Figure 5.6. The block has three faces at the symmetry plane and the rest three faces are the hull surface, the free surface and the outer edge of the quarter ball. The hull volume block has $304 \times 192 \times 160$ volumes, altogether 9 338 880 volumes, where I -direction is from ship bow to aft, J -direction is from ship surface to quarter ball surface and K -direction is from ship bottom to free surface. The height of the first cell on the hull surface is $2.0 \cdot 10^{-5}$ m, which gives the approximation of non-dimensional distances to wall be $y^+ \approx 1$. After the hull volume block is generated, it is divided to 19 smaller blocks in order to be able to use coarse grain parallelization. For the self-propulsion simulation the volume mesh of the resistance simulation is mirrored.

In the same manner as the hull volume, the volume meshes are created for the propeller and duct. The propeller mesh has 7 208 960 volumes and duct mesh 6 815 744 volumes and these volume meshes are overlapping, as shown in Figure 5.7. In Figure 5.8 are shown the surface meshes of the duct and propeller behind the hull. In Table 5.1 is given number of volumes of each grid part and total amount of volumes in both simulation cases.

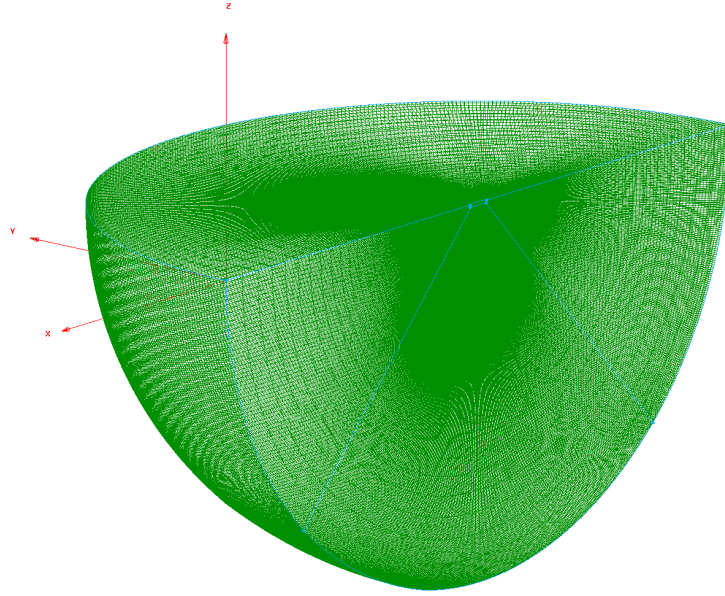


Figure 5.6: Volume mesh for resistance simulation

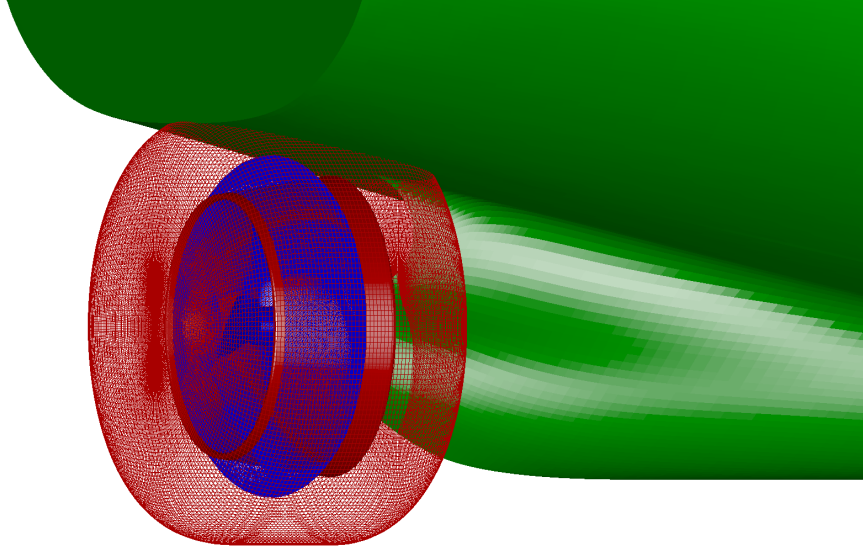


Figure 5.7: Overlapping meshes of propeller and duct used in self-propulsion simulation. The duct surface and mesh outer edge are red and the propeller surface and mesh outer edge are blue

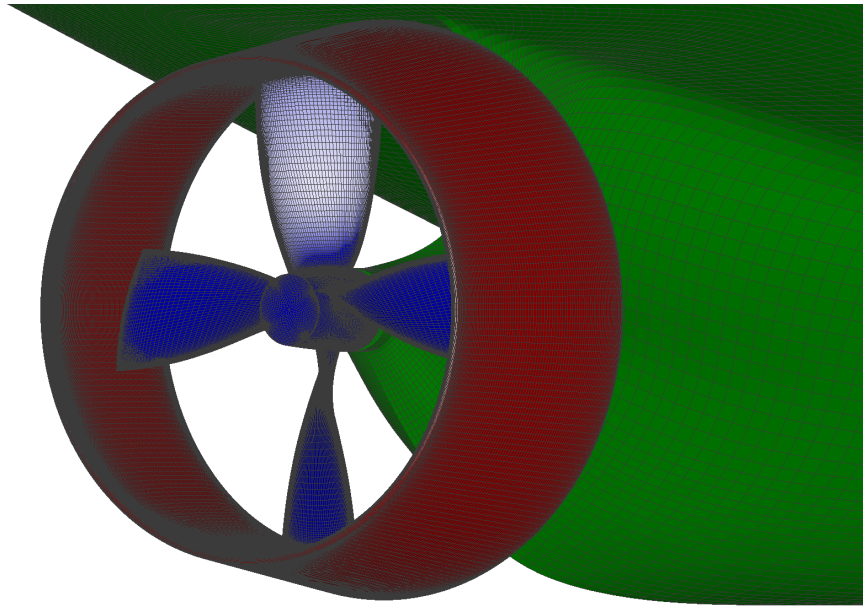


Figure 5.8: Meshes of propeller and duct used in self-propulsion simulation

Table 5.1: Grid dimensions

		Blocks	Volumes
Resistance simulation	Half hull	76	9 338 880
	Total	76	9 338 880
Self-propulsion simulation	Whole hull	152	18 677 760
	Propeller	12	7 208 960
	Duct	6	6 815 744
	Total	170	32 702 464

When the computational grids for FINFLO are generated, the boundary conditions for boundary faces are defined. The boundary conditions used in the ship simulation in FINFLO are listed in Table 5.2. Each block face must have a boundary condition and these are defined in the boundary condition file, which shown in Appendix D.

Table 5.2: FINFLO boundary conditions for the ship simulation

Name	Explanation	Where applied	Simulation cases
CON	Connectivity	Internal connections	Both
EXT	External	Outer boundaries of hull volume mesh	Both
MIR	Mirror	Symmetry plane of hull volume mesh	Resistance
ROT	Rotating solid	Propeller surfaces	Self-propulsion
MOV	Moving solid	Ship surface and duct surface	Both
CHI	Chimera	Outer boundaries of propeller and duct blocks	Self-propulsion
FRE	Free surface	Free surface plane	Both

5.3 Simulation schemes and parameters in FINFLO

In this section the simulation schemes used in resistance and self-propulsion simulation by FINFLO are presented and the most important simulation parameters are shown. Both the resistance and self-propulsion RANS simulations are done in model scale and the dynamic position of the ship is calculated with the potential flow solver ν -SHALLO before FINFLO simulations. With the method developed in (Ajanko, 2008) it would be possible to use also the wave pattern from ν -SHALLO in FINFLO simulation, but in this thesis only the dynamic position of the ship calculated by ν -SHALLO is used and the free surface is solved in FINFLO starting from the flat free surface.

5.3.1 Resistance simulation scheme

The ship resistance simulation is done in model scale with FMG by using three grid levels L3, L2 and L1, where level L1 is the finest grid and level L3 is the coarsest grid. The grid on level L1 is the actual grid created while on levels L2 and L3 the mesh is made coarser by joining neighboring shells together. On level L2 each second connector is kept and respectively on level L3 each second connector of the mesh on L2 is kept. The resistance simulations are started on grid level L3 and when the calculation is converged, i.e. residuals do not change significantly, the simulation is continued on grid level L2 and further on level L1.

5.3.2 Self-propulsion simulation scheme

The self-propulsion simulation is done in model scale by the time accurate simulation on grid levels L3 and L2. The simulation is started as a quasi-static simulation with MRF method on grid level L3 and the free surface calculation is included. When the solution is converged, the free surface is frozen and the actual time accurate simulations on grid level L3 and further on level L2 are done. The propeller and duct are implemented to the hull volume grid as separate grid blocks with the Chimera grid method introduced in Section 3.1.4.

The initial guess for the propeller rotation rate is got from the propeller open water curves and the approximation is done based on the nominal wake at the propeller plane and hull resistance obtained in the resistance simulation. The quasi-static simulation on grid level L3 is done with the initial guess for the propeller rotation rate, which is after the quasi-static simulation updated to corresponding to the new ship resistance. Next the time accurate simulation is done on grid level L3 and the propeller rotation rate is updated few times during the simulation, until it does not essentially change anymore. When the self-propulsion point is reached on grid level L3, the simulation is continued on level L2. In Figure 5.9 is shown the idea of the self-propulsion scheme used.

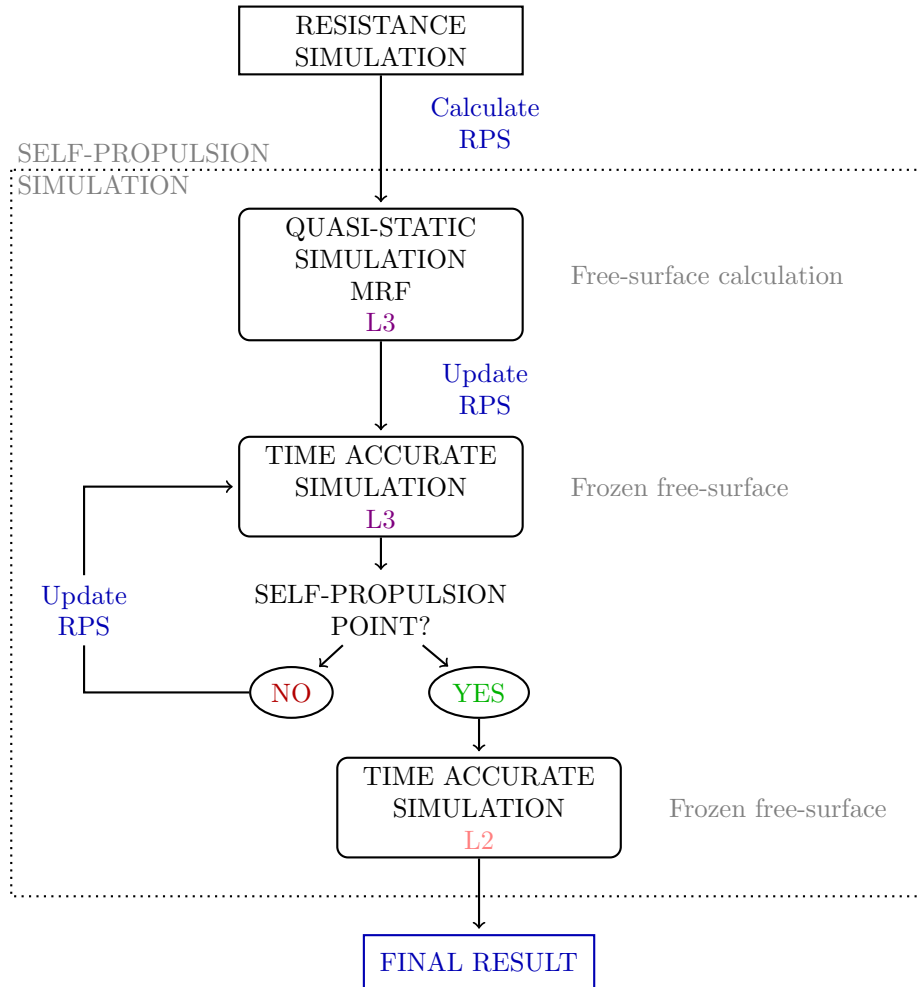


Figure 5.9: Self-propulsion scheme

Since the self-propulsion simulation is done in model scale, the viscous effects in the simulation are over predicted. This is because the scaling from full scale to model scale is done with the Froude scaling law, i.e. the Froude numbers ($Fn = \frac{V}{\sqrt{gL}}$) are kept equal in the model and full scale and thus the Reynolds number in model scale is too small. Hence the propeller has to create relatively more thrust in the model scale than in full scale at the self-propulsion point. To take this difference into account, the model is towed in the model test with a correction force F_D . However, in the self-propulsion simulation no towing force is added to the simulation, but a such propeller rotation rate is searched that the resulting thrust force together with the towing force cancels the ship resistance

$$T + F_D = R_T. \quad (5.37)$$

The towing force corresponds to the difference in friction coefficients between the full and the model scale and according to ITTC-57 method it is calculated as

$$F_D = \frac{1}{2}\rho_m V_m^2 S_m [C_{Fm} - (C_{Fs} + C_A)], \quad (5.38)$$

where C_{Fm} and C_{Fs} are the friction coefficients in model and full scale respectively and C_A is the correlation allowance coefficient. The friction coefficient according ITTC-57 friction line is

$$C_F = \frac{0.075}{(\log(Rn) - 2)^2}. \quad (5.39)$$

The correlation allowance C_A is defined empirically and in this thesis the value defined by HSVA for the original vessel A is used also for the modified vessel B. (Matusiak, 2007a)

5.3.3 Simulation parameters

The simulation is controlled by an input-file in which the simulation parameters are defined. The input files for the resistance and self-propulsion simulations are shown in Appenfix D. The most important free stream values and simulation parameters are shown in Tables 5.3 and 5.4 respectively.

Table 5.3: Free stream values (model scale)

Parameter		Value
V_∞	[m/s]	1.499
T_∞	[°C]	15.0
ρ_∞	[kg/m ³]	1000
ν	[m ² /s]	1.139
Fn	[-]	0.1714
Rn_{LPP}	[-]	$1.0073 \cdot 10^7$

Table 5.4: Simulation parameters used in FINFLO simulations

Parameter	Value
Turbulence model	SST $k - \omega$
CFL	2.0
CFL_{FRE}	2.0
INTERK	-3 -3 1 / -3 -3 -3
α_u (ALFAUB)	0.5
α_p (ALFAP)	0.02

In Table 5.4 CFL is the flow Courant number, which is defined as

$$CFL = \frac{u\Delta t}{\Delta x}, \quad (5.40)$$

and CFL_{FRE} is the Courant number for the free surface calculation. INTERK defines the discretization parameters used in the I , J and K directions given respectively in the table, where the left hand side values are used in the resistance simulation and the right hand side values in the self-propulsion simulation. Value -3 is the third-order upwind scheme without flux limitation and value 1 is the second-order upwind biased scheme with the van Albada limiter. Parameters α_u and α_p are the under-relaxation factors for the velocity and pressure correction respectively.

The FINFLO simulations are run on a server with 48 Intel Xeon X5560 processors (2.80 GHz) and 108 GB of main memory. The resistance simulations were done by using 19 cores while 22 cores were used for the self-propulsion simulation. In the resistance simulation on the finest grid level L1 the computation time of one iteration was approximately 8.2 sec./iteration and 20 000 iterations were done. In the time-accurate self-propulsion simulation one propeller revolution was divided to 250 time steps. On the medium grid level L2 the computation time of one time step was approximately 20 minutes.

In this chapter the ship flow simulation equations, potential flow model and RANS equation together with the boundary conditions for the ship and free surfaces have been presented. The simulation tools v-SHALLO and FINFLO have been introduced and the computational grids to be used have been described. The simulation schemes for the resistance and self-propulsion simulation in FINFLO have been presented and the most important simulation parameters have been shown. In the next chapter the simulation results are presented and discussed.

Chapter 6

Results and discussion

The resistance and self-propulsion simulations were done with the large vessel and ducted propeller by FINFLO in model scale. Before the self-propulsion simulation was run, the propeller open water simulations were done for the ducted propeller. For a comparison, the propeller open water simulations were done also for the open propeller used in the original vessel A.

In the resistance simulation the hull resistance and the nominal wake field were studied and compared to corresponding results of the original vessel. There are no model test results for the modified hull B. The propeller open water simulations were done in order to obtain knowledge of how accurately FINFLO can simulate the propeller flow. The obtained K_T , K_{TN} , K_Q , η_0 and τ were considered and compared to the propeller open water model test results. In the self-propulsion simulation the results were obtained for the propeller rotation rate n , thrust T and torque Q . Additionally the thrust and torque coefficients K_T and K_Q , the effective wake fraction w_T , the thrust deduction factor t , the effective power P_E and the power delivered at propeller P_D , the hull efficiency η_H , the propulsive efficiency η_D , the relative rotative efficiency η_R and the open water efficiency η_0 were computed and compared to corresponding values of the original vessel. The thrust deduction factor is in model scale calculated from

$$t = 1 - \frac{R_{Tm} - F_D}{T_{tot,m}} \quad (6.1)$$

and the wake fraction is

$$w = 1 - \frac{V_A}{V}. \quad (6.2)$$

The nominal wake field is obtained from the resistance simulation and in this thesis the averaged nominal wake field in the axial direction at the propeller disk is marked with w_n and called the nominal wake fraction. The effective wake fraction w_T is computed from the self-propulsion test results by using the thrust identity. In both cases the average advance velocity of the propeller V_A can be calculated from Equation (6.2). The effective power is calculated from

$$P_E = R_T V \quad (6.3)$$

and the power delivered at propeller is obtained from

$$P_D = 2\pi Q n. \quad (6.4)$$

The hull efficiency is defined as

$$\eta_H = \frac{1 - t}{1 - w}, \quad (6.5)$$

the propulsive efficiency is obtained from

$$\eta_D = \frac{P_E}{P_D} \quad (6.6)$$

and the relative rotative efficiency from

$$\eta_R = \frac{K_{QT}}{K_Q}, \quad (6.7)$$

where K_{QT} is the torque coefficient which corresponds to the computed thrust. All the results are given and compared in the model scale as the simulations were done in the model scale. In order to obtain a full scale prediction from the model scale results, an extrapolation method, for example ITTC-57 or ITTC-78, should be used. However, since only the percentage differences have been considered and the ship scales and velocities of the vessels A and B are equal, the scaling has no effect on the presented results. In the next sections the results for the resistance, propeller open water and self-propulsion simulations are shown and discussed.

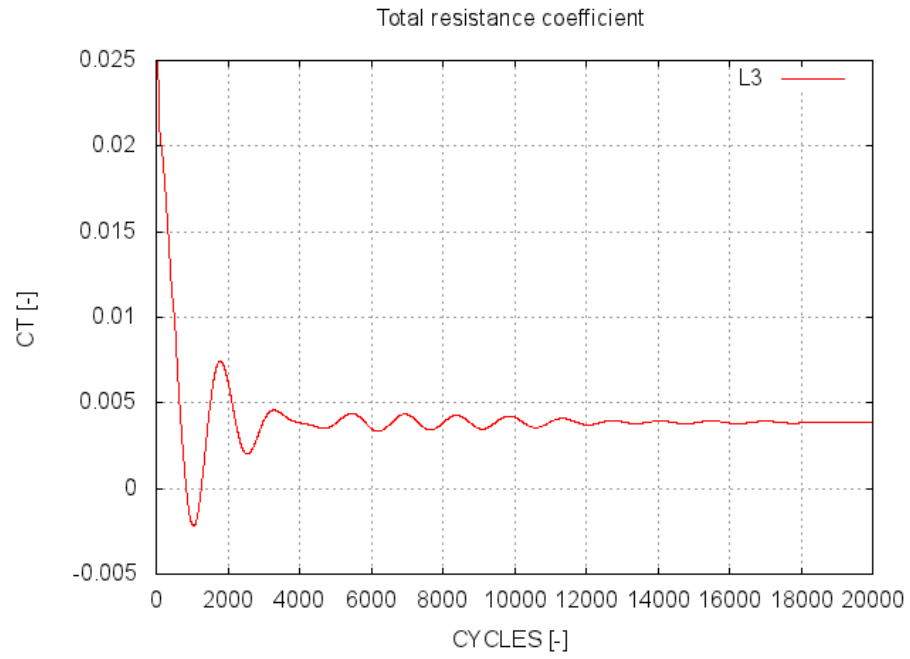
6.1 Resistance simulation

The dynamic position of the ship was calculated before FINFLO simulations by ν -SHALLO. In Table 6.1 the trim angle and dynamic sinkage are shown as a percentage of the values of the original hull. It can be seen, that the sinkage of the vessel B has increased from the sinkage of the vessel A and the trim angle is smaller.

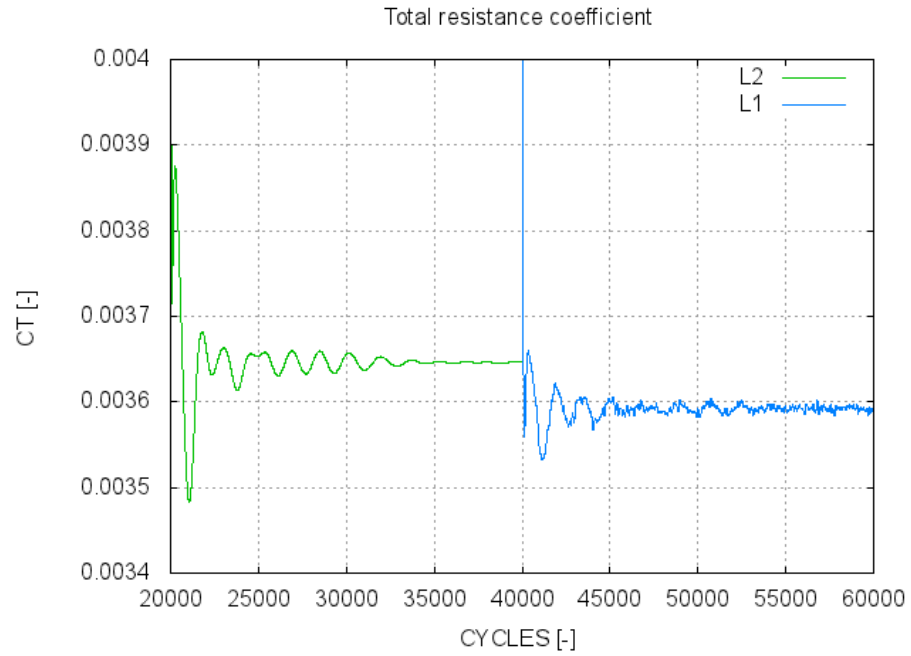
Table 6.1: Dynamic position of the ship calculated with ν -SHALLO as a percentage of the dynamic position of the vessel A.

		Vessel B	Vessel A
Trim angle	[%]	96.7	100.0
Sinkage	[%]	101.0	100.0

The resistance simulation by FINFLO was done on three grid levels L3, L2 and L1. In Figures 6.1, 6.2 and 6.3 the convergence curves of the total resistance coefficient, turbulent kinetic energy and minimum and maximum wave heights are shown. It can be seen, that the simulation has converged, even though there are small fluctuations on values on the finest grid level.

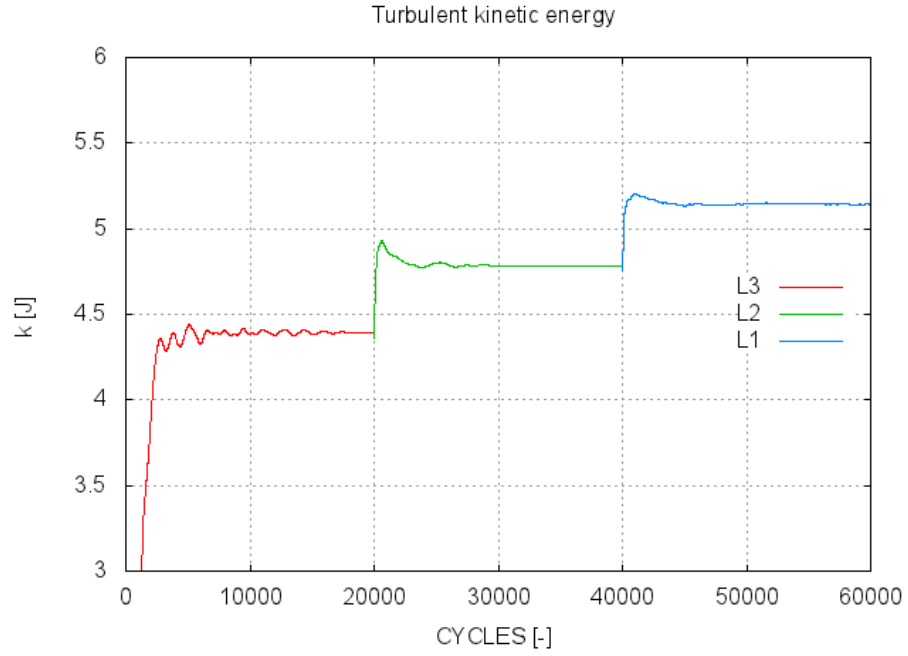


(a) Convergence of the total resistance coefficient on the coarsest grid level (L3)

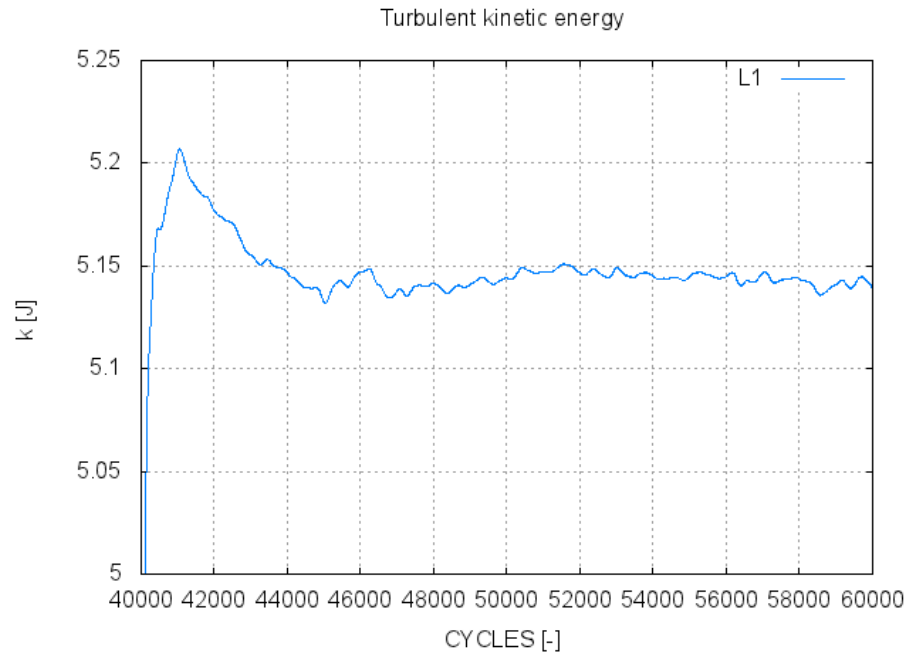


(b) Convergence of the total resistance coefficient on the medium (L2) and fine (L1) grids

Figure 6.1: Convergence of the total resistance coefficient of the vessel B



(a) Convergence of the turbulent kinetic energy



(b) Convergence of the turbulent kinetic energy on the finest grid level (L1)

Figure 6.2: Convergence of the turbulent kinetic energy of the vessel B

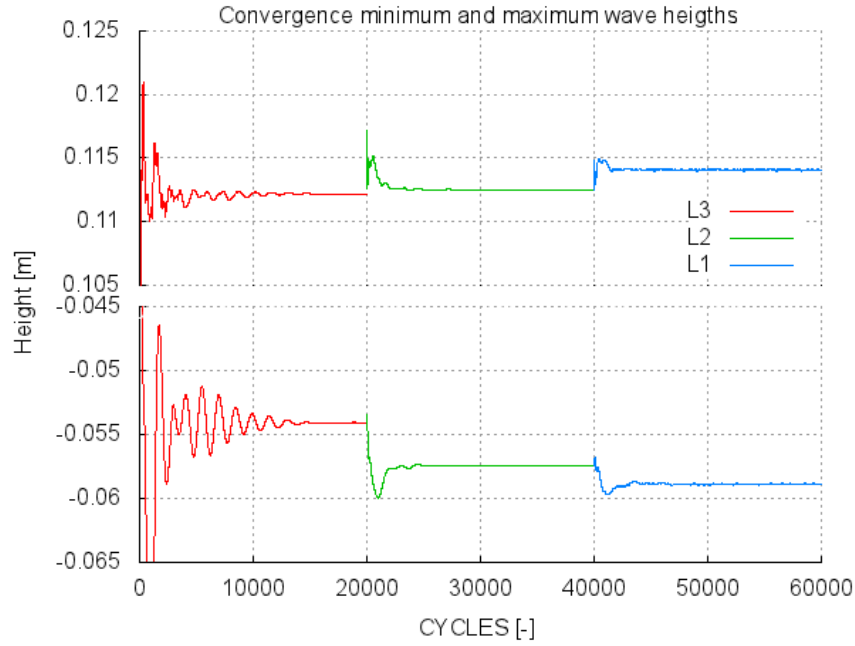


Figure 6.3: Convergence of the minimum and maximum wave heights of the vessel B

The wave patterns of the both vessels A and B are shown in Figure 6.4 and the wave patterns at the aft region are shown closer in Figure 6.5. In Figures 6.6 and 6.7 the wake fields of the both vessels are shown at the propeller plane and at the propeller disk, respectively.

In Figure 6.4 it can be seen that the wave pattern has changed not only at the aft region but also at the bow and midship areas. The bow wave has become a bit deeper and the waves at the midship region are lower. Also the aft waves of the modified vessel are a bit lower than in the original vessel. In Figures 6.6 and 6.7 it can be seen that the flow is slower at the wake field with the modified hull, i.e. the nominal wake fraction is increased. It must be though noticed, that the location of the propeller disk is more astern in the vessel B.

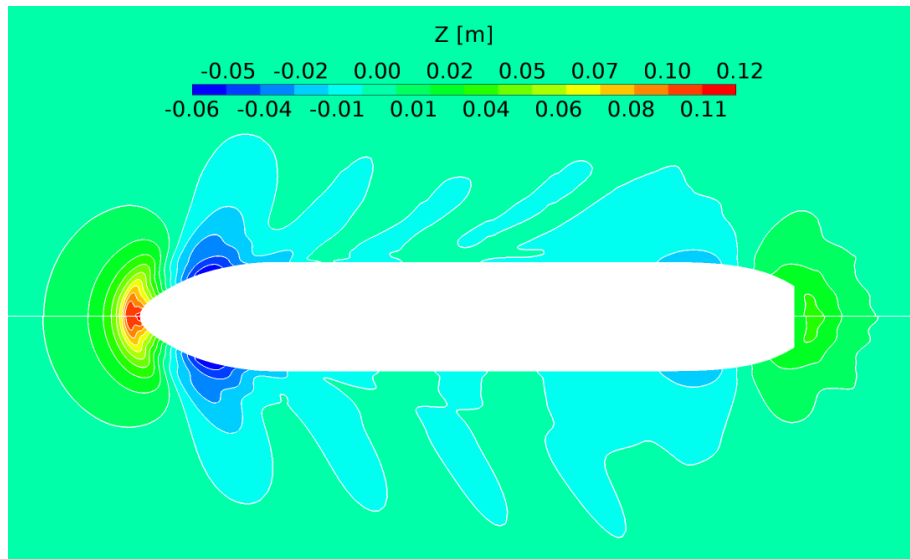


Figure 6.4: Wave patterns of modified (above) and original (below) hull forms

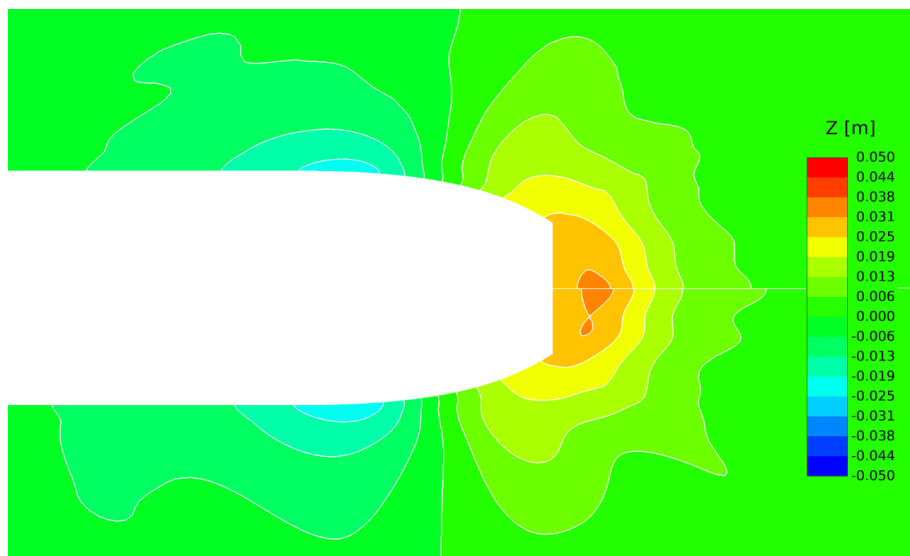


Figure 6.5: Wave pattern at the aft region of modified (above) and original (below) hull forms

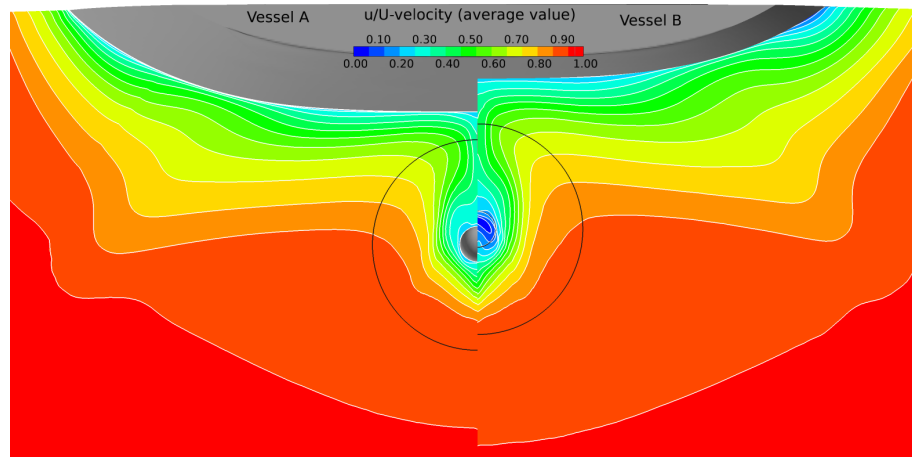


Figure 6.6: Nominal wake at the propeller plane of the original vessel (left) and modified vessel (right)

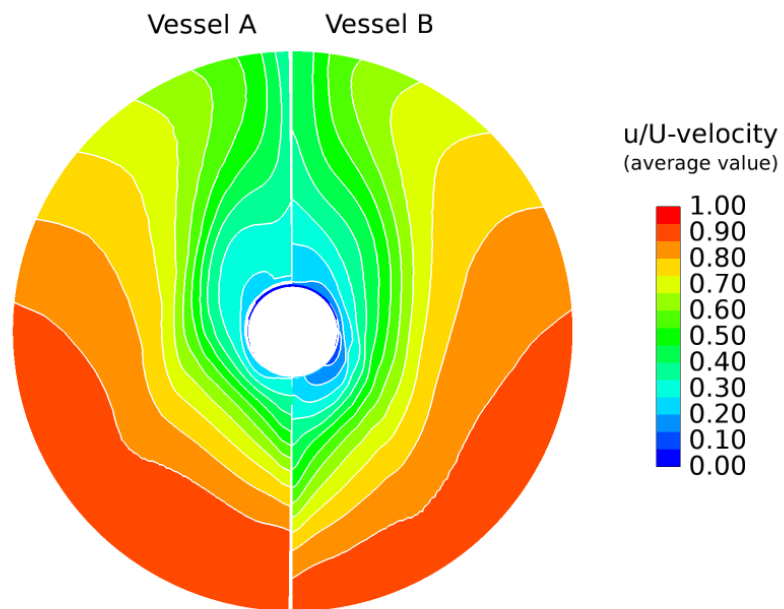


Figure 6.7: Nominal wake at the propeller disk of original (left) and modified (right) hull forms

The changes in the hull resistance and averaged nominal wake w_n are given in Table 6.2 as a percentage of the models test results of the original vessel A. Additionally, the changes in viscous and residual resistances, R_V and R_T respectively, are given as percentages of the simulation results of the original vessel. Both simulations have been done without appendages. However, in the model tests the nominal wake field is measured from the model having the pre-swirl stators and in the resistance test both the rudder and pre-swirl stators are included. Thus, in the comparison of the simulation results and the model test data it must be taken into account, that the appendages create additional resistance and the pre-swirl stators slow the flow and thus increase the nominal wake fraction.

Table 6.2: Resistance test results as percentage values (model scale)

		Vessel B		Vessel A
		FINFLO	FINFLO	HSVA
R_T	[%]	95.9	96.4	100.0
R_R	[%]	99.2	100.0	-
R_V	[%]	99.6	100.0	-
w_n	[%]	85.0	82.8	100.0

From the results it can be seen that even though the hull form modifications made were small, they had a little effect on the ship resistance and wake field. The comparison of the FINFLO simulation results of the vessels A and B shows, that the resistance of the new hull form is 0.5 % smaller than the resistance of the original hull. When the viscous and residual resistance components are compared, it is noticed that the viscous resistance has decreased less than 0.5 % and the residual resistance has decreased almost by 1.0 %. In addition, the consideration of the composition of the total resistance reveals that with the modified hull form the share of the viscous resistance has increased and the share of the residual resistance decreased when compared to the total resistance composition of the original hull. In Figures 6.4 and 6.5 it can be seen that the changed position of the ship, which results from the modification made on the skeg, gives lower waves both at the midship section and at the aft region. The bow wave is a bit deeper in the modified vessel, but the changes in the mid-ship and stern regions are more remarkable, as can be seen from the decreased residual resistance. The nominal wake fraction w_n was increased by 2.7 % with the new hull form, which means that the averaged flow velocity in the x -direction is decreased, as can be seen in Figure 6.7.

When the resistance simulation results of the original hull shape are compared to the model test results, it can be noticed that FINFLO underestimates both the resistance value and the averaged nominal wake value so that the total resistance is underestimated by 3.6 % and the nominal wake fraction by 17.2 %. In the resistance simulation no appendages are included while in the model tests the rudder and pre-swirl stators are used. These appendages create additional resistance and for example the rudder was estimated to create 3 % of the total resistance in Chapter 4. Thus the accuracy of the FINFLO resistance prediction can be regarded good while a relative large difference is though obtained in the nominal wake prediction. Probable reasons for the inaccuracy of the wake field prediction are the turbulence

modeling, which is challenging at the ship stern region because of the complex hull shape and flow vorticity, and the insufficient grid resolution at the wake field.

6.2 Propeller open water simulation

The propeller open water simulations were done both for the propeller Ka4-55 in duct 19A, which was the propeller chosen to the vessel B, and for the open propeller of the vessel A. The propulsion points in both cases were calculated on the medium grid level L2 with nine advance numbers, which were controlled with the inflow velocity while the propeller rotation rate was kept constant. Additionally, the effect of the grid resolution was studied with the ducted propeller by recalculating two points on the finest grid level L1.

6.2.1 Ducted propeller Ka4-55 in 19A

In Figure 6.8 the calculated points for both grid levels L2 and L1 and the propeller open water curves obtained from the propeller model tests are shown. In Table 6.3 the values computed on the grid level L2 are shown as a percentage of the model test results and in Table 6.4 the results on the grid level L1 are shown. From the results it can be seen, that on the grid level L2 the largest difference in the total thrust is 8.7 %. The thrust created by the duct is greatly underestimated and the maximum difference of 50.5 % is obtained at $J = 0.1$, when the advance numbers having a positive duct thrust are considered. The difference decreases when the advance number increases, the minimum difference being 11.9 %. As the duct thrust is underestimated and the total thrust approximately right, the propeller thrust is overestimated, which can also be from the too high duct loading factor τ . The error in τ increases when the propeller advance number decreases and similar behavior can be seen in the propeller torque calculation. The torque is overestimated, the difference being largest (40 %) with small advance numbers and getting smaller when the advance number is increased.

The simulation on the finest grid level L1 gives more accurate results. At the advance number $J = 0.7$, which is close to the design point of the propeller of the vessel B, the differences in the propeller thrust and torque are less than 1 %. However, the duct thrust is still underestimated by the same amount as on the grid level L2 and thus also the total thrust is underestimated. With the smaller advance number $J = 0.5$ the differences are a bit larger, but still the simulation accuracy of the propeller thrust and torque has improved remarkably from the medium grid simulation. Also at $J = 0.5$ the duct thrust is almost equal to the thrust obtained on the medium grid level.

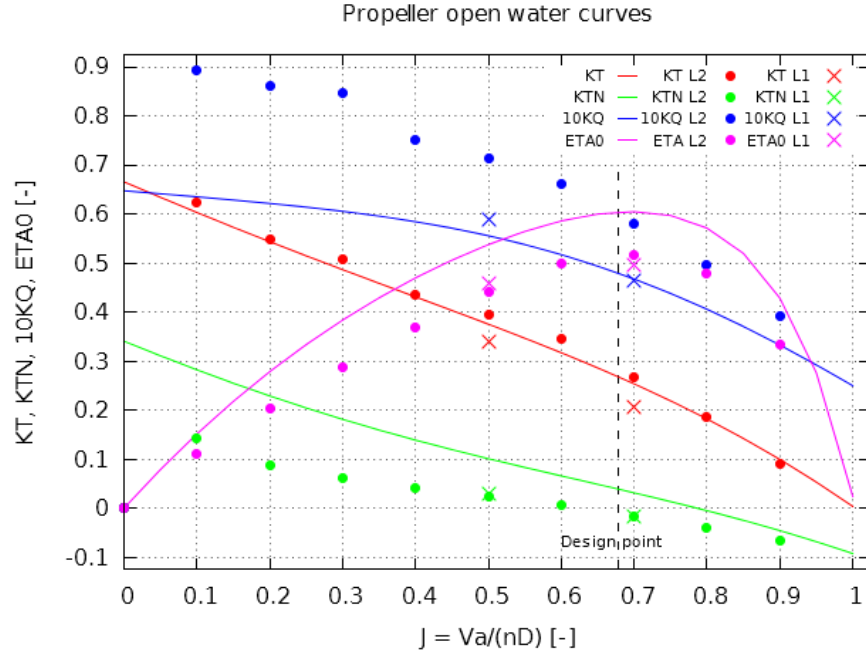


Figure 6.8: Propeller open water curves and simulation results for Ka4-55 in duct 19A with $P/D = 1.2$. The simulation results on grid level L2 are marked with dots and the results on grid level L1 with crosses. The design point of the propeller is marked with the dashed line.

Table 6.3: The propeller open water simulation results on grid level L2 as a percentage of the model test results (Oosterveld, 1970) of the propeller Ka4-55 in duct 19A

J [-]	K_T [%]	K_{TN} [%]	K_Q [%]	η_0 [%]	τ [%]
0.1	103.3	50.5	140.7	73.4	145.0
0.2	100.7	38.7	138.6	72.6	144.9
0.3	104.2	33.3	139.6	74.7	140.5
0.4	101.2	29.1	128.7	78.6	133.9
0.5	105.5	24.9	128.6	82.0	128.1
0.6	108.7	11.9	127.8	85.1	123.4
0.7	105.7	-51.8	124.0	85.2	121.1
0.8	102.4	805.3	122.4	83.6	118.1
0.9	91.5	143.9	117.6	77.8	118.0

Table 6.4: The propeller open water simulation results on L1 as a percentage of the model test results (Oosterveld, 1970) of the propeller Ka4-55 in duct 19A

J	K_T	K_{TN}	K_Q	η_0	τ
[-]	[%]	[%]	[%]	[%]	[%]
0.5	90.3	28.4	106.2	85.1	125.3
0.7	81.5	-48.3	99.2	82.2	122.5

The comparison of the results on the medium and fine grids (L2 and L1) show that the accuracy of the propeller performance prediction increases remarkably when the fine grid is used. Reason for this is the Chimera interpolation, which works better with the finer grid. The Chimera interpolation on the boundary of the over-lapping grid is not in a so-called conservation form. Consequently, the continuity equation can be locally untrue, which means that the mass is either created or disappeared (the mesh is leaking). With coarse grids more leakage occurs, while with fine grids the continuity equation is better satisfied.

A fundamentally same duct thrust value is obtained with the both grid levels L2 and L1, and thus the reason for this inaccuracy is probably not the grid resolution. As described in Chapter 2, the duct thrust is affected by the inflow velocity and the inflow angle and thus the possible reasons for the duct thrust underestimation are a too small inflow angle, a too high inflow velocity, an overestimated viscous resistance or a combination of these. Additionally the free vortices and viscous resistance affect the duct thrust.

The inflow angle and velocity are bounded to the propeller performance while the viscous resistance calculation has more to do with the simulation of the boundary layer. Since the propeller performance changed when changing the grid level but the duct thrust remained the same, the propeller behavior is not the reason for the error in the duct thrust calculation. Hence either the boundary layer calculation has a large effect or the nozzle geometry used in the simulation is not correct. In the simulation the duct boundary layer is modeled as a turbulent boundary layer while it based on the Reynolds number along the duct chord is laminar. As the flow behavior is different in laminar and turbulent flows, applying the turbulence model in a laminar boundary layer can give unrealistic results. However, the same situation is in the propeller simulation, but still quite accurate results for the propeller forces are obtained. Thus the most probable reason for the difference in the duct thrust prediction is the nozzle profile shape, where the roundings of the leading and trailing edges are not exactly the same as in the nozzle used in the model test. The edge shapes affect the flow field around the nozzle and as a consequence the forces are affected. For example, a blunter trailing edge creates larger free vortices and thus the induced drag is increased and the total force in the x -direction decreased.

6.2.2 Open propeller

In Figure 6.9 the calculated points and the propeller open water curves of the propeller of the vessel A are shown. In Table 6.5 the values computed on the grid level L2 as a percentage of the model test values are given. From the results it can be seen, that the thrust is overestimated when the advance coefficient is $J < 0.8$,

the difference being largest (42.7 %) at the smallest advance coefficients. For the higher advance coefficients the propeller thrust is a bit underestimated. The torque values are similarly overestimated, the difference being largest (47.6 %) at the small advance coefficients.

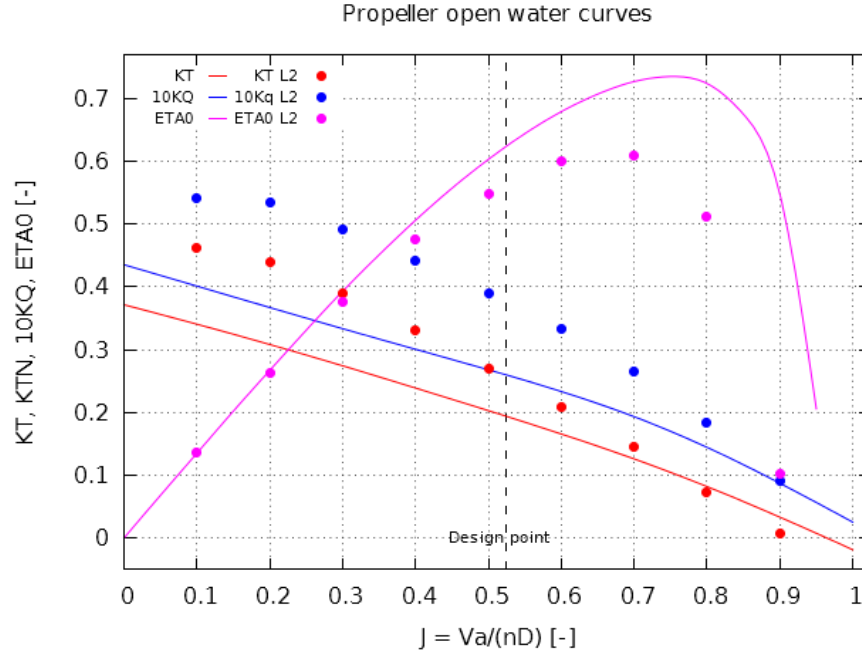


Figure 6.9: Propeller open water curves and simulation results for the open propeller used in the vessel A. The simulation results (grid level L2) are marked with dots and the design point is marked with a dashed line.

Table 6.5: Propeller open water simulation results as a percentage of the model test results of the open propeller of vessel A

J	K_T	K_Q	η_0
[-]	[%]	[%]	[%]
0.1	135.4	134.7	100.5
0.2	142.7	145.4	98.1
0.3	141.7	147.6	96.0
0.4	138.2	147.0	94.0
0.5	132.5	145.7	90.9
0.6	126.4	142.9	88.5
0.7	114.7	136.9	83.8
0.8	89.8	127.1	70.7
0.9	19.4	104.2	18.6

The open water simulation of the open propeller on grid level L2 gives the same kind of results as the ducted propeller simulation on L2, i.e. because of the coarse grid the Chimera interpolation does not work well and thus the propeller thrust

and torque are overestimated. It is supposed that the accuracy of the simulation increases also in this case when the simulation is done with the denser grid.

6.3 Self-propulsion simulation

The self-propulsion simulation was done on two grid levels L3 and L2. In Figures 6.10, 6.11 and 6.12 the convergence curves of the total resistance coefficient, turbulent kinetic energy and minimum and maximum wave heights are shown, respectively. In Figures 6.13, 6.14, 6.15 and 6.16 the convergences of the total thrust of ducted propeller, propeller thrust, duct thrust and propeller moment are shown, respectively. It can be seen, that the rotating propeller causes oscillation to the total resistance. In the convergence curves of the propeller and duct forces, the updates in the propeller rotation rate can be seen as jumps in the force level. On the grid level L2 the force calculation has reached a sufficient convergence during the ninth propeller revolution (the third propeller revolution on the level L2) whereas the turbulent kinetic energy has not yet converged.



Figure 6.10: Convergence of the total resistance coefficient in quasi-static (QS) and time-accurate (TA) simulations on the coarse and medium grids (L3 and L2)

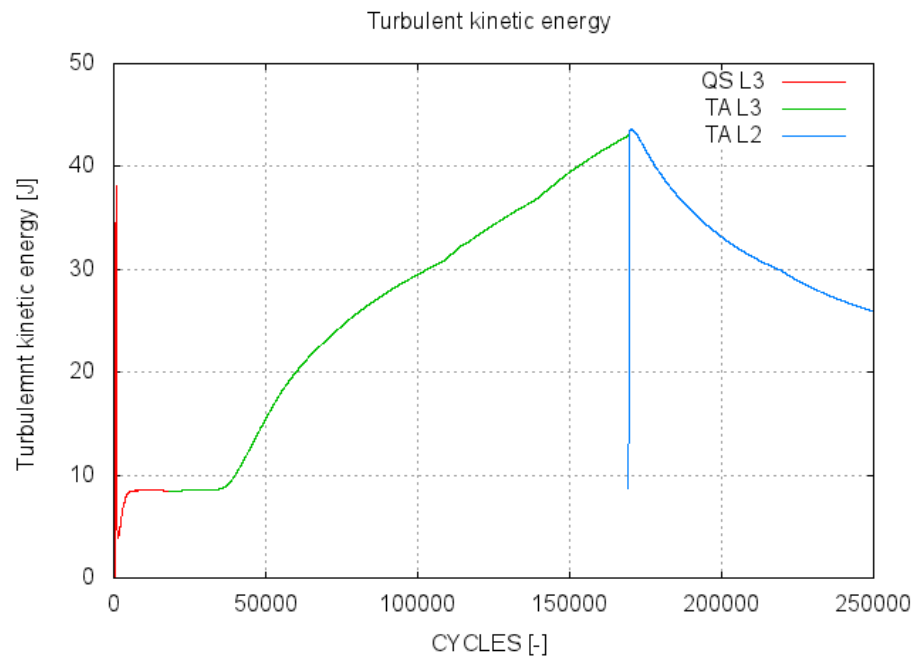


Figure 6.11: Convergence of the turbulent kinetic energy

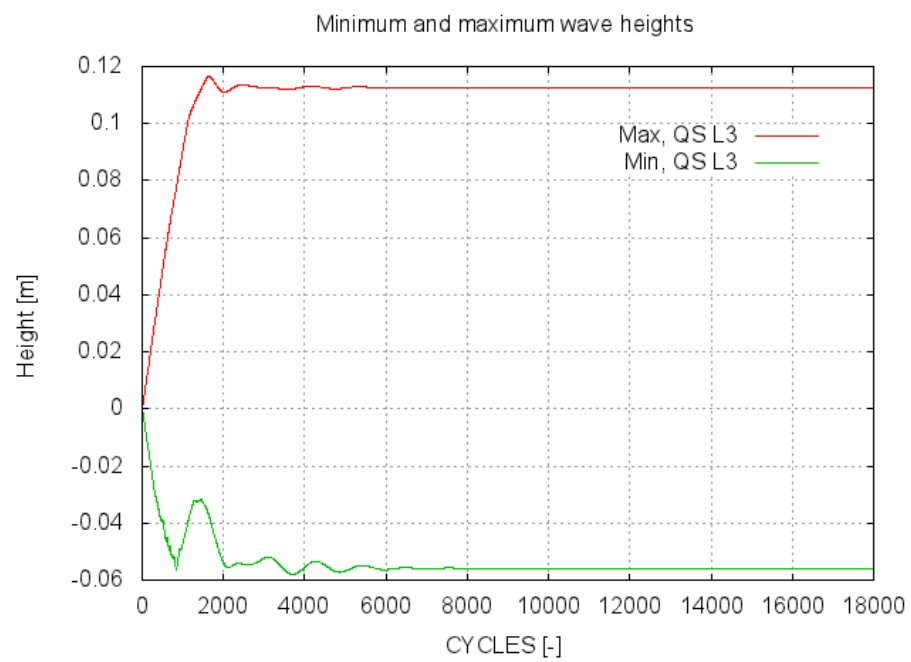


Figure 6.12: Convergence of the minimum and maximum wave heights



Figure 6.13: Convergence of the total thrust of the propeller and the duct

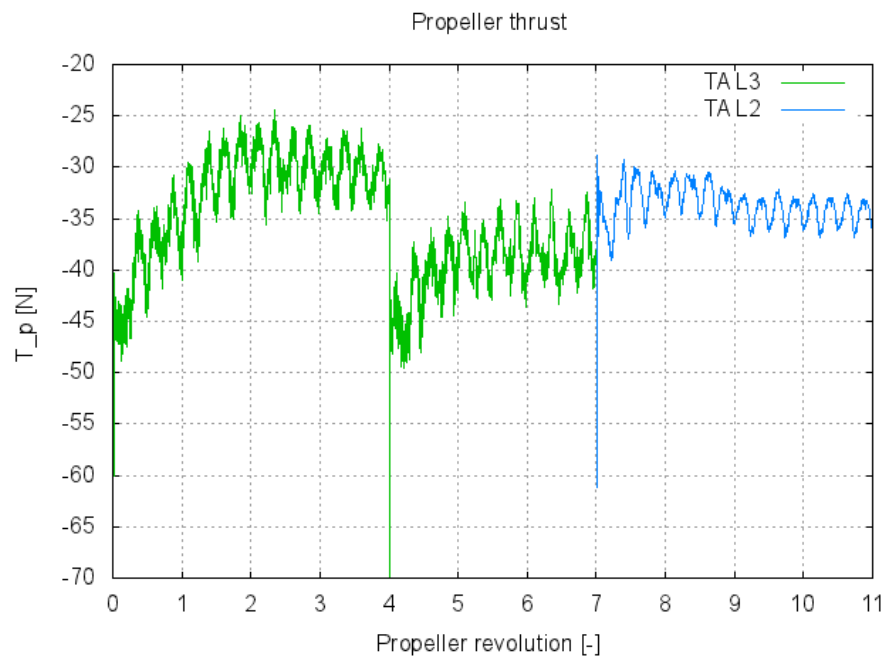


Figure 6.14: Convergence of the propeller thrust

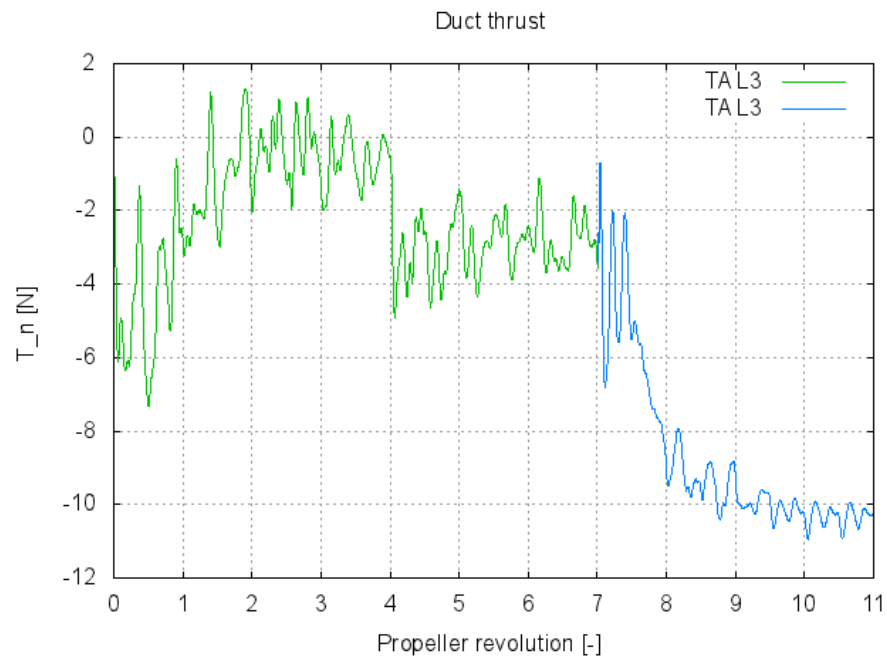


Figure 6.15: Convergence of the duct thrust

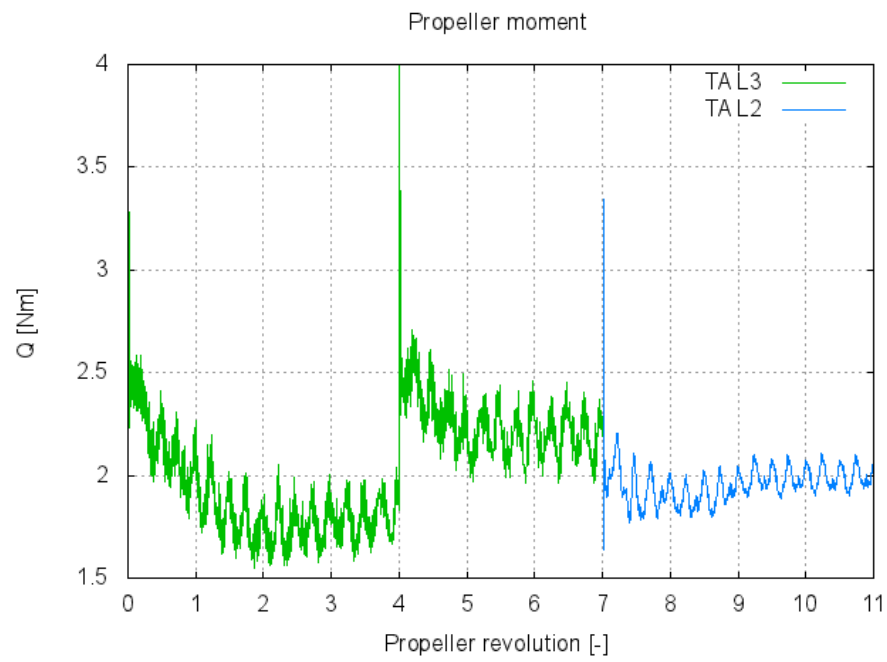


Figure 6.16: Convergence of the propeller moment

The wave pattern obtained on the grid level L3 and further used in the time-accurate simulations is shown in Figure 6.17. When the wave pattern in Figure 6.17 is compared to the wave formation obtained in the resistance simulation, shown in Figure 6.4, it can be seen that the wave form used in the self-propulsion simulation is not fully developed. Additionally the effect of the propeller can be seen in the aft wave, where the wave pattern is not symmetric.

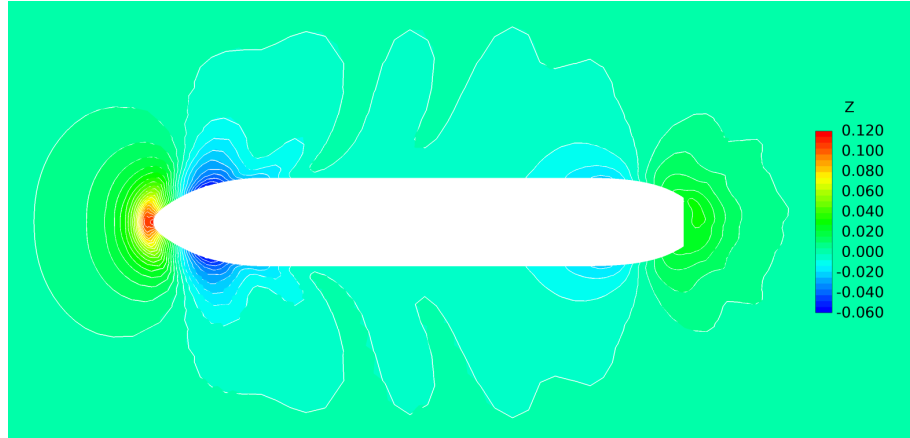
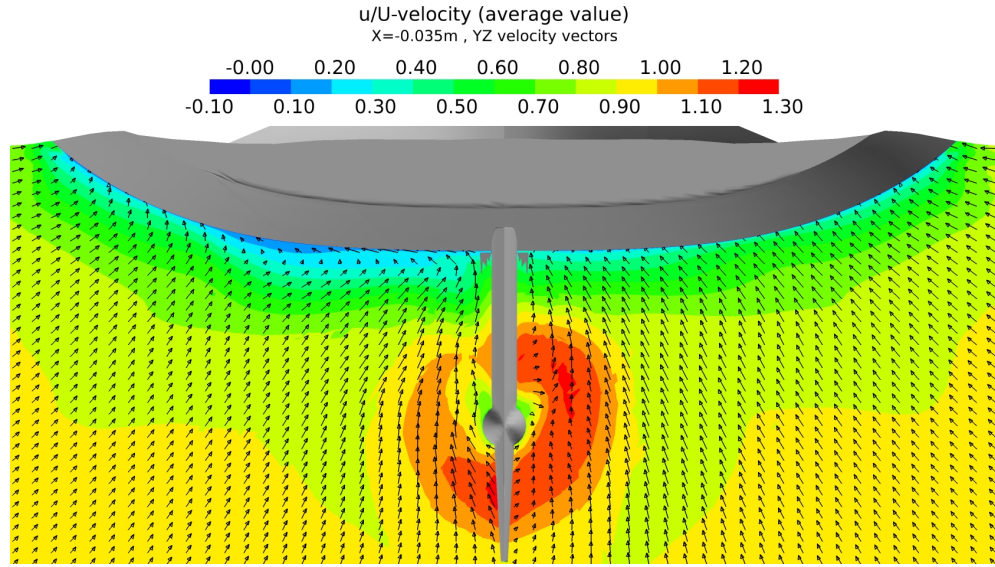
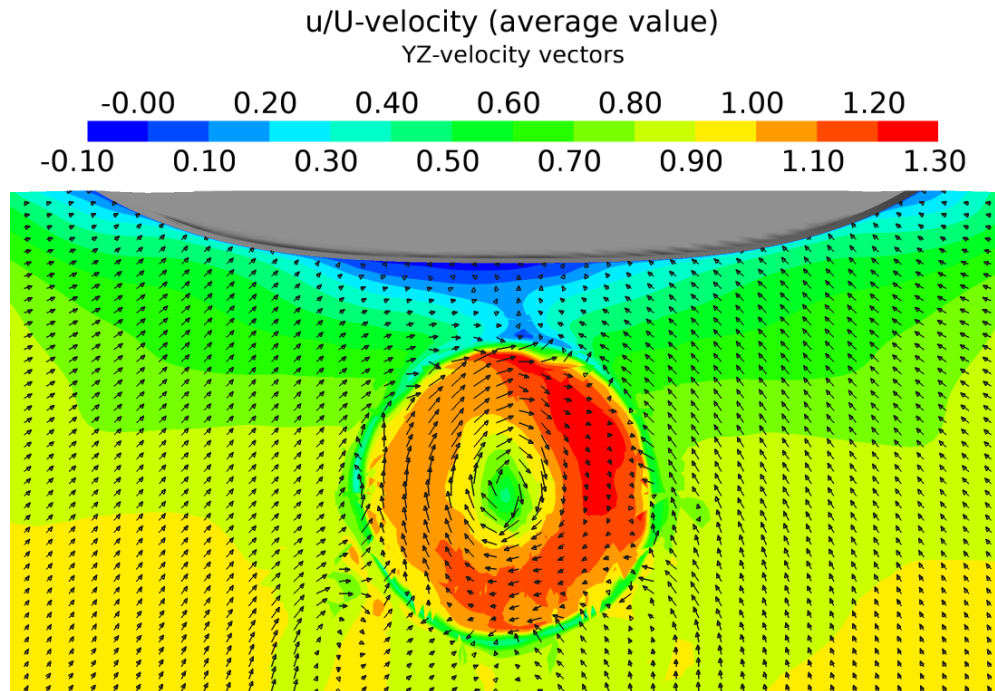


Figure 6.17: Wave pattern of the self-propulsion simulation obtained on grid level L3

The wake fields of the original vessel A and modified vessel B at the locations $D/3$ aft-wards from the propeller planes are shown in Figure 6.18. The effect of the duct can be seen in Figure 6.18(b) as a ring shaped region with a lower flow speed and varying yz -velocity directions. When the velocity distribution is compared to the wake of the original vessel in Figure 6.18(a), it can be seen the flow inside the duct is more uniformly accelerated than the flow with the open propeller.



(a) Original vessel A



(b) Modified vessel B

Figure 6.18: Wake field at $D/3$ after the propeller plane

The thrust and moment of each propeller blade during one propeller revolution are shown in Figures 6.19 and 6.20. The thrust force of a blade is the total force of the blade in x -direction and the torque of a blade is defined around the propeller axis.

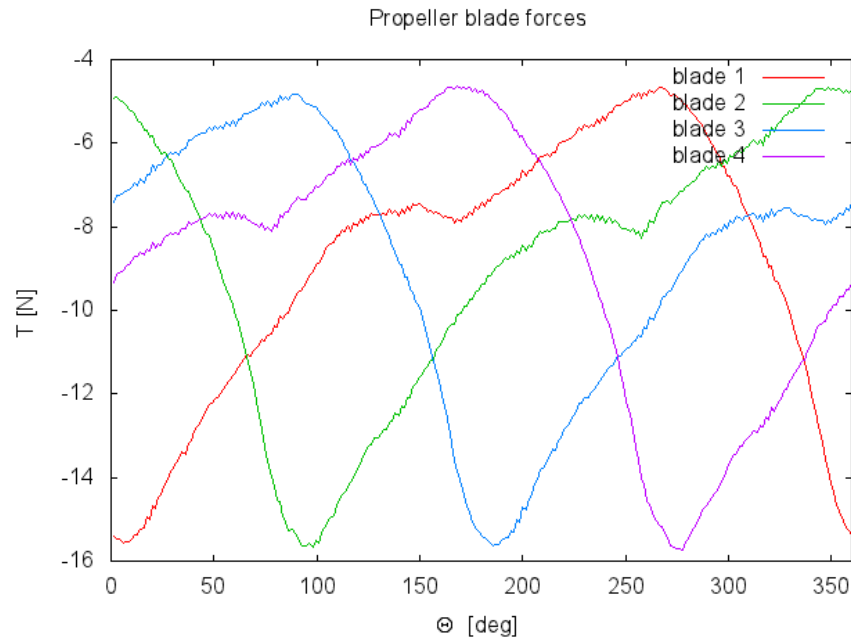


Figure 6.19: Thrust forces of the propeller blades during one propeller revolution

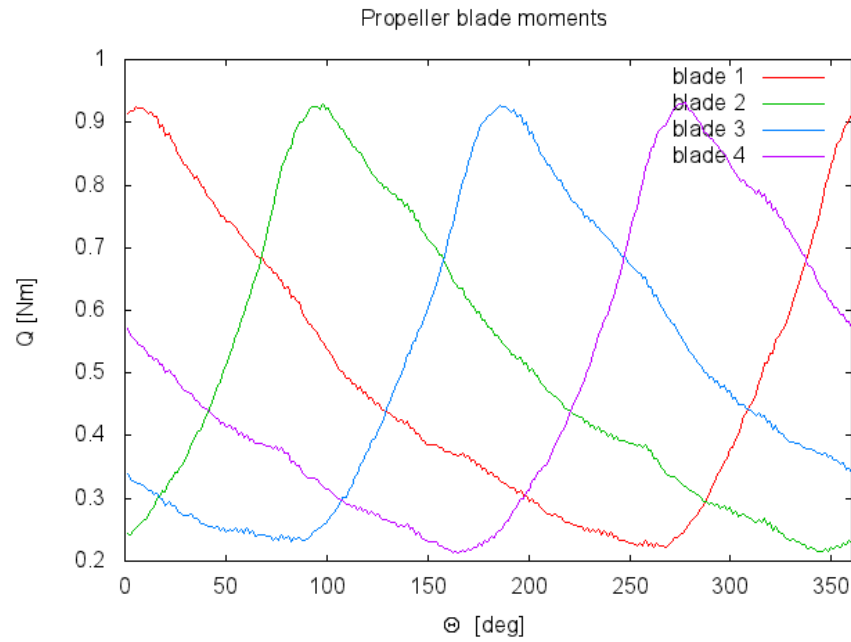


Figure 6.20: Moments around the propeller axis of the propeller blades during one propeller revolution

In Table 6.6 the self-propulsion test results for the simulation of the vessels A and B and for the model test of the vessel A are given. The results are presented as percentage of the model test values of the original vessel A. As the thrust, moment and resistance values oscillate within one propeller revolution, the final values are obtained as average values of the last propeller revolution. The total resistance shown in Table 6.6 is the resistance with the rotating propeller, which in the full

scale self-propulsion point is equal to the thrust and in model scale equal to the difference of the obtained resistance and towing force. The wake fraction w_T is the effective wake fraction obtained from the propeller open water curves based on the propeller thrust and rotation rate. In the simulation of the vessel B there is the nozzle and propeller included and in the simulation and model test of the vessel A, the propeller, rudder and pre-swirl stators are included.

From the results it can be seen that with the vessel B the self-propulsion point is reached, the total thrust being only 0.3 % smaller than the resistance. The self-propulsion simulation of the vessel A is done with a fixed propeller rotation rate defined in the model test and the self-propulsion point is not reached, the thrust being only 86.5 % of the thrust achieved in the model test measurement. However, the general guidelines of the simulation of the vessel A reveal, that the torque is overestimated with relation to thrust and the effective wake fraction is underestimated.

Since the self-propulsion point is not reached in the simulation of the vessel A, the results of the vessel B are compared to model test data of the vessel A. In the comparison it can be seen that the required thrust has increased by 6.0 %. However, with the ducted propeller the amount of the thrust created by the propeller is only 81.5 % of the propeller thrust of the original vessel. The duct loading factor is obtained to be $\tau = 0.77$, which is 10.2 % smaller than what was expected based on the propeller open water curves. The propeller rotation rate has decreased by 12.4 % from the original vessel but the required torque is 35.2 % larger. The increased propeller torque results with 18.8 % increase in the power delivered at propeller and 23.2 % decrease in the propulsive efficiency η_D . Additionally the hull efficiency has decreased remarkably by 25.7 %, when the wake fraction has decreased and thrust deduction factor increased.

Based on the resistance simulation, the wake fraction was expected to be under predicted. Since the wake fraction is underestimated, the inflow velocity to the propeller is higher than in reality and hence the propeller rotation rate is supposed to be over predicted, as can be seen from the simulation of the vessel A. Similarly the propeller torque value is supposed to be over predicted based on the results of the ducted propeller open water simulations and self-propulsion simulation of the vessel A and thus also the power delivered at propeller is overestimated. The amount of the over prediction can be approximated from the open water simulation results. Since the self-propulsion simulation is done on the grid level L2, the difference between the real and calculated torque values is estimated based on the propeller open water simulation on the level L2. The difference is at the design point obtained with the linear interpolation to be 27.8 %. When the new torque value is calculated with this difference, the power delivered at the propeller is only 85.4 % of the power delivered at propeller of the vessel A. However, the background grid is in the self-propulsion simulation a bit denser than in the open water simulation and thus the difference might be smaller. Since the actual needed correction is not known because of the different grids, an estimation is done also for the minimum correction needed in order to obtain at least equal P_D in both vessels A and B. The study reveals, that the equal P_D is obtained when the propeller torque is in the simulation overestimated by 15.4 % and with the overestimation of 11.2 % the P_D of the vessel B is 5 % larger than the P_D of the vessel A.

Table 6.6: Self-propulsion results as a percentage of the self-propulsion model test data of the vessel A(model scale)

		Vessel B		Vessel A
		FINFLO	HSVA	FINFLO
R_T	[%]	105.7	100.0	109.9
n	[%]	87.6	100.0	100.0
T_{tot}	[%]	106.0	100.0	86.5
T_p	[%]	81.5	100.0	86.5
Q	[%]	135.2	100.0	92.5
K_T	[%]	138.2	100.0	86.5
K_Q	[%]	176.3	100.0	92.5
w_T	[%]	76.9	100.0	76.9
t	[%]	167.7	100.0	73.1
P_E	[%]	90.7	100.0	93.2
P_D	[%]	118.2	100.0	92.4
η_0	[%]	101.8	100.0	106.3
η_R	[%]	102.6	100.0	98.3
η_H	[%]	74.3	100.0	93.4
η_D	[%]	76.8	100.0	100.9

In the new estimation of the power delivered at the propeller, the possible corrections needed for the thrust forces are not considered. Based on the propeller open water simulations, the propeller thrust would be over predicted and the duct thrust underestimated. However, in the self-propulsion simulation the duct loading factor is smaller (the duct creates larger amount of the total thrust) than what was expected based on the open water curves from the model tests and hence the propeller open water simulation results cannot be used as a guideline for the thrust corrections. If the thrust is assumed to be approximately correct, the duct works very well behind the vessel B and decreases the propeller loading remarkably. In the case where the corrections would be needed, the obtained propulsion point is not the self-propulsion point.

In addition to uncertainties in the propeller simulation, the self-propulsion simulation results are affected also by the simplifications made in the simulation problem statement. In the self-propulsion simulation the ship position is kept the same as in the resistance simulation even though in reality the working propeller may change the trim angle and sinkage of the ship. The free-surface shape is calculated on the coarsest grid level L3 and then kept static during the time accurate simulations and thus the free-surface shape used is not quite accurate at the beginning and further it does not adopt the changes which the rotating propeller would cause. This means that the kinematic boundary condition of the free surface is not satisfied and the flow below the free surface is not exactly right. Additionally, the final self-propulsion simulation results are calculated on the grid level L2 which is too coarse for obtaining accurate results. Especially the Chimera grid interpolation suffers from the too

coarse grid. To obtain the grid convergence, i.e. the more dense grid does not affect the results, and sufficient accuracy in Chimera interpolation, the simulation should be done on the finest grid level and possibly especially the propeller, duct and wake region grids would need even more computational cells.

In this chapter the results obtained in the resistance, propeller open water and self-propulsion simulations of the modified vessel B have been presented and discussed. The results have been given as percentages of the corresponding results of the original vessel model tests and the results of the RANS simulations of the original vessel A used for comparison have been shown. In the next chapter the obtained results are further discussed and concluding remarks of the study are made.

Chapter 7

Conclusions

In the previous chapter the results obtained were presented and discussed. In this chapter the conclusions of the results are made and the recommendations for the further work are given.

7.1 Resistance

The resistance simulations were conducted for the vessels A and B with the bare hulls. The results of the simulation with the vessel A were compared to the corresponding model test data, the only difference in the models used being that in the model test the model included also the rudder and pre-swirl stators. The comparison revealed, that the bare hull resistance obtained with FINFLO is 3.6 % smaller than the resistance obtained in the model test basin. Partly this difference results from the effect of the appendages and for example in Chapter 4 it is approximated that the rudder resistance is 3 % of the total resistance. Hence the accuracy of the FINFLO resistance prediction is regarded good. While the resistance was well estimated, a relatively large difference was obtained in the nominal wake field prediction. The nominal wake fraction w_n by FINFLO is 17.2 % smaller than in the model test measurement, which is probable a result of the inaccuracies in the turbulence modeling and grid resolution. Additionally the pre-swirl stators used in the model test measurement affect the wake by increasing the wake factor by few percents. This effect is though small when compared to the total difference of 17.2 % between the simulation and model test results.

The comparison of the simulation results of the vessels A and B showed, that the hull form modifications had positive effect on the hull resistance. The modifications made on the aft skeg changed the dynamic position of the ship, which resulted with the better wave pattern and thus decreased the total resistance. The averaged nominal wake w_n was increased with the new hull form at the propeller plane.

7.2 Simulation of the propeller in the open water condition

The propeller open water simulations were done in order to evaluate the accuracy of FINFLO-solver in the ducted propeller simulation. The ducted propeller simulations were done on the grid level L2 and additionally two points were calculated on the finest grid level L1. The results were compared to the model test results of the open water test. For a comparison point, the open water simulations were conducted also for the open propeller of the vessel A on the grid level L2.

The propeller open water simulations with the both propellers showed that a too coarse grid does not give accurate results but the propeller thrust and torque are overestimated, especially at the lower advance numbers. The simulation with the finest grid level improved the simulation results of the ducted propeller thrust and torque remarkably while the duct force prediction was not improved. The most probable reason for the difference in the duct force prediction are the small inaccuracies in the duct geometry at the leading and trailing edges. These inaccuracies affect the pressure field at the leading edge and the free vortices at the trailing edge.

7.3 Self-propulsion

The self-propulsion simulations were conducted for the vessels A and B on the grid level L2. The simulation of the vessel A was done with a fixed propeller rotation rate defined in the model test and the self-propulsion point was not reached. In the self-propulsion simulation of the vessel B, the self-propulsion point was searched by updating the propeller rotation rate and was obtained with 0.3 % difference in the obtained and required thrust. The propeller open water simulations revealed that the propeller simulation accuracy on the grid level L2 is not good. Additionally, the fixed free surface used in the simulation and the wake field calculation are not accurate. Hence the self-propulsion results obtained in the simulation are only approximate.

The comparison of the self-propulsion simulation results of the vessel B to the model test data of the vessel A showed, that the total thrust required was increased by 6.0 %, the power delivered at the propeller increased by 18.2 % and the propeller rotation rate decreased by 12.4 %. The hull efficiency was decreased remarkably. Based on these results the ducted propeller is not an effective solution for the propulsion of the vessel B. However, if the guidelines from the propeller open water simulation are considered and a correction is done to the estimated propeller torque, more promising results are obtained. If the propeller torque is over predicted as much as in the propeller open water simulation on the grid level L2 at the design point, the power delivered at the propeller is decreased by 14.6 % from the P_D of the vessel A. If the torque of the propeller is overestimated at least by 15.4 %, the required power delivered at the propeller is equal or decreased from that of the original vessel A and with the overestimation of 11.2 %, the power demand would increase 5 %.

The results reveal that the most remarkable effect of the ducted propeller is the decreased propeller rotation rate, which can enable a usage of more efficient slow

speed engines. It is also possible, that the power demand of the vessel is decreased with the ducted propeller, if there is a quite large difference in the simulation and real torque values like the propeller open water simulation results suggest. As the ducted propeller used in the simulation was not optimized for the case vessel, it is possible that even if the power demand with the used ducted propeller is increased by 5 %, the P_D would be decreased with the duct and propeller shapes optimized for the vessel. Additionally, in this thesis the changes in the aft shape were kept as small as possible. With larger changes also the hull shape could be optimized to be more suitable for the ducted propeller. However, no reliable conclusions can be made because of the uncertainties in the duct simulation and force corrections. It seems though, that the ducted propulsion could be an effective solution for this kind of vessel.

7.4 Recommendations for further work

The resistance simulation by FINFLO gives already fairly accurate results for the resistance but the wake field is not correct. Improvements could be possibly obtained with a denser grid at the wake field. Other widely known reason for the inaccurate wake field prediction is the problematic turbulence modeling at the wake field. As the SST $k - \omega$ turbulence model used in the FINFLO ship simulation is the one commonly used in ship hydrodynamics, it is suggested that the field of the turbulence modeling at ship applications is followed in order to find out if a turbulence model more suitable for ship flow simulations is released.

In the propeller simulation with the fine grid fairly accurate results are obtained for the propeller thrust and torque, while the duct performance simulation is incorrect. To get more reliable results of the ducted propulsion simulation, the reason for the inaccuracies in the duct simulation should be clarified and corrected. As the most probable reason for the inaccuracies is the slightly incorrect duct geometry, the first step would be to find a more detailed description of the leading and trailing edge roundings than that used in this thesis. After the possible corrections are made on the duct geometry, the open water simulations should be repeated. If the possible corrections on the geometry do not affect the results remarkable, further investigations for the reason of the inaccuracies should be done. For example a denser background grid might improve results, as it is possible that with the current grid the duct wake field and free vortices are not correctly modeled and thus the duct forces are inaccurate. Additionally, as the open water simulations performed in this thesis were done as quasi-static simulations with MRF method, also the time-accurate simulation might give more information about the problem. It is possible that the approximated boundary conditions used in MRF method affect the simulation results.

The accuracy of the self-propulsion simulation depends strongly on the wake field simulation and on the propeller simulation. A step towards a more accurate self-propulsion simulation would be the usage of a denser grid at the aft region where the propeller is located since even though the wake field might still be incorrect, the propeller simulation would be more accurate. Other improvements for the self-propulsion scheme used in FINFLO would be an automatized procedure for updating the propeller rotation rate based on the changes in ship resistance since

currently these changes are done manually.

When considering the ducted propeller in the large vessel, more testing is required in order to validate the efficiency of the solution. Either the self-propulsion test should be done in a model test or the self-propulsion simulation should be repeated by at least one other RANS solver to see if the trends in the propeller rotation rate and power demand estimations are true. Further investigations should also be done on different ducted propellers in order to find an optimum design for a large vessel.

Bibliography

- R. Ajanko. Laivarungon virtauslaskentaprosessin kehittäminen. Master's thesis, Teknillinen Korkeakoulu, 2008.
- American Bureau of Shipping. Guidance notes on ship vibration, April 2006. Available: https://www.eagle.org/eagleExternalPortalWEB/ShowProperty/BEA%20Repository/Rules&Guides/Current/147_ShipVibration/Pub147_ShipVib.
- J. Baltazar and J. A. C. Falcão de Campos. On the Modelling of the Flow in Ducted Propellers With a Panel Method. In K. Koushan and S. Steen, editors, *Proceedings of the First International Symposium on Marine Propulsors - smp'09. 22-24 June 2009. Trondheim, Norway*. MARINTEK, 2009. [Referenced:10.02.2014]. ISBN (electronic): 978-82-7174-264-5. ISBN (printed): 978-82-7174-263-8. Available: <http://www.marinepropulsors.com/proceedings-2009.php>.
- J. Baltazar, J. A. C. Falcão de Campos, and J. Bosschers. Open-Water Thrust and Torque Prediction of a Ducted Propeller System with a Panel Method. *International Journal of Rotating Machinery*, 2012:11 pages, 2012. [Referenced: 10.02.2014]. DOI: 10.1155/2012/474785. Available: <http://www.hindawi.com/journals/ijrm/2012/474785/>.
- Becker Marine Systems. Becker nozzle: High-performance and efficient heavy-duty manoeuvring solution. Product brochure, a. [Online] [Referenced: 25.03.2014] Available: http://www.becker-marine-systems.com/05_downloads/zzpdf/product_pdf/Becker_Nozzle.pdf.
- Becker Marine Systems. Product brochure, b. [Online] [Referenced: 17.02.2014] . Available: http://www.becker-marine-systems.com/05_downloads/zzpdf/product_pdf/Becker_Product_Brochure.pdf.
- J. Bosschers, G. Vaz, A. Starke, and E. van Wijngaarden. Computational analysis of propeller sheet cavitation and propeller-ship interaction. In *RINA conference "MARINE CFD2008". 26-27 March 2008. Southampton, UK.*, 2008. [Referenced:05.02.2014]. Available: http://www.marin.nl/upload_mm/1/e/a/1807585792_1999999096_Computational_analysis_of_sheet_cavitation_and_propeller-ship_interaction_-_RINA_CFD2008.pdf.
- J. S. Carlton. *Marine Propellers and Propulsion*. Butterworth-Heinemann, 1st edition, 1994. ISBN 075061143X.

- P. M. Carrica, A. M. Castro, and F. Stern. Self-propulsion computations using a speed controller and a discretized propeller with dynamic overset grids. *Journal of Marine Science and Technology*, 15(4):316–330, Dec 2010. [Referenced: 06.02.2014]. DOI:10.1007/s00773-010-0098-6.
- P. M. Carrica, H. Fu, and F. Stern. Computations of self-propulsion free to sink and trim and of motions in head waves of the KRISO Container Ship (KCS) model. *Applied Ocean Research*, 33(4):309–320, Oct 2011. [Referenced: 06.02.2014]. DOI:10.1016/j.apor.2011.07.003.
- F. Çelik, A. Doğrul, and Y. Arikan. Investigation of the Optimum Duct Geometry for A Passenger Ferry. In C. Pensa and P. Cioffi, editors, *Conference proceedings. 9th Symposium on High Speed MMarine Vessels. May 2011. Naples, Italy.*, 2011. [Referenced:10.02.2014]. ISBN: 978-88-906112-0-9. Available: <http://www.din.unina.it/HSMV%202011%20Proceedings/html/Papers/17.pdf>.
- J. Dang and H. Laheji. Hydrodynamic Aspects of Steerable Thrusters. In *Presentation. Dynamic Positioning Conference. 22-30 September, 2004. Houston, USA.* Wärtsilä Propulsion Netherlands BV (WPNL), 2004. [Referenced: 06.03.2014]. Available:http://www.dynamic-positioning.com/dp2004/thrusters_dang_pp.pdf.
- G. Dhinesh, K. Murali, and V. A. Subramanian. Estimation of hull-propeller interaction of a self-propelling model hull using a ranse solver. *Ships and Offshore Structures*, 5(2):125–139, Aug 2010. DOI: 10.1080/17445300903231109.
- B. Epps. Openprop v2.4 theory document, December 2010. Available: <http://engineering.dartmouth.edu/epps/openprop/index.html>.
- Finflo Ltd. Finflo user guide version 8.1, 2012.
- Q. Gao, W. Jin, and D. Vassalos. The calculations of propeller induced velocity by RANS and momentum theory. *Journal of Marine Science and Application*, 11(2): 164–168, Jun 2012. DOI: 10.1007/s11804-012-1118-1.
- G. R. Hough and D. E. Ordway. The generalized actuator disk. TAR-TR 6401, Therm Advanced Research, Inc., January 1964. [Referenced: 07.02.2014] Available: <http://oai.dtic.mil/oai/oai?verb=getRecord&metadataPrefix=html&identifier=AD0433976>.
- T. Kawamura, H. Miyata, and K. Mashimo. Numerical simulation of the flow about self-propelling tanker models. *Journal of Marine Science and Technology*, 2(4): 245–256, Dec 1997. DOI: 10.1007/BF02491531.
- J. E. Kerwin. *Principles of Naval Architecture Series: Propulsion*. The Society of Naval Architect, 2010. ISBN 093977383X. ISBN: 978-0-939773-83-1.
- J. E. Kerwin, S. A. A. Kinnas, J.-T. Lee, and W.-Z. Shih. A Surface Panel Method for the Hydrodynamic Analysis of Ducted Propellers. Massachusetts Inst of Tech Cambridge Dept of Ocean Engineering, 1987. [Referenced: 11.02.2014]. Available: <http://oai.dtic.mil/oai/oai?verb=getRecord&metadataPrefix=html&identifier=ADA192569>.

- G. Kuiper. *The Wageningen Propeller Series*. MARIN, May 1992. ISBN-10: 90-9007247-0.
- M. Lakatos. Evaluation of a propulsion calculation procedure using an actuator disk model featured in a RANS model. Master's thesis, Aalto University School of Engineering, 2013.
- L. Larsson and H. C. Raven. *The Principles of Naval Architecture Series: Ship Resistance and Flow*. The Society of Naval Architects and Marine Engineers, 2010. ISBN: 978-0-939773-76-3.
- J. Marzi and D. Hafermann. The v-SHALLO User Guide, Release 1.8.5. Hamburgische Schiffbau Versuchsanstalt GmbH, October 2008.
- J. Matusiak. Johdatus laivan aallonmuodostukseen, 2005. Helsinki University of Technology, M - 227.
- J. Matusiak. *Laivan propulsio*. Picaset Oy, 7 edition, 2007a. Helsinki University of Technology, Ship Laboratory, M-176.
- J. Matusiak. Laskennallinen laivahydrodynamiikka, September 2007b. Helsinki University of Technology.
- T. Mikkola. Computational ship hydrodynamics. Lecture notes, 2013. Aalto University.
- A. Minchev, J. R. Nielsen, and E. Lundgren. Ducted Propeller Design and Verification for Contemporary Offshore Support Vessels. In K. Koushan and S. Steen, editors, *Proceedings of the First International Symposium on Marine Propulsors - smp'09. 22-24 June 2009. Trondheim, Norway*. MARINTEK, 2009. [Referenced: 10.02.2014]. ISBN (electronic): 978-82-7174-264-5. ISBN (printed): 978-82-7174-263-8. Available: <http://www.marinepropulsors.com/proceedings-2009.php>.
- A. F. Molland and S. R. Turnock. *Marine Rudders and Control Surfaces*. Butterworth-Heinemann, 1TH edition, 2007.
- M. W. C. Oosterveld. Wake adapted ducted propellers. Publication No. 345, NSMB., 1970.
- A. B. Phillips, S. R. Turnock, and M. Furlong. Evaluation of manoeuvring coefficients of a self-propelled ship using a blade element momentum propeller model coupled to a Reynolds-averaged Navier-Stokes flow solver. *Ocean Engineering*, 36 (15-16):1217–1225, Nov 2009. DOI: 10.1016/j.oceaneng.2009.07.019.
- J. V. Pytkäinen. Influence of Advance Number on the Performance of Ducted Propellers in Three Duct Configurations. Helsinki University of Technology, Ship Laboratory, M-156., 1991.
- D. Ripjkema, B. Starke, and J. Bosschers. Numerical simulation of propeller-hull interaction and determination of the effective wakr field using hybrid RANS-BEM approach. In R. B. J. Binns and N. Bose, editors, *Proceedings of the Third International Symposium on Marine Propulsors - smp13. 5-8 May 2013*.

- Launceston, Tasmania, Australia*. Australian Maritime College, University of Tasmania, 2013. [Referenced:05.02.2014]. ISBN: 978-646-90334-7. Available: <http://www.marinepropulsors.com/proceedings-2013.php>.
- A. H. Sacks and J. A. Burnell. Ducted propellers - critical review of the state of the art. Report No. ARD-232, June 1959.
- A. Sánchez-Caja. Proepller theory. Lecture Notes of Potential Flow Theory for Lifting Surfaces, extended course. Aalto Univesity School of Engineering, 2013.
- A. Sánchez-Caja and J. Pylkkänen. Prediction of effective wake at model and full scale using a rans code with actuator disk model. In *Second International Conference on Maritime Research and Transportation. 28-30 June, 2007. Ischia, Naples, Italy.*, 2007. [Referenced: 05.02.2014]. <http://www.icmrt07.unina.it/Proceedings/>.
- A. Sánchez-Caja, J. Pylkkänen, and T. P. Sipilä. Simulation of the Incompressible Viscous Flow around Ducted Propellers with Rudders using a RANSE Solver. In *27th Symposium on Naval Hydrodynamics. 5-10 October, 2008. Seoul, Korea.*, 2008. [Referenced: 10.02.2014]. ISBN: 978-1-61738-774-6. Available: <http://202.114.89.60/resource/pdf/4318.pdf>.
- T. Siikonen. Virtaussimulointi. Course material. Aalto University School of Engineering., 2013.
- T. Siikonen. Laskennallisen virtausmekaniikan jatkokurssi. Course material. Aalto University School of Engineering., 2014.
- T. Siikonen, E. Salminen, and J. Ilkko. Comparison between hull flow simulation of a model-scale and a full-scale tanker. Technical Report F-66, Finflo Ltd., 2010.
- J. M. Stubblefield. Numerically-Based Ducted Propeller Design Using Vortex Lattice Lifting Line Theory. Master's thesis, Massachusetts Institute of Technology, June 2008.
- Y. Tahara, R. V. Wilson, P. M. Carrica, and F. Stern. RANS simulation of a container ship using a single-phase level-set method with overset grids and the prognosis for extension to a self-propulsion simulator. *Journal of Marine Science and Technology*, 11(4):209–228, Dec 2006. doi: 10.1007/s00773-006-0231-8. DOI:10.1007/s00773-006-0231-8.
- T. Taketani, K. Kimura, N. Ishii, M. Matsuura, and Y. Tamura. Advanced design of a ducted propeller with high bollard pull performance. In K. Koushan and S. Steen, editors, *Proceedings of the First International Symposium on Marine Propulsors - smp'09. 22-24 June 2009. Trondheim, Norway*. MARINTEK, June 2009. [Referenced: 10.02.2014]. ISBN (electronic): 978-82-7174-264-5. ISBN (printed): 978-82-7174-263-8. Available: <http://www.marinepropulsors.com/proceedings-2009.php>.

- Y. Tamura, Y. Nanke, M. Matsuura, T. Taketani, K. Kimura, and N. Ishii. Development of a high performance ducted propeller. In *The 21st International Tug, Salvage & OSV Convention and Exhibition. 2010. Vancouver, Canada.*, 2010. [Referenced: 10.02.2014] Available: http://towmasters.files.wordpress.com/2010/09/its6_high_performance_ducted_propeller.pdf.
- R. Van Houten. Analysis of ducted propellers in steady flow. Technical Report ARMC Report No. 4.76-1, Airflow Research and Manufacturing Corporation, 1986.
- J. D. van Manen and M. W. C. Oosterveld. Series of model tests on ducted propellers. Netherland Ship Model Basin Wageningen, 1972. [Referenced: 10.02.2014]. Available: <http://oai.dtic.mil/oai/oai?verb=getRecord&metadataPrefix=html&identifier=AD0746868>.
- T. Watanabe, T. Kawamura, Y. Takekoshi, M. Maeda, and S. Rhee. Simulation of Steady and Unsteady Cavitation on a Marine Propeller Using a RANS CFD Code. In *Fifth International Symposium on Cavitation. 1-4 November, 2003. Osaka, Japan.*, 2003. [Referenced: 13.02.2014]. Available: <http://202.114.89.60/resource/pdf/4428.pdf>.
- F. White. *Viscous Fluid Flow*. Mc Graw Hill, 3rd edition, 2006. ISBN: 007-124493-X.
- D. C. Wilcox. *Turbulence Modeling for CFD (Third Edition)*. DCW Industries, 2006. ISBN: 1-928729-08-8.
- L. Yu, M. Druckenbrod, M. Greve, and M. Abdel-Maksoud. An Automatic Optimization Process for Optimal Ducted Propeller Design and Its Application Based on CFD Techniques. In R. B. J. Binns and N. Bose, editors, *Proceedings of the Third International Symposium on Marine Propulsors - smp13. 5-8 May 2013. Launceston, Tasmania, Australia*. Australian Maritime College, University of Tasmania, 2013. [Referenced:10.02.2014]. ISBN: 978-646-90334-7. Available: <http://www.marinepropulsors.com/proceedings-2013.php>.
- Z.-r. Zhang. Verification and Validation for RANS Simulation of KCS Container Ship Without/With Propeller. *Journal of Hydrodynamics, Ser. B*, 22(5):932–939, Oct 2010. DOI: 10.1016/S1001-6058(10)60055-8.
- Y. Zheng and M.-S. Liou. A Novel Approach of Three-Dimensional Hybrid Grid Methodology: Part 1. Grid Generation. *Computer Methods in Applied Mechanics and Engineering*, 192(37-38):4147–4171, Sep 2003. DOI: 10.1016/S0045-7825(03)00385-2.

Appendix A

Duct geometry

Geometry data of the duct is shown in Table A.1. For nozzle the 19A the length-diameter ratio is $L/D = 0.5$.

Table A.1: Propeller Ka4-55 geometry. Taken from (Kuiper, 1992).

x/L	y_{inner}/L	y_{outer}/L
0	18.25	
1.25	14.66	20.72
2.5	12.8	21.07
5	10.07	20.8
7.5	8	—
10	6.34	—
15	3.87	—
20	2.17	—
25	1.1	—
30	0.48	—
40	0	—
50	0	—
60	0	—
70	0.29	—
80	0.82	—
90	1.45	—
95	1.86	—
100	2.36	6.36

Appendix B

Propeller geometry

The geometry of the propeller 4-55 is shown in Figure B.1. In Table B.1 are shown the propeller parameters and in Table B.2 are shown the coordinates for propeller geometry for suction and pressure side. The zero location is at 0 % , the trailing edge is at -100 % and the leading edge is at 100 %. The profiles are given as a percentage of the maximum thickness of the blade section. The chord length of a propeller is calculated with

$$c_r = \frac{K_r \cdot D \cdot EAR}{Z}, \quad (\text{B.1})$$

where K_r is given in Table B.1, D is the propeller diameter, EAR is the propeller are ratio (A_e/A_0) and Z is the number of blades (Kuiper, 1992).

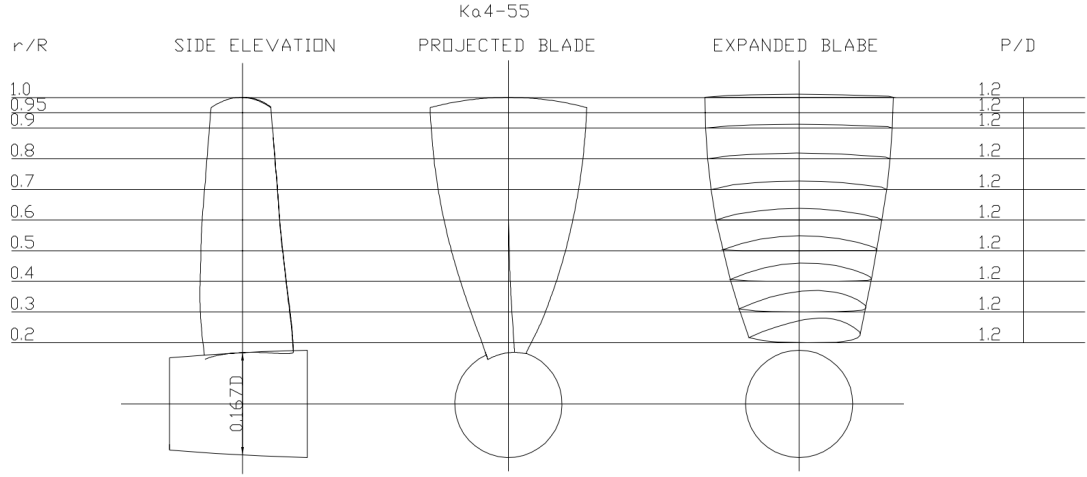


Figure B.1: Geometry of propeller Ka4-55

Table B.1: Ordinates of nozzle 19A. Taken from (Kuiper, 1992).

r/R	P/D	$Rake$	$Skew/c_r$	c_r/D	f_{max}/c_r	t_{max}/c_r	x_{tmax}/c_r	K_r
0.2	1.20	0.0	0.050	0.1818	0.0469	0.0400	0.3498	1.322
0.3	1.20	0.0	0.028	0.2074	0.0538	0.0352	0.3976	1.508
0.4	1.20	0.0	0.013	0.2306	0.0501	0.0300	0.4602	1.677
0.5	1.20	0.0	0.006	0.2518	0.0417	0.0245	0.4913	1.831
0.6	1.20	0.0	0.000	0.2709	0.0351	0.0190	0.4998	1.970
0.7	1.20	0.0	0.000	0.2866	0.0241	0.0138	0.5000	2.084
0.8	1.20	0.0	0.000	0.2980	0.0154	0.0092	0.5000	2.167
0.9	1.20	0.0	0.000	0.3050	0.0100	0.0061	0.5000	2.218
1.0	1.20	0.0	0.000	0.3076	0.0081	0.0050	0.5000	2.237

Table B.2: Ordinates of propeller of Ka-series. Taken from (Kuiper, 1992).

r/R	-100 % = TE	-80 %	-60 %	-40 %	-20 %	0 % = x_{tmax}	20 %	40 %	60 %	80 %	90 %	95 %	100 % = LE
Face = suction side													
0.2	-	45.52	65.42	82.50	95.00	100.00	98.13	92.29	81.56	65.52	54.79	48.02	-
0.3	-	43.67	67.70	84.14	95.86	100.00	97.75	90.89	78.34	59.17	46.15	37.87	-
0.4	-	42.92	67.50	85.69	96.25	100.00	97.22	89.31	75.00	52.92	38.61	30.27	-
0.5	-	42.45	68.76	86.42	96.60	100.00	96.77	87.27	70.97	46.86	31.58	23.77	-
0.6	-	43.58	68.26	85.89	96.47	100.00	96.47	85.89	68.26	43.58	28.59	20.44	-
0.7	-	45.31	69.24	86.33	96.58	100.00	96.58	86.33	69.24	45.31	30.79	22.88	-
0.8	-	48.16	70.84	87.04	96.76	100.00	96.76	87.04	70.84	48.16	34.39	26.90	-
0.9	-	51.75	72.94	88.09	97.17	100.00	97.17	88.09	72.94	51.75	38.87	31.87	-
1.0	-	52.00	73.00	88.00	97.00	100.00	97.00	88.00	73.00	52.00	39.25	32.31	-
Back = pressure side													
0.2	20.21	7.29	1.77	0.10	-	-	0.21	1.46	4.37	10.52	16.04	20.62	33.33
0.3	13.85	4.62	1.07	-	-	-	0.12	0.83	2.72	6.15	8.28	10.30	21.18
0.4	9.17	2.36	0.56	-	-	-	-	0.42	1.39	2.92	3.89	4.44	13.47
0.5	6.62	0.68	0.17	- -	-	-	-	0.17	0.51	1.02	1.36	1.53	7.81

Table C.1: Coefficients for polynomials, Ka3-65 and Ka4-55. Taken from (Oosterveld, 1970)

x	y	Ka3-65			Ka4-55		
		Axy	Bxy	Cxy	Axy	Bxy	Cxy
0	0	0.028100	0.154000	0.006260	-0.375000	-0.045100	-0.034700
0	1	-0.143910	0.115560		-0.203050		0.018568
0	2	-0.123761	-0.017942		0.830306		
0	3	-0.38373			-2.746930	-0.663741	
0	4	-0.008089				-0.244626	-0.195582
0	5	-0.741240					0.317452
0	6	0.646894			0.067548		-0.093739
1	0	-0.542674			2.030070	0.244461	0.158951
1	1	-0.429709	-0.749643		-0.392301	-0.578464	-0.048433
1	2	-0.016644			-0.611743	1.116820	
1	3				4.319840	0.751953	0.024157
1	4				-0.341290		
1	5						-0.123376
1	6	-0.162202				-0.08916	
2	0	0.671268	0.972388		-3.031670		-0.212253
2	1					-0.146178	
2	2	0.286926	1.468570			-0.917516	
2	3				-2.007860		
2	4						
2	5						
2	6						
3	0	-0.182294	-0.317644	0.040041	2.836970	0.068186	0.156133
3	1					0.174041	
3	2	-1.084980				0.102334	
3	3				0.391304		
3	4						
3	5						
3	6	-0.032298					
4	0				-0.994962		
4	1						0.030740
4	2						0.073587
4	3	0.199637					
4	4						
4	5						
4	6						
5	0						-0.031826
5	1	0.060168			0.015742		-0.014568
5	2						-0.109363
5	3						
5	4						0.043862
5	5						
5	6						
6	0	-0.003460			0.043782	-0.008581	0.007947
6	1	-0.17378	-0.000674				
6	2	0.001721					0.038275
6	3						
6	4						-0.021971
6	5						
6	6						0.000700
0	7					0.088319	0.022850

Table C.2: Coefficients for polynomials, Ka4-70 and Ka5-75. Taken from (Oosterveld, 1970)

x	y	Ka4-70			Ka5-75		
		Axy	Bxy	Cxy	Axy	Bxy	Cxy
0	0	0.030550	0.076594	0.006735	0.033000	0.007210	-0.000813
0	1	-0.148687	0.075223		-0.153463		0.034885
0	2		-0.061881	-0.016306		-0.014670	
0	3	-0.391137	-0.138094		-0.398491		-0.276187
0	4			-0.007244		-0.006398	
0	5		-0.370620				
0	6		0.323447				
1	0		-0.271337				
1	1	-0.432612	-0.687921		-0.435515		-0.626198
1	2		0.225189	-0.024012		-0.031380	0.450379
1	3						
1	4						
1	5						
1	6		-0.081101				
2	0	0.667657	0.666028		0.664045		0.359718
2	1						
2	2		0.734285	0.005193	0.283225	0.010386	
2	3						
2	4						
2	5						
2	6						
3	0	-0.172529	-0.202467	0.046605	-0.162764	0.053169	-0.087289
3	1						
3	2		-0.542490				
3	3						
3	4						
3	5						
3	6		-0.016149				
4	0			-0.007366		-0.014731	
4	1						
4	2						
4	3		0.099819				
4	4						
4	5						
4	6						
5	0						
5	1						
5	2		0.030084				
5	3						
5	4						
5	5						
5	6						
6	0			-0.001730			
6	1	-0.017293		-0.000337	-0.017208		
6	2		-0.001876	0.00861			-0.003751
6	3						
6	4						
6	5						
6	6						
0	7						

Appendix D

FINFLO input and boundary conditions

The simulation in FINFLO is controlled with input- and boundary condition-files. Below are shown these files for resistance and self-propulsion simulations.

D.1 Resistance simulation

Input-file for the resistance simulation.

```
&INPUTS
NAME      = 'Resistance, 14kts'
FLUXTY    = 'INCO'
FULLNC    = 'no'
CFL       = 2.0
CFLl      = 2.0
ICMAX     = 20000
IPRESC    = 1
LEVEL     = 1
FRSTEM    = 288.15
TEMINI    = 288.15
FRSPRE    = 101325.0
AREF      = 7.406
CHLREF    = 7.654
FRSVEL    = 1.4990
ITURB     = 6
KP        = 15000
MPRINT    = 10000
KRRINT    = 4000
ALPHA     = 0.0
ARTSSP    = 10.
ALFAP     = 0.02
FRSDEN    = 1000.
ISTATE    = 6
IDRXX     = 6
XMOM      = -3.827
YMOM      = 0.0
```

```

ZMOM      = 0.0
XXTRAC    = 'no'
TURCOC    = 'yes'
IFSBC     = 4
JFIRST    = 32
NFSD      = 4
ICFST     = 350
GK        = -1.
GML       = -0.1
CFLFRE    = 4.
DTWMIN    = 1.E-4
DTWMAX    = 0.01
DWMV      = 0.001
FREDIF    = 200
FRESUC    = 'yes'
DT        = 1e-3
DISTANC   = 'NO'
NEGVC     = 'YES'
NEGV      = -1E-5
&END

&BLOCKS
FRSMUTB(:) = 76*0.01      FRSTURB(:) = 76*0.0002      TURLIMB(:) = 76*15000.
ALFAUB(:)  = 76*0.5
IK(:) = 76*1  IL(:)  = 76*2  IT(:)  = 76*-2
MGRID(:)= 76*1
IGRID(:,1)= 76*21
IGRID(:,2)= 76*5
IGRID(:,3)= 76*1
MOV(:) = 76*0
INTERK(:) = 76*1
&END

&FLIGHT
XCG(1)    = -3.827
ZCG(1)    = 0.0
TRIMA(1)  = 0.1278
DRAUGHTI(1) = 0
DRAUGHT(1) = 0.4200
&END

&WORKS
IOLD1     = 1
GRIDFI    = 'VOLUME_out.grd'
BCFILE    = 'VOLUME_out.bc'
&END

&FORCE_GROUP_DATA
&END

```

Boundary condition-file for resistance simulation (before splitting).

Resistance simulation - 14 kn

```

1
----- Block No.      1 -----
 304 192 160
1 1
MIR 1 192 1 160
2 1
MOV 1 304 1 160 4 H
    0 0.0 0.0 0.0 0.0 0.0 0.0 0.0 0.0 0.0 0.0 0.0 0.0 0.0 0.0
3 1
MIR 1 304 1 192
4 1
MIR 1 192 1 160
5 1
EXT 1 304 1 160
6 1
FRE 1 304 1 192

```

D.2 Self-propulsion simulation

Below is given the input file for the self-propulsion simulation on the medium grid level.

```

&INPUTS
NAME      = 'ducted self-propulsion, TA L2'
FLUXTY    = 'INCO'
FULLNC    = 'no'
LUSGS     = 1
CFL       = 2.0
CFL       = 2.0
ICMAX     = 60
IPRESC    = 1
LEVEL     = 2
FRSTEM    = 288.15
TEMINI    = 288.15
FRSPRE    = 101325.0
AREF      = 14.812
CHLREF    = 7.799
FRSVEL    = 1.499
ITURB     = 6
KP        = 10000
KRRINT    = 60
MPRINT    = 12
ALPHA     = 0.0
ARTSSP    = 20.0
ALFAP     = 0.02
FRSDEN    = 1000.
ISTATE    = 6
IDRXX     = 6
XMOM      = -0.12267

```

```

YMOM      = 0.0
ZMOM      = -0.26871
XXTRAC    = 'no'
TURCOC    = 'yes'
IFSBC     = 4
JFIRST    = 32
NFSD      = 4
ICFST     = 350
GK        = -1.
GML       = -0.1
CFLFRE    = 1.0
DTWMIN    = 1.E-4
DTWMAX    = 0.01
DWMV      = 0.0001
FREDIF    = 200
FRESUC    = 'yes'
DT        = 6.60E-4
TMAX      = 0.6601
TIMEC     = 'yes'
DISTANC   = 'yes'
NEGVC     = 'NO'
NEGV      = -1E-5
INCHIMC   = 'yes'
REFLECC   = 'yes'
ENTROPY_FIXC = 'yes'
&END

```

&BLOCKS

```

FRSMUTB(:) = 170*0.01      FRSTURB(:) = 170*0.0002      TURLIMB(:) = 170*15000.
ALFAUB(:)   = 170*0.5
MGRID(:)= 170*1
IGRID(1:158,1)= 158*21
IGRID(1:158,2)= 158*6
IGRID(1:158,3)= 158*1
IGRID(159:170,1)= 12*10
IGRID(159:170,3)= 12*2
IGRID(159:170,4)= 12*1
MOV(:) = 170*3
INTERK(:) = 170*-3
INTERI(:) = 170*-3
INTERJ(:) = 170*-3
NCHIMT(153:158) = 6*1
NCHIMT(159:170) = 12*2
ZEROVB(:) = 170*'no'
&END

```

&FLIGHT

```

XCG(1)    = -3.827
ZCG(1)    = 0.0
TRIMA(1)  = 0.1278

```

```

DRAUGHTI(1) = 0
DRAUGHT(1) = 0.4200
XCGI(2) = 0.04332756
YCGI(2) = 0.0
ZCGI(2) = 0.1611785
XCG(2) = 0.04332756
YCG(2) = 0.0
ZCG(2) = 0.1611785
VX(2) = -1.0
VY(2) = 0.0
VZ(2) = 0.0
SHAFT(2) = 38.0761
THETARI(2) = 180
THETAR(2) = 180
&END

&FORCE_GROUP_DATA
FORCE_GROUP_INFO=
'p' 'Propeller' 0.01516464 0.0 0.1611785 -1.0 0.0 0.1611785
'd' 'Nozzle' 0.01516464 0.0 0.1611785 -1.0 0.0 0.1611785
'e' 'blade1' 0.01516464 0.0 0.1611785 -1.0 0.0 0.1611785
'f' 'blade2' 0.01516464 0.0 0.1611785 -1.0 0.0 0.1611785
'g' 'blade3' 0.01516464 0.0 0.1611785 -1.0 0.0 0.1611785
'h' 'blade4' 0.01516464 0.0 0.1611785 -1.0 0.0 0.1611785
'i' 'duct inside' 0.01516464 0.0 0.1611785 -1.0 0.0 0.1611785
'u' 'duct outside' 0.01516464 0.0 0.1611785 -1.0 0.0 0.1611785
&END

&WORKS
IOLD1 = 1
GRIDFI = '../self-propulsion/VOLUME_hull_out.grd'
BCFILE = '../self-propulsion/VOLUME_hull_out.bc'
&END

```

Below is shown the boundary condition file for the self-propulsion simulation.

Self-propulsion simulation - 14 kn

```

20
----- Block No. 1 -----
304 192 160
1 1
CON 1 192 1 160 2 4 1
2 1
MOV 1 304 1 160 4 Ho
0 0.0 0.0 0.0 0.0 0.0 0.0 0.0 0.0 0.0 0.0 0.0 0.0 0.0 0.0
3 1
CON 1 304 1 192 2 3 1
4 1
CON 1 192 1 160 2 1 1
5 1
EXT 1 304 1 160

```

```

6 1
FRE 1 304 1 192
----- Block No. 2 -----
304 192 160
1 1
CON 1 192 1 160 1 4 1
2 1
MOV 1 304 1 160 4 Hv
0 0.0 0.0 0.0 0.0 0.0 0.0 0.0 0.0 0.0 0.0 0.0 0.0 0.0 0.0
3 1
CON 1 304 1 192 1 3 1
4 1
CON 1 192 1 160 1 1 1
5 1
EXT 1 304 1 160
6 1
FRE 1 304 1 192
----- Block No. 3 -----
128 32 256
1 2
CON 1 32 1 128 4 1 2
CON 1 32 129 256 6 1 2
2 1
MOV 1 128 1 256 4 dtu
0 0.0 0.0 0.0 0.0 0.0 0.0 0.0 0.0 0.0 0.0 0.0 0.0 0.0 0.0
3 1
CON 1 128 1 32 1 6 1
4 2
CON 1 32 1 128 4 4 2
CON 1 32 129 256 6 4 2
5 1
CON 1 128 1 256 2 2 1
6 1
CON 1 128 1 32 1 3 1
----- Block No. 4 -----
128 32 256
1 4
CON 1 16 1 128 4 1 1
CON 17 32 1 128 3 1 2
CON 1 16 129 256 6 1 1
CON 17 32 129 256 5 1 2
2 1
CON 1 128 1 256 1 5 1
3 1
CON 1 128 1 32 2 6 1
4 4
CON 1 16 1 128 4 4 1
CON 17 32 1 128 3 4 2
CON 1 16 129 256 6 4 1
CON 17 32 129 256 5 4 2

```

```

5 1
CHI 1 128 1 256
6 1
CON 1 128 1 32 2 3 1
----- Block No. 5 -----
192 48 128
1 2
CHI 1 32 1 128
CON 33 48 1 128 2 1 2
2 1
CON 1 192 1 128 5 2 1
3 1
CON 1 192 1 48 5 6 1
4 2
CHI 1 32 1 128
CON 33 48 1 128 2 4 2
5 1
CON 1 192 1 128 4 2 1
6 1
CON 1 192 1 48 5 3 1
----- Block No. 6 -----
192 48 128
1 2
CON 1 16 1 128 2 1 1
CON 17 48 1 128 1 1 1
2 1
CON 1 192 1 128 3 5 1
3 1
CON 1 192 1 48 6 6 1
4 2
CON 1 16 1 128 2 4 1
CON 17 48 1 128 1 4 1
5 1
MOV 1 192 1 128 4 dti
      0 0.0 0.0 0.0 0.0 0.0 0.0 0.0 0.0 0.0 0.0 0.0 0.0 0.0 0.0
6 1
CON 1 192 1 48 6 3 1
----- Block No. 7 -----
192 48 128
1 2
CHI 1 32 1 128
CON 33 48 1 128 2 1 4
2 1
CON 1 192 1 128 3 2 1
3 1
CON 1 192 1 48 3 6 1
4 2
CHI 1 32 1 128
CON 33 48 1 128 2 4 4
5 1

```

```

CON    1 192    1 128        6    2    1
6    1
CON    1 192    1  48        3    3    1
----- Block No.      8 -----
192  48 128
1    2
CON    1  16    1 128        2    1    3
CON   17  48    1 128        1    1    2
2    1
CON    1 192    1 128        5    5    1
3    1
CON    1 192    1  48        4    6    1
4    2
CON    1  16    1 128        2    4    3
CON   17  48    1 128        1    4    2
5    1
MOV    1 192    1 128        4 dti
      0 0.0 0.0 0.0 0.0 0.0 0.0 0.0 0.0 0.0 0.0 0.0 0.0 0.0 0.0
6    1
CON    1 192    1  48        4    3    1
----- Block No.      9 -----
 16  80  32
1    2
CON    1  80    1  16        7    1    2
CON    1  80   17  32        7    1    1
2    1
ROT    1  16    1  32
      0 0.0 0.0 0.0 0.0 0.0 0.0 0.0 0.0 0.0 0.0 0.0 0.0 0.0
3    1
CON    1  16    1  80        16    6    1
4    2
CON    1  80    1  16        8    1    1
CON    1  80   17  32        8    1    4
5    1
CHI    1  16    1  32
6    1
CON    1  16    1  80        10    3    1
----- Block No.     10 -----
 96  80 224
1    4
CON    1  80    1  16        7    4    1
CON    1  80   17 112        8    1    3
CON    1  80 113 208        8    1    2
CON    1  80 209 224        7    4    2
2    1
ROT    1  96    1 224
      0 0.0 0.0 0.0 0.0 0.0 0.0 0.0 0.0 0.0 0.0 0.0 0.0 0.0
3    1
CON    1  96    1  80        17    6    1
4    4

```

pt

pte

```

CON    1  80    1  16      9  1  1
CON    1  80   17 112      8  4  3
CON    1  80  113 208      8  4  2
CON    1  80 209 224      9  1  2
5  1
CHI    1  96    1 224
6  1
CON    1  96    1  80     11  3  1
----- Block No.    11 -----
 16  80  32
1  2
CON    1  80    1  16      8  4  1
CON    1  80   17  32      8  4  4
2  1
ROT    1  16    1  32
      0 0.0 0.0 0.0 0.0 0.0 0.0 0.0 0.0 0.0 0.0 0.0 0.0 0.0
3  1
CON    1  16    1  80     18  6  1
4  2
CON    1  80    1  16      9  4  2
CON    1  80   17  32      9  4  1
5  1
CHI    1  16    1  32
6  1
CON    1  16    1  80     12  3  1
----- Block No.    12 -----
 16  80  32
1  2
CON    1  80    1  16     10  1  2
CON    1  80   17  32     10  1  1
2  1
ROT    1  16    1  32
      0 0.0 0.0 0.0 0.0 0.0 0.0 0.0 0.0 0.0 0.0 0.0 0.0 0.0
3  1
CON    1  16    1  80      7  6  1
4  2
CON    1  80    1  16     11  1  1
CON    1  80   17  32     11  1  4
5  1
CHI    1  16    1  32
6  1
CON    1  16    1  80     13  3  1
----- Block No.    13 -----
 96  80 224
1  4
CON    1  80    1  16     10  4  1
CON    1  80   17 112     11  1  3
CON    1  80  113 208     11  1  2
CON    1  80 209 224     10  4  2
2  1

```

pt

pt

ROT 1 96 1 224
0 0.0 0.0 0.0 0.0 0.0 0.0 0.0 0.0 0.0 0.0 0.0 0.0 0.0 0.0
3 1
CON 1 96 1 80 8 6 1
4 4
CON 1 80 1 16 12 1 1
CON 1 80 17 112 11 4 3
CON 1 80 113 208 11 4 2
CON 1 80 209 224 12 1 2
5 1
CHI 1 96 1 224
6 1
CON 1 96 1 80 14 3 1
----- Block No. 14 -----
16 80 32
1 2
CON 1 80 1 16 11 4 1
CON 1 80 17 32 11 4 4
2 1
ROT 1 16 1 32
0 0.0 0.0 0.0 0.0 0.0 0.0 0.0 0.0 0.0 0.0 0.0 0.0 0.0 0.0
3 1
CON 1 16 1 80 9 6 1
4 2
CON 1 80 1 16 12 4 2
CON 1 80 17 32 12 4 1
5 1
CHI 1 16 1 32
6 1
CON 1 16 1 80 15 3 1
----- Block No. 15 -----
16 80 32
1 2
CON 1 80 1 16 13 1 2
CON 1 80 17 32 13 1 1
2 1
ROT 1 16 1 32
0 0.0 0.0 0.0 0.0 0.0 0.0 0.0 0.0 0.0 0.0 0.0 0.0 0.0 0.0
3 1
CON 1 16 1 80 10 6 1
4 2
CON 1 80 1 16 14 1 1
CON 1 80 17 32 14 1 4
5 1
CHI 1 16 1 32
6 1
CON 1 16 1 80 16 3 1
----- Block No. 16 -----
96 80 224
1 4

ptf

pt

pt


```

CON    1  80    1  16      13  4   1
CON    1  80   17 112      14  1   3
CON    1  80  113 208      14  1   2
CON    1  80 209 224      13  4   2
2  1
ROT    1  96    1 224
      0 0.0 0.0 0.0 0.0 0.0 0.0 0.0 0.0 0.0 0.0 0.0 0.0 0.0
3  1
CON    1  96    1  80      11  6   1
4  4
CON    1  80    1  16      15  1   1
CON    1  80   17 112      14  4   3
CON    1  80  113 208      14  4   2
CON    1  80 209 224      15  1   2
5  1
CHI    1  96    1 224
6  1
CON    1  96    1  80      17  3   1
----- Block No.   17 -----
16  80  32
1  2
CON    1  80    1  16      14  4   1
CON    1  80   17  32      14  4   4
2  1
ROT    1  16    1  32
      0 0.0 0.0 0.0 0.0 0.0 0.0 0.0 0.0 0.0 0.0 0.0 0.0 0.0
3  1
CON    1  16    1  80      12  6   1
4  2
CON    1  80    1  16      15  4   2
CON    1  80   17  32      15  4   1
5  1
CHI    1  16    1  32
6  1
CON    1  16    1  80      18  3   1
----- Block No.   18 -----
16  80  32
1  2
CON    1  80    1  16      16  1   2
CON    1  80   17  32      16  1   1
2  1
ROT    1  16    1  32
      0 0.0 0.0 0.0 0.0 0.0 0.0 0.0 0.0 0.0 0.0 0.0 0.0 0.0
3  1
CON    1  16    1  80      13  6   1
4  2
CON    1  80    1  16      17  1   1
CON    1  80   17  32      17  1   4
5  1
CHI    1  16    1  32

```

ptg

pt

pt

```

6 1
CON 1 16 1 80 7 3 1
----- Block No. 19 -----
96 80 224
1 4
CON 1 80 1 16 16 4 1
CON 1 80 17 112 17 1 3
CON 1 80 113 208 17 1 2
CON 1 80 209 224 16 4 2
2 1
ROT 1 96 1 224
0 0.0 0.0 0.0 0.0 0.0 0.0 0.0 0.0 0.0 0.0 0.0 0.0 0.0 0.0
3 1
CON 1 96 1 80 14 6 1
4 4
CON 1 80 1 16 18 1 1
CON 1 80 17 112 17 4 3
CON 1 80 113 208 17 4 2
CON 1 80 209 224 18 1 2
5 1
CHI 1 96 1 224
6 1
CON 1 96 1 80 8 3 1
----- Block No. 20 -----
16 80 32
1 2
CON 1 80 1 16 17 4 1
CON 1 80 17 32 17 4 4
2 1
ROT 1 16 1 32
0 0.0 0.0 0.0 0.0 0.0 0.0 0.0 0.0 0.0 0.0 0.0 0.0 0.0 0.0
3 1
CON 1 16 1 80 15 6 1
4 2
CON 1 80 1 16 18 4 2
CON 1 80 17 32 18 4 1
5 1
CHI 1 16 1 32
6 1
CON 1 16 1 80 9 3 1

```

pth

pt